

AD-A133 462

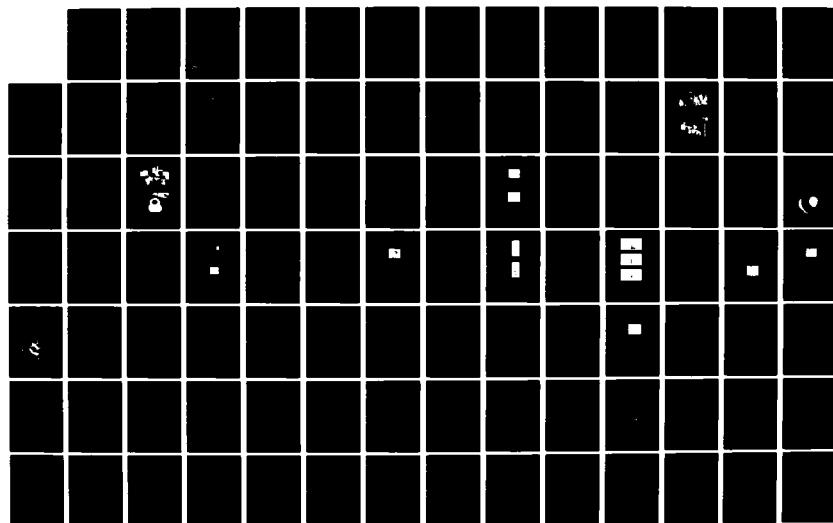
AN INVESTIGATION OF ACCELERATING MECHANISMS IN A PLASMA 1/2  
FOCUS RELEVANT TO. (U) OLD DOMINION UNIV NORFOLK VA  
DEPT OF ELECTRICAL ENGINEERING M S PRONKO ET AL.

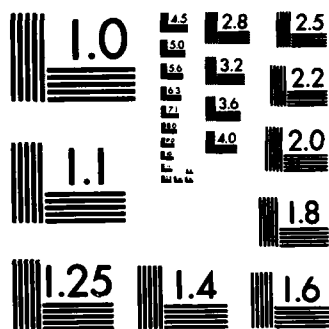
UNCLASSIFIED

JUL 83 AFOSR-TR-83-0794 AFOSR-81-0039

F/G 20/9

NL

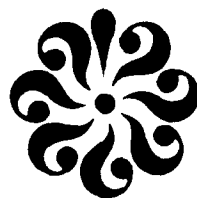




MICROCOPY RESOLUTION TEST CHART  
NATIONAL BUREAU OF STANDARDS-1963-A

AD-A133462

OLD DOMINION UNIVERSITY RESEARCH FOUNDATION



DTIC FILE COPY

AFOSR-TR- 83 - 0794

DEPARTMENT OF ELECTRICAL ENGINEERING  
SCHOOL OF ENGINEERING  
OLD DOMINION UNIVERSITY  
NORFOLK, VIRGINIA

AN INVESTIGATION OF ACCELERATING MECHANISMS IN A  
PLASMA FOCUS RELEVANT TO INTERRUPTING SWITCHES

By

Mark S. Pronko

and

G. Marshall Molen, Principal Investigator

Final Report

For the period ending Januray 31, 1983

Prepared for the  
Air Force Office of Scientific Research  
Bolling Air Force Base  
Washington, D.C. 20332

Under  
Research Grant AFOSR-81-0039  
Lt. Col. Anthony K. Hyder

DTIC  
OCT 12 1983

Approved for public release;  
distribution unlimited.

July 1983

83 10 04 079

DEPARTMENT OF ELECTRICAL ENGINEERING  
SCHOOL OF ENGINEERING  
OLD DOMINION UNIVERSITY  
NORFOLK, VIRGINIA

AN INVESTIGATION OF ACCELERATING MECHANISMS IN A  
PLASMA FOCUS RELEVANT TO INTERRUPTING SWITCHES

By

Mark S. Pronko

and

G. Marshall Molen, Principal Investigator

Final Report

For the period ending Januray 31, 1983

Prepared for the  
Air Force Office of Scientific Research  
Bolling Air Force Base  
Washington, D.C. 20332

Under  
Research Grant AFOSR-81-0039  
Lt. Col. Anthony K. Hyder

Submitted by the  
Old Dominion University Research Foundation  
P.O. Box 6369  
Norfolk, Virginia 23508

July 1983



AIR FORCE OFFICE OF SCIENTIFIC RESEARCH (AFSC)  
NOTICE OF TRANSMITTAL TO DTIC  
This technical report has been reviewed and is  
approved for public release IAW AFR 190-12.  
Distribution is unlimited.  
MATTHEW J. KERPER  
Chief, Technical Information Division

Unclassified

SECURITY CLASSIFICATION OF THIS PAGE (When Data Entered)

REPORT DOCUMENTATION PAGE		READ INSTRUCTIONS BEFORE COMPLETING FORM
1. <b>AFOSR-PR- 83-0794</b> 1	2. GOVT ACCESSION NO. AD-A133462	3. RECIPIENT'S CATALOG NUMBER
4. TITLE (and Subtitle) AN INVESTIGATION OF ACCELERATING MECHANISMS IN A PLASMA FOCUS RELEVANT TO INTERRUPTING SWITCHES		5. TYPE OF REPORT & PERIOD COVERED Final, November 1, 1980 to January 31, 1983
		6. PERFORMING ORG. REPORT NUMBER
7. AUTHOR(s) Mark S. Pronko and G. Marshall Molen, Principal Investigator		8. CONTRACT OR GRANT NUMBER(s)  AFOSR-81-0039
9. PERFORMING ORGANIZATION NAME AND ADDRESS  Department of Electrical Engineering Old Dominion University, Norfolk, VA 23508		10. PROGRAM ELEMENT, PROJECT, TASK AREA & WORK UNIT NUMBERS 61102F 2301/A7
11. CONTROLLING OFFICE NAME AND ADDRESS  Air Force Office of Scientific Research Bolling Air Force Base Washington, DC 20332		12. REPORT DATE July, 1983
		13. NUMBER OF PAGES 103
14. MONITORING AGENCY NAME & ADDRESS (if different from Controlling Office)		15. SECURITY CLASS. (of this report)  Unclassified
		15a. DECLASSIFICATION/DOWNGRADING SCHEDULE
16. DISTRIBUTION STATEMENT (of this Report)  This document has been approved for public release; its distribution is unlimited.		
17. DISTRIBUTION STATEMENT (of the abstract entered in Block 20, if different from Report)		
18. SUPPLEMENTARY NOTES		
19. KEY WORDS (Continue on reverse side if necessary and identify by block number)  Plasma Focus, Charged Particle Beams, Electron Beams, X-ray Simulator, Radiation Production, Interrupting Switches, Inductive Energy Storage		
20. ABSTRACT (Continue on reverse side if necessary and identify by block number)  An experimental investigation was conducted using a 34-kJ Dense Plasma Focus (DPF) in which the possible enhancement of the electron beam was addressed. Electron beams ejected from the DPF have been observed to exceed 30 kA with pulse durations of a few nanoseconds. Enhancement was considered to be either an increase in the probability that the peak beam current exceeded some lower limit, or an increase in the mean energy of the beam electrons. The investigation was divided into two parts, each addressing one of the aspects of enhancement.		

Unclassified

SECURITY CLASSIFICATION OF THIS PAGE(When Data Entered)

In the first part of the investigation, an axial magnetic field was introduced into the beam drift region so as to reduce beam loss due to contact with the conductive walls of the drift tube. The beam guiding apparatus was shown to increase the probability of observing a beam with a peak current greater than 10 kA from 10% of the DPF discharges to 20%.

The second part of the investigation initially addressed the apparent increase in the beam electron's mean energy produced by the introduction of a secondary discharge in the DPF pinch region prior to pinch formation. However, on the average, the presence in the DPF chamber of a third electrode which was necessary to produce the secondary discharge had an adverse effect on the transmission of the electron beam through the drift tube. This effect, which was shown to be inversely related to the distance between the DPF anode and the third electrode, subsequently became the main emphasis of the second part of the investigation. The diagnostic results obtained during the investigation were not sufficient to conclusively determine the role of the third electrode in the beam disturbance; however, it is speculated that the presence of the third electrode caused internal currents to circulate which magnetically deflected the electron beam from entering the drift tube region.



Accession For	
CRA&I	<input checked="" type="checkbox"/>
TAB	<input type="checkbox"/>
Unpublished	<input type="checkbox"/>
Classification	
Distribution/	
Availability Codes	
Dist	Attn and/or Special
<input checked="" type="checkbox"/>	<input type="checkbox"/>

11 Unclassified

SECURITY CLASSIFICATION OF THIS PAGE(When Data Entered)

## TABLE OF CONTENTS

	<u>PAGE</u>
TABLE OF CONTENTS . . . . .	iii
LIST OF FIGURES . . . . .	v
I. INTRODUCTION . . . . .	1
II. BACKGROUND . . . . .	4
III. THE EXPERIMENTAL ARRANGEMENT . . . . .	13
The Dense Plasma Focus . . . . .	15
The Guiding Field Solenoid and Pulser Circuit. . . . .	20
The Auxiliary Electrode . . . . .	26
The Faraday Cup . . . . .	29
IV. EXPERIMENTAL RESULTS . . . . .	35
Typical DPF Performance Data . . . . .	35
Electron Beam Guiding Field Results . . . . .	42
The Effect of the Auxiliary Electrode . . . . .	49
V. THEORETICAL CONSIDERATIONS . . . . .	58
Electron Beam Propagation . . . . .	58
The Guiding Field Concept . . . . .	63
Analysis of the Auxiliary Electrode Results . . . . .	66
VI. CONCLUSION . . . . .	77

	<u>PAGE</u>
LIST OF REFERENCES . . . . .	80
APPENDIX . . . . .	85
A.    DIAGNOSTIC EQUIPMENT . . . . .	86
Self-Integrated Rogowski Probe . . . . .	86
PIN Diodes . . . . .	88
Soft X-Ray Pinhole Photography . . . . .	89
Image Converter Camera System . . . . .	92
Ḃ Probe and Passive Integrator . . . . .	92
B.    GUIDING FIELD WINDING CONFIGURATION . . . . .	94
C.    DPF REMOTE CONTROL SYSTEM . . . . .	98
D.    DPF TRIGGER SYSTEM . . . . .	101



## LIST OF FIGURES

<u>FIGURE</u>	<u>PAGE</u>
II-1. The temporal evolution of the Mather-type DPF discharge illustrating (a) the initial breakdown, (b) the acceleration of the plasma sheath toward the end of the electrodes, (c) the arrival of the sheath at the end of the electrodes, and (d) the ensuing plasma pinch.	6
III-1. The DPF experimental apparatus (a) with the lead shield and (b) without the shield.	14
III-2. Schematic of the DPF with the vacuum vessel and drift tube assembly omitted for clarity. All dimensions are in centimeters.	16
III-3. The initial DPF anode and electron beam drift tube assembly. All dimensions are in centimeters.	18
III-4. Photographs of the DPF apparatus illustrating (a) the electrodes, capacitor bank modules, parallel-plate conductor arrangement, and (b) close-up of the coaxial electrodes.	19
III-5. The DPF anode and the guiding field solenoid apparatus. The solenoid's electrical connections and structural support are omitted for clarity. All dimensions are in centimeters.	21
III-6. Schematic of the guiding field solenoid pulser circuit.	24
III-7. The guiding field solenoid current for a capacitor voltage of 5.0 kV.	25
III-8. The guiding field magnetic flux density (upper trace) and corresponding solenoid current (lower trace) for a capacitor voltage of 5.0 kV.	25
III-9. The arrangement of the DPF electrodes and the auxiliary electrode used in this investigation. All dimensions are in centimeters.	27

<u>FIGURE</u>	<u>PAGE</u>
III-10. The DPF shown connected to the inductive energy storage circuit. Current transformers (CT-A and CT-B) were used to monitor the current in the circuit. The reference arrows shown below the transformers indicate the direction of conventional current flow which produces a positive signal.	28
III-11. Schematic of the Faraday cup shown attached to the guiding field drift tube.	30
III-12. Photograph of the Faraday cup.	30
III-13. The Faraday cup calibration circuit.	34
III-14. Faraday cup calibration illustrating the injected current (upper trace) and the cup response (lower trace).	34
IV-1. The DPF discharge current for operation with $V_0 = 16$ kV and $P_0 = 1.25$ torr.	37
IV-2. Typical image converter camera photographs showing (a) a 500 ns streak photograph, and (b) a framing photograph with a 20 ns shutter speed and 100 ns frame separation where $t = 0$ corresponds to the initial DPF x-ray pulse.	39
IV-3. Typical soft x-ray pinhole photographs.	41
IV-4. The bremsstrahlung x-ray dose rate produced by the electron beam was measured using the arrangement shown in (a) where PIN A and PIN B are PIN diodes which have intrinsic layer thicknesses of 20 $\mu\text{m}$ and 125 $\mu\text{m}$ , and $e^-$ transmissions of 40 keV and 300 keV, respectively. Typical results are shown in (b) for DPF operation with $V_0 = 16$ kV and $P_0 = 1.25$ torr.	43
IV-5. Typical DPF electron beam current as measured by the Faraday cup for DPF operation with $V_0 = 16$ kV and $P_0 = 1.25$ torr.	44
IV-6. The experimental arrangement shown in (a) was used to illustrate the divergence of the DPF electron beam from the DPF axis. The resulting damage is shown in (b).	45
IV-7. Peak beam current results illustrating the performance of the beam guiding apparatus. The peak current intervals are such that the histogram analysis includes the lower limit but excludes the upper limit.	48

<u>FIGURE</u>		<u>PAGE</u>
IV-8.	X-ray dose-rate measurements illustrating the performance of the beam guiding apparatus. The results collected using (a) PIN A and (b) PIN B are expressed in relative units, and the dose-rate intervals are such that the histogram analysis includes the lower limit but excludes the upper limit.	50
IV-9.	The Faraday cup results illustrating the effect of the auxiliary electrode when connected to the inductive energy storage circuit. The normalized confidence interval on the average peak beam current measured when the auxiliary electrode was not in the DPF chamber is $\pm 0.24$ .	53
IV-10.	The DPF current diverted to the inductive energy storage circuit as measured by CT-A. The upper trace shows the interaction over the entire DPF discharge interval and the lower trace is a time expansion of the upper trace over the interval shown. The signal polarity is such that positive current flow is opposite to the reference arrow shown in Fig. III-10.	55
IV-11.	Faraday cup results illustrating the effect of the auxiliary electrode when at the potential of the DPF cathode. The normalized confidence interval on the average peak beam current measured when the auxiliary electrode was not in the DPF chamber is $\pm 0.24$ .	57
V-1.	A transverse magnetic field in the region of the anode aperture at the time of beam formation can be produced by a secondary current density, $J$ . A possible closed path for the secondary current is shown by the dotted line.	69
V-2.	The interaction which produces the current measured by CT-A is modeled by the circuit shown in (a). The DPF current at the time of the pinch is modeled by (b) a piecewise-linear impulse-type function which has (c) a piecewise-continuous derivative.	71
V-3.	Response of the circuit shown in Fig. V-2(a) to the excitation presented in Fig. V-2(b) for $L = 3.2 \mu\text{H}$ , $C = 1.35 \text{ nF}$ , $\Delta I_1 = 250 \text{ kA}$ , $\Delta I_2 = 110 \text{ kA}$ , $\Delta t_1 = 25 \text{ ns}$ , and $\Delta t_2 = 35 \text{ ns}$ .	74
A-1.	Location of the Rogowski probe in the DPF apparatus that was used to measure the DPF discharge current.	87
A-2.	Electrical schematic of the Rogowski coil, $0.29\text{-}\Omega$ shunt resistor, and $50\text{-}\Omega$ impedance-matching resistor.	87

<u>FIGURE</u>		<u>PAGE</u>
A-3.	Electrical schematic of the PIN diode bias circuit.	90
A-4.	Ray tracing in a pinhole imaging system.	91
A-5.	Exploded view of the soft x-ray pinhole camera.	91
B-1.	Plot of the magnetic flux density measured along the axis of the guiding field solenoid in the region of the vacuum valve for a coil current of 150 A. The field plot is scaled to the drawing.	96
C-1.	Remote control logic diagram. Modules A through D are located outside the screenroom and each interfaces the control system to a single capacitor bank.	99
D-1.	The DPF trigger system.	102
D-2.	The Krytron pulse amplifier circuit.	103

## Chapter I

### INTRODUCTION

Over the last several years, applications for high-energy electron beam devices have experienced significant growth. These applications include such diverse areas as nuclear weapon effects simulation, intense microwave generation, collective ion acceleration, laser excitation, inertial confinement fusion studies, and industrial processing. Of the many types of charged particle accelerators, the dense plasma focus (DPF) has recently been recognized as an intense, high-energy electron beam source [1]. Although the generation of the electron beam is not a very efficient process in the DPF, the device is capable of producing beams with peak currents in excess of 30 kA with pulse durations of several nanoseconds. The energy of the electrons in the beam are typically in the range of a few hundred kiloelectron volts, but electrons with energies up to a megaelectron volt have also been observed. Electron beams with these parameters are of particular interest in radiation simulation studies where the electron beam is used to produce a short, intense burst of x rays by thick-target bremsstrahlung. In fact, this concept has already been proven useful for SGEMP (system-generated electromagnetic pulse) and TREE (transient radiation effects in electronics) testing of satellite components [2].

The DPF offers a method of producing an intense, short-duration electron burst from a relatively simple, compact device. In addition, the DPF

accelerating mechanism produces beams with energies significantly higher than implied by the initial capacitor bank voltage. As discussed in Chapter II, this accelerating mechanism is attributed to the development of an anomalous resistance in the dense plasma column.

The investigation addresses the possibility of enhancing the electron beam output of the DPF. For the purposes of this investigation, enhancement is defined as:

- (1) an increase in the probability that the peak beam current will be above some lower limit (i.e., an increase in the electron flux);  
or
- (2) an increase in the mean energy of the beam electrons.

The investigation was divided into two parts, each addressing one of the above aspects of enhancement.

The first part of the investigation involved the introduction of an externally generated, axial magnetic field in the beam drift region in order to reduce beam losses as the beam was transported through a half-meter-long, conductive drift tube. The externally generated magnetic field was of sufficient strength so as to limit the Larmor radius of a typical beam electron to a value less than the radius of the drift tube. The use of the magnetic guiding field was shown to double the probability that the peak beam current would exceed 10 kA.

The second part of the investigation was motivated by observations made in a study addressing the use of the DPF as an opening switch in an inductive energy storage system [3]. In that study a secondary discharge, which was in addition to the DPF discharge, was observed to apparently change the energy spectrum of the x rays emitted from the pinch region.

The x-ray dose rate at the low end of the spectrum (typically around 20 keV) was somewhat reduced by the presence of the secondary discharge suggesting a reduced plasma temperature and density. On the other hand, an increase in the x-ray dose rate was observed for energies greater than 300 keV suggesting an increase in the mean energy of the beam electrons which produce radiation by thick-target bremsstrahlung.

Initial experiments in the second part of the investigation showed that the presence of a third electrode, which was necessary to produce the secondary discharge, had an adverse effect on the production of the DPF electron beam. This electrode was in addition to the DPF electrodes and the adverse effect was observed without a secondary discharge present. On the average, the peak beam current was observed to decrease as the distance between the secondary electrode and the DPF electrodes decreased. Consequently, the emphasis of the second part of this investigation shifted to an attempt to identify the cause of this effect.

Background on the operation and characteristics of the DPF as well as a brief literature review of recent research conducted on the DPF electron beam are presented in Chapter II. The experimental arrangement and results are presented in Chapters III and IV, respectively. Chapter V contains a brief outline on electron beam propagation theory and analysis of the experimental results. Finally, conclusions and suggestions for further research are presented in Chapter VI.

## Chapter II

### BACKGROUND

The DPF is a coaxial electrode, plasma accelerator in which magnetic energy stored in the electrode geometry and external circuit is rapidly converted to plasma energy as an azimuthally symmetric current sheath collapses to form a dense plasma pinch [4]. As a result of the pinch, the device is capable of producing a high-current, short-duration, relativistic electron beam, an oppositely directed ion beam, and an intense burst of x radiation. Furthermore, with an appropriate fill gas such as deuterium, the DPF can be a relatively high-yield neutron source. Since its development in the early 1960's, the DPF has eluded the efforts of researchers attempting to gain a fundamental understanding of the mechanisms responsible for the plasma focus phenomena. The purpose of this chapter is to summarize some of the generally accepted ideas concerning the development of the plasma focus discharge and the resulting phenomena.

The DPF consists of a pair of coaxial electrodes which are fed by a low-inductance conductive path from an energy storage system such as a capacitor bank. The electrodes are surrounded by a vacuum chamber which is usually filled with hydrogen, or deuterium, in the pressure range of a fraction of a torr up to 20 torr.

The DPF is classified as to the geometry of its coaxial electrodes. The Mather geometry is characterized by an electrode whose length is much larger than the diameter; conversely, the Filippov geometry has an



electrode diameter much larger than the electrode length. A hybrid of these two, the Conrad geometry, has an electrode length equal to the diameter. The phenomena associated with the plasma focus are common to each of these geometries; however, discussion of the DPF discharge as it applies to geometry is restricted to the Mather configuration since this type was used exclusively throughout the investigation. A schematic of a Mather-type DPF is shown in Fig. II-1. A more detailed description of the particular device used in this investigation can be found in Chapter III.

Referring to Fig. II-1, breakdown initially occurs at (a) as a symmetric arrangement of streamers along the breech insulator between the inner electrode and the outer electrode backplate shortly after voltage is applied. A symmetric breakdown is essential to proper focus formation as reported elsewhere [5]. As the current increases in the discharge "sheath", Lorentz forces cause it to lift off the insulator surface and propagate radially toward the outer electrode. During this inverse pinch phase, the current sheath develops a distinctly parabolic shape due to the radial dependence of the magnetic pressure gradient associated with the magnetic field produced by the discharge current. Once the plasma sheath contacts the cylindrical surface of the outer electrode, it begins to accelerate toward the open end of the electrodes (b) in Fig. II-1. The discharge current continues to increase as the sheath propagates down the gun while simultaneously pushing, or snowplowing, the relatively cold plasma ahead of it. The outer electrode usually has an open structure so that much of the plasma is forced out of the gun by the snowplow action of the current sheath. By the time the sheath reaches the open end of the electrodes (c), it is moving at an almost constant velocity of about  $10^7$  cm/s [4,6-11].

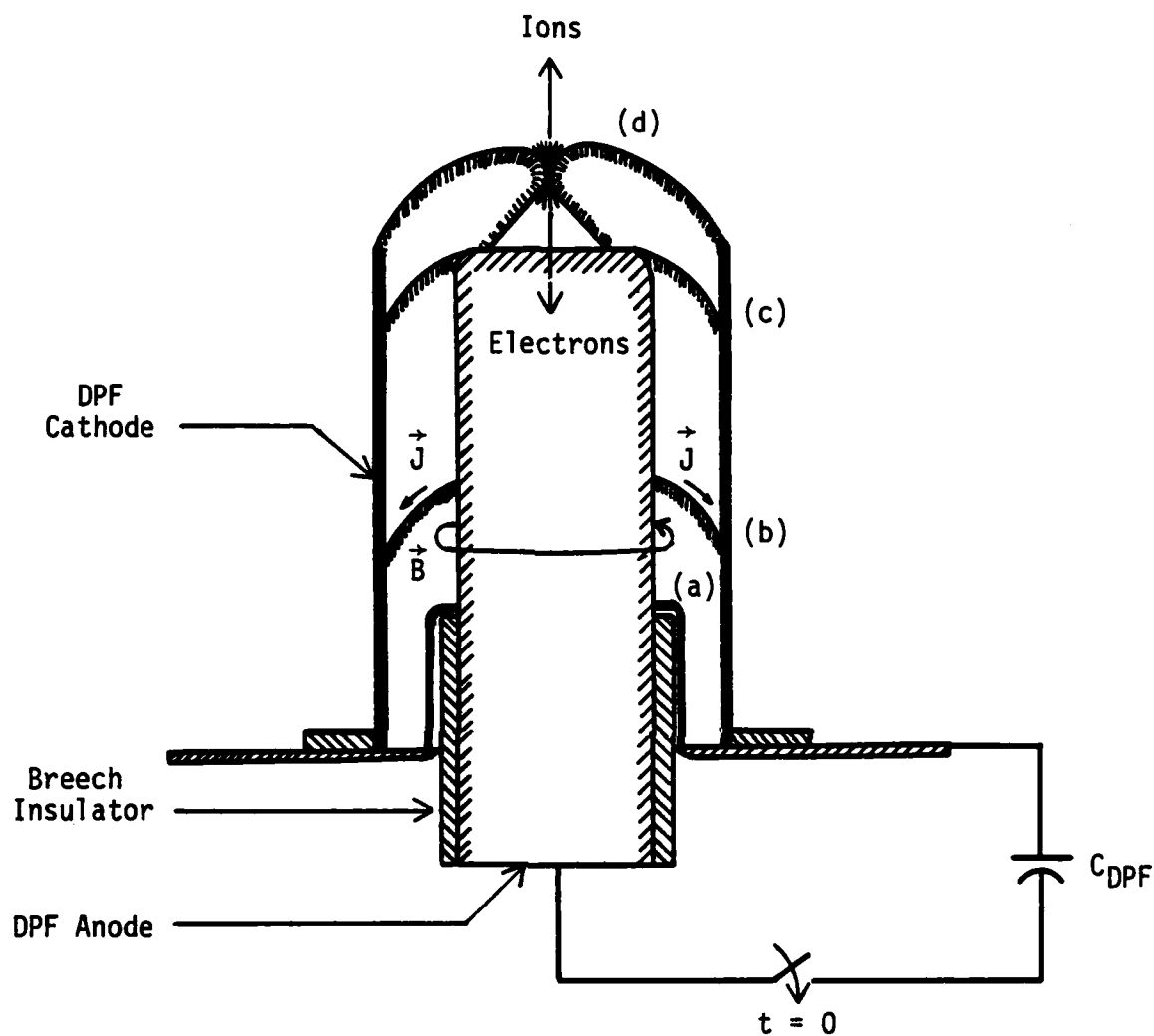


Fig. II-1. The temporal evolution of the Mather-type DPF discharge illustrating (a) the initial breakdown, (b) the acceleration of the plasma sheath toward the end of the electrodes, (c) the arrival of the sheath at the end of the electrodes, and (d) the ensuing plasma pinch.

The change in profile of the inner electrode boundary at the end of the gun causes a radial collapse of the sheath toward the axis of the DPF. The initial capacitor bank voltage and gas fill pressure are selected so that as the sheath collapses toward the axis, the discharge current approaches its maximum value. Consequently, the maximum amount of magnetically stored energy is available for conversion to plasma energy during the final stages of the collapse phase. The time interval between the initial breakdown and the end of the collapse phase is usually on the order of a few microseconds.

The radial collapse terminates with the rapid conversion of magnetically stored energy to plasma energy forming a dense plasma focus, or plasma pinch, as shown in Fig. II-1 at position (d). The focus contains about 10% of the gas swept up by the current sheath snowplow [11,12] and occurs on the axis, at the end of the inner electrode. The pinch volume is roughly cylindrical in shape having a diameter of a few millimeters (typically 2 mm to 3 mm) and a length of about a centimeter.

The development and subsequent decay processes of the dense plasma pinch are rather complex and not well understood. Most researchers agree that the pinch passes through several distinct phases. These phases, in the order that they occur, are as follows [9,12-15].

- (1) As the current sheath collapses, the relatively field-free snowplowed plasma is compressed to its maximum average density of  $10^{18} \text{ cm}^{-3}$  to  $10^{19} \text{ cm}^{-3}$  [4,6-11,15-17] and reaches a plasma temperature on the order of a kiloelectron volt [1,4,6,7,9,11,15-18]. This temperature is well above the typical temperature of 100 eV for ions and the somewhat lower temperature for electrons in the sheath during the collapse phase [7,8]. The actual

temperature of the plasma depends on the pressure mode in which the device is operated. In the low-pressure mode, where it has been observed that charged particle beam production is maximized [19], the plasma temperature is somewhat lower than for the high-pressure mode.

- (2) As the current sheath continues to collapse, a quasi-stable, intermediate phase follows the maximum compression phase in which the plasma density decreases as the pinched column expands against the collapsing current sheath. The collapse of the current sheath causes a change in inductance which produces an axial electric field proportional to  $I\dot{L}$  where  $I$  is the DPF discharge current and  $\dot{L}$  is the time derivative of the circuit inductance. This electric field is strong enough to significantly increase the electron turbulence and, hence, the plasma resistivity [7,13].
- (3) The increased electron turbulence precedes the onset of magnetohydrodynamic (MHD)-type  $m = 0$ , or sausage, instabilities. These instabilities, which are believed by some to develop in a background of other plasma instabilities [7,13,15,20], cause an anomalously rapid increase in the plasma resistivity resulting in very strong axial accelerating fields. At low pressures, both ions and electrons are accelerated parallel to the DPF axis by these fields to energies as high as a megaelectron volt [1,11,21-24]. The axial direction of the accelerating fields causes considerable anisotropy in the particles' velocity distribution with respect to the DPF axis, as observed by several

researchers [7,11,12,25]. Furthermore, the energies of particles ejected from the pinch have been observed to be charge dependent rather than mass dependent [11,22,23,26,27] suggesting behavior similar to that of a plasma filled diode. A strong correlation between the onset of  $m = 0$  instabilities and the beginning of hard x-ray and neutron emission [7,11], as well as the characteristic drop in the DPF discharge current [23], has also been observed.

- (4) Finally, the instabilities in the plasma cause expansion of the plasma column into the surrounding low-temperature gas, cooling the plasma and causing the plasma column to decay rapidly.

The existence of these phases, at least in part, has been experimentally verified by several researchers and has been observed to last for a total duration of about 100 ns [9-11].

Despite the apparent consensus regarding the different phases of the pinch evolution, there is some disagreement as to the appropriate theoretical model to use in explaining some of the observed characteristics of the DPF pinch. Since the DPF was originally thought to be applicable as a fusion reactor, most of the models presented in the literature are based on ion acceleration mechanisms which produce neutrons. Some of the more widely known models are listed as follows.

- (1) The thermal plasma model initially assumed that neutrons are produced by thermonuclear reactions in a stationary plasma volume; however, the model was later modified to a "moving boiler" model in which the thermonuclear plasma moves away from the center electrode at some velocity [4,28]. The "moving

boiler" model attempts to explain the experimentally observed, spatial anisotropy in the neutron energy spectrum but yields unrealistic values for the velocity of the plasma volume as it moves away from the electrode. Furthermore, the model fails to predict the existence of oppositely directed ion and electron beams.

- (2) The beam-target model assumes that ions accelerated away from the center electrode, presumably by plasma instabilities which occur in the dense plasma formed by the current sheath collapse, produce neutrons as they impinge on a stationary gas target comprised of the ambient fill gas. This model, as with the thermal plasma model, does not agree well with experimental observations since the observed duration of neutron production and total neutron flux imply unrealistically large values for the duration of the plasma instabilities and the ion beam current [29].
- (3) The converging ion model, which is similar in some respects to both the thermal plasma model and the beam-target model, assumes that at any given instant in time, neutrons are produced in a small plasma volume on the DPF axis by a three-dimensional convergence of isotropic ions as observed from the frame of reference of the plasma volume's center of mass. In the laboratory frame of reference, the plasma volume moves away from the DPF center electrode at some velocity and the ions are described by an anisotropic velocity distribution [29]. This model seems to predict the observed neutron anisotropy somewhat better than

either the thermal plasma model or the beam-target model; however, the mechanisms responsible for producing the required ion velocity distribution are not well described.

- (4) The crossed-field acceleration model is based on detailed calculation of charged particle trajectories which are determined by the changing electromagnetic field profile in the pinch volume [30-32]. Strong axial electric fields are produced as the magnetic structure of the collapsing current sheath decays. The electric and magnetic fields subsequently interact to produce charged particle trajectories which are somewhat curved. In addition to predicting the existence of axially directed, charged particle beams, the model may also help to validate the ion velocity distribution proposed by the converging ion model [29].
- (5) The MHD model formulates the focus formation entirely in terms of MHD equations. The subsequent solution of these equations predicts the various phases of the pinch, and the associated phenomena, to a remarkable degree [13,15]. However, several experimental phenomena (particularly, microscopic turbulence) have not been included in the theory and require further investigation [33].

Each of these models attempts, at least qualitatively, to explain one or more of the phenomena associated with the plasma focus. It is beyond the scope of this report to present the details of each of these models; however, additional information is available in the literature.

For a positive inner electrode polarity, the electron beam produced by the plasma focus has been shown to be directed toward the DPF inner

electrode [25]. Hard x-ray emission (e.g., greater than 10 keV), localized in the center of the electrode, has been shown by van Paassen et al. [34], Harries et al. [35], and others [1,18,19,36] to be the result of thick-target bremsstrahlung caused by an impinging electron beam with maximum energies greater than 350 keV. Harries et al. have also shown that electrons with energies greater than 30 keV travel almost parallel to the DPF axis with an angular spread of less than  $10^0$ ; however, lower energy electron trajectories have been measured at much larger angles. Gullickson and Barlett [36] have shown that the electrons in the beam have an average energy of 150 keV.

Correlation between the hard x-ray and neutron emission suggests that the electrons are accelerated by the same processes as the ions. This idea is supported by Stygar et al. [23], who have shown that the energy spectrum of the electron beam and oppositely directed ion beam follow the same power law. They have also shown that the electron beam current scales as the DPF discharge current, and they measured a maximum beam current of 17 kA for an initially stored energy of 12.5 kJ. Molen [1] has measured a maximum beam current of greater than 30 kA for electrons with energies greater than 150 keV for an initially stored energy of 17 kJ. Furthermore, the beam current can be shown to agree well with the power law of Stygar et al. Molen has also shown that the electron beam has a 2 ns to 5 ns risetime and a 5 ns to 25 ns pulsewidth.

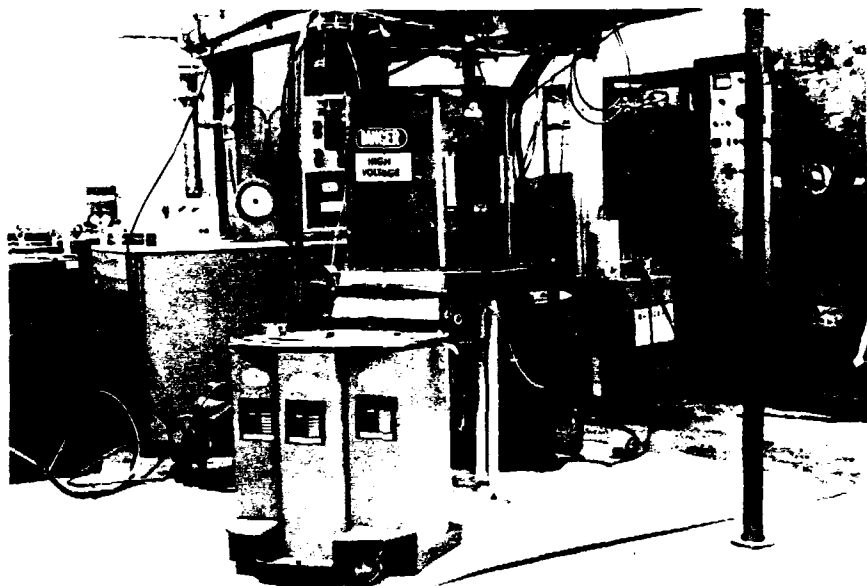


### Chapter III

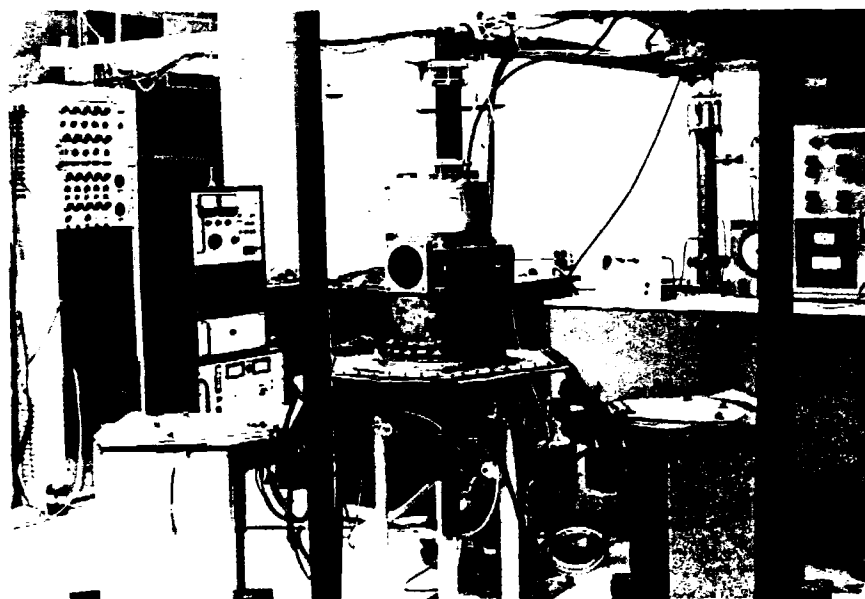
#### THE EXPERIMENTAL ARRANGEMENT

The experimental investigation was conducted using a 34-kJ DPF of the Mather geometry, a photograph of which appears in Fig. III-1. The device's coaxial electrodes, which are surrounded by a cylindrical aluminum vacuum chamber and a 5-mm-thick lead radiation shield, are fed by azimuthally symmetric, parallel-plate conductors which connect to four capacitor bank modules providing a total capacitance of 168  $\mu\text{F}$  with a maximum voltage rating of 20 kV. The device was operated with a reduced total capacitance of 84  $\mu\text{F}$  (two capacitor bank modules) and an initial stored energy in the range of 6 kJ to 11 kJ, corresponding to an initial capacitor bank charging voltage of 12 kV to 16 kV, respectively. Voltages less than the maximum 20 kV were used so as to reduce the probability of dielectric failure. The peak discharge current, as determined by the initial capacitor bank voltage, was in the range of 390 kA to 550 kA for the specified voltage range and was reached approximately 2.2  $\mu\text{s}$  after the initial breakdown. The fill-gas pressure was chosen so that the pinch occurred within 0.3  $\mu\text{s}$  of the peak current. Hydrogen, in the pressure range of 0.75 torr to 3.0 torr, was used throughout the investigation as the fill gas.

During the course of the experimental investigation, a system to guide the electron beam ejected from the pinch and a third (auxiliary) electrode, which is in addition to the anode and cathode of the DPF, were added to the device. Direct measurements of the electron beam were made



(a)



(b)

Fig. III-1. The DPF experimental apparatus (a) with the lead shield and (b) without the shield.

with a Faraday cup similar to those described elsewhere [1,37]. The DPF, the beam guiding system, the auxiliary electrode, and the Faraday cup are described in this chapter. Other diagnostic equipment and techniques, such as the Rogowski probe used to measure the DPF discharge current, PIN diodes, image converter camera, and x-ray pinhole photography, are described in Appendix A.

### The Dense Plasma Focus

The DPF used in these experiments was originally designed and constructed at The Aerospace Corporation in Los Angeles, California, where it was used in studies concerning the characterization of the electron beam ejected from the pinch region [1], x-ray spectral analysis [38], pinch characterization [1], and radiation effects on materials where the DPF was used as a photon source [2]. Some of the experimental results concerning the electron beam that were published by The Aerospace Corporation, where the beam was first observed, are verified during the course of this investigation and are used to evaluate the performance of the DPF subsequent to the modifications described in this chapter.

The Mather-type electrodes, as shown in Fig. III-2, are connected to copper backplates which are fed by the parallel-plate conductors. A Pyrex insulator, which extends 6.4 cm along the inner electrode (anode) from the outer electrode (cathode) backplate toward the open end of the electrodes, electrically isolates the DPF electrodes from each other in the breech region of the plasma gun. Nitrile o-rings are used to form a vacuum seal between the insulator and the DPF electrode backplates. The cathode is a 20.0-cm-long, 14.3-cm-ID copper cylinder perforated with evenly spaced, 1.0-cm-diameter circular holes over 45% of its surface area. Two different anodes were used both having a length of 24.4 cm, a 7.6-cm OD, and a

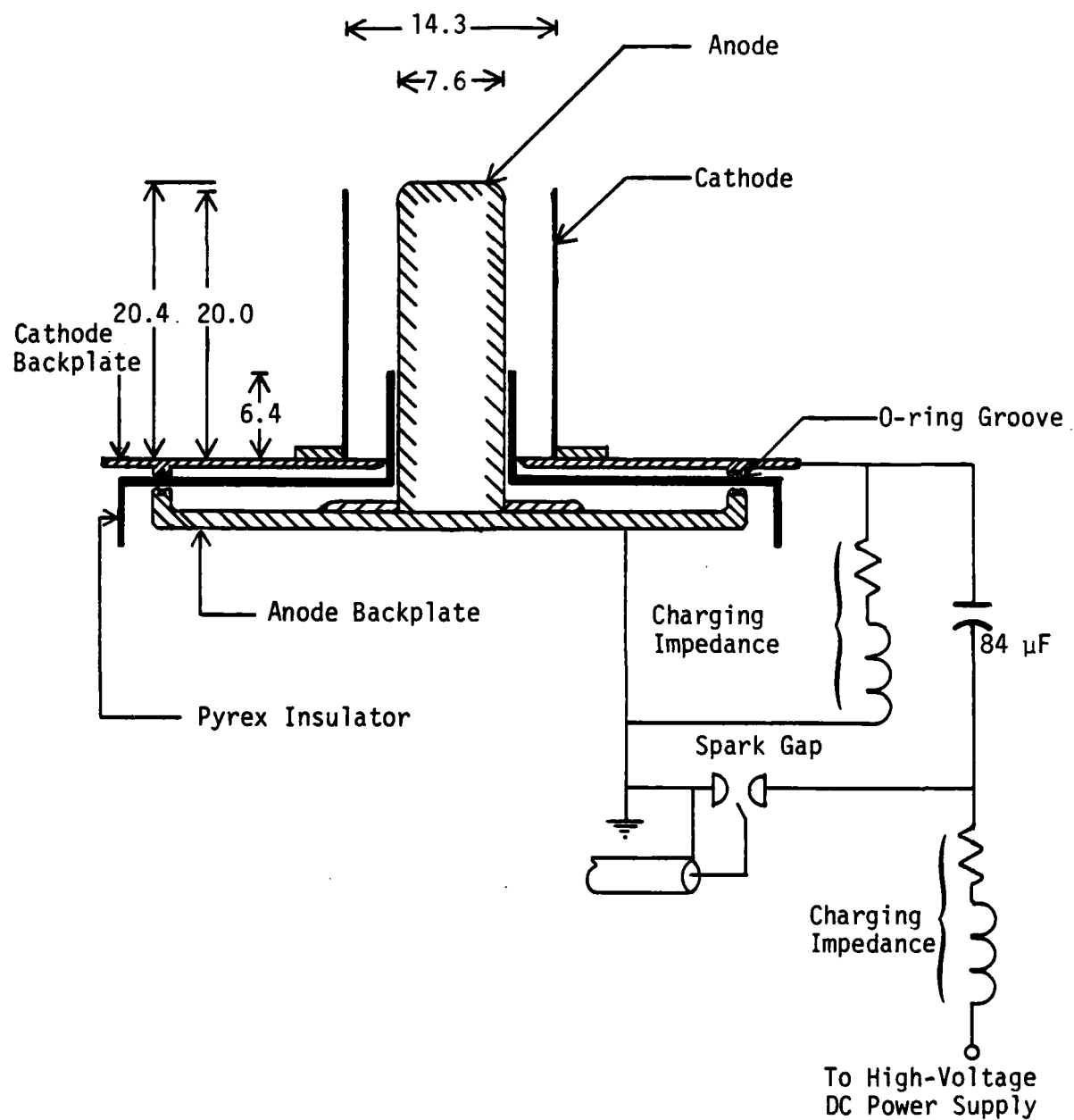


Fig. III-2. Schematic of the DPF with the vacuum vessel and drift tube assembly omitted for clarity. All dimensions are in centimeters.

1.5-cm-diameter hole drilled on the axis through the electrode so as to couple the electron beam from the pinch region into the drift tube. The two anodes differ in the configuration of the electron beam drift tube that was used with each. The first anode and drift tube that were used are shown in Fig. III-3 and were developed at The Aerospace Corporation. The drift tube, which is at the same pressure as the DPF chamber, consists of two sections of 4.9-cm-ID copper tubing between which a 5.1-cm-ID butterfly vacuum valve is inserted. The vacuum valve is necessary to facilitate maintenance of the beam diagnostic equipment which is located at the bottom of the lower drift tube section. The overall distance from the tip of the DPF anode to the bottom of the drift tube is 87.6 cm. The second anode, which is similar to the first, is inherently part of the beam guiding apparatus; consequently, further description of the anode and its complementary drift tube are deferred to a subsequent section of this chapter.

The parallel-plate conductors connect the DPF electrodes to the two capacitor bank modules which are symmetrically arranged. Each module consists of three Sangamo 14- $\mu$ F, low-inductance, energy-discharge capacitors which are connected in parallel for a total capacitance of 42  $\mu$ F and a maximum voltage rating of 20 kV. Each module is also equipped with a low-pressure trigatron spark gap and header plates for connection to the parallel-plate conductors. The inductance of the modules, parallel-plate conductors, and the DPF electrodes is estimated to be about 33 nH. A photograph of these elements without the vacuum vessel is shown in Fig. III-4. The capacitor bank modules are charged by a 6-kVA, dc power supply which is remotely controlled from inside a double-clad, copper screenroom by a modular control system. A multichannel, high-voltage pulse generator, having a risetime of 25 ns and a 25 kV peak output per

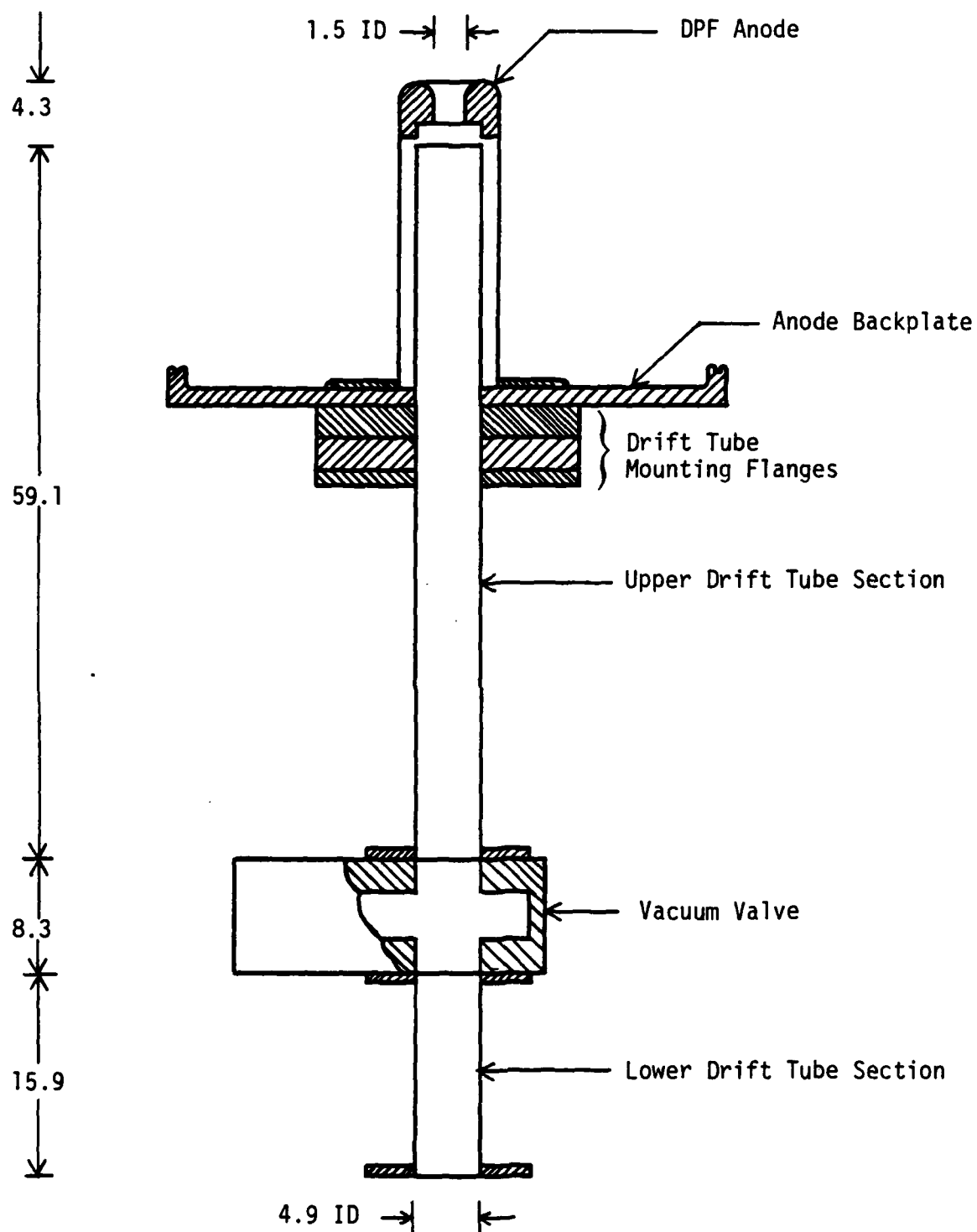
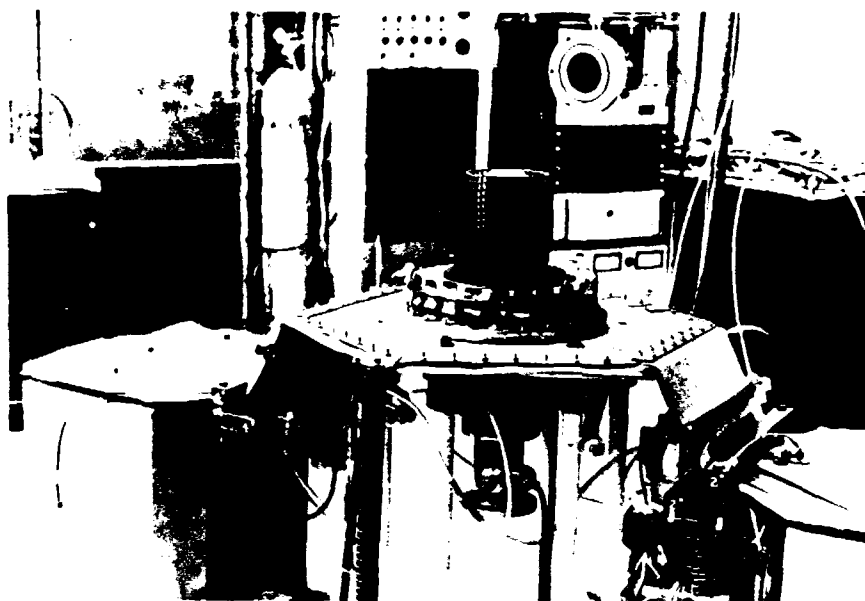
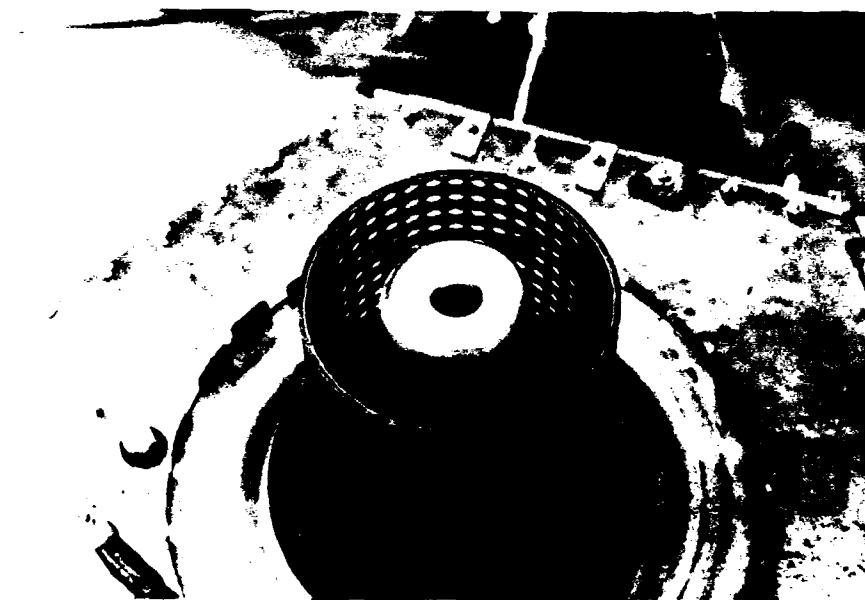


Fig. III-3. The initial DPF anode and electron beam drift tube assembly. All dimensions are in centimeters.



(a)



(b)

Fig. III-4. Photographs of the DPF apparatus illustrating (a) the electrodes, capacitor bank modules, parallel-plate conductor arrangement, and (b) close-up of the coaxial electrodes.

channel, is used to trigger the spark gaps with a relative jitter of less than 5 ns. A more detailed description of the control system and the pulse generator are presented in Appendices C and D, respectively.

The DPF's electrodes are enclosed inside a three-section cylindrical aluminum vacuum chamber which is vacuum sealed at one end by a circular aluminum lid and the other end by the cathode backplate. The upper section of the chamber is fitted with a vacuum port, the chamber lid and middle section contain diagnostic ports, and the bottom section functions as a spacer. The 29.7-cm-ID, 44.8-cm-long chamber is evacuated through a 7.6-cm-ID Pyrex process pipe by a 12.7-cm-diameter diffusion pump vacuum system to a base pressure of about  $10^{-6}$  torr. Nitrile o-rings are used to form vacuum seals throughout the system.

#### The Guiding Field Solenoid and Pulser Circuit

The magnetic field used to guide the electron beam from the pinch to the bottom of the drift tube is produced by a two-section solenoid that is constructed with PVC-insulated, 18-AWG stranded copper wire wound on a 4.5-cm-OD Pyrex tube that has a wall thickness of 2.4 mm. The axes of both solenoidal sections are aligned with the axis of the DPF, as shown in Fig. III-5, so that the solenoidal sections also function as the electron beam drift tube which is at the same pressure as the DPF discharge chamber. The solenoidal sections are mounted in separate cylindrical copper chambers which are separated by an 8.9-cm-ID butterfly vacuum valve when assembled on the DPF. Each chamber is also equipped with vacuum-quality electrical feedthroughs. The distance from the top of the DPF anode to the bottom of the solenoid is 65.8 cm.

To provide a path for the electron beam return current (see Chapter V, Theoretical Considerations, for further explanation), each of the Pyrex



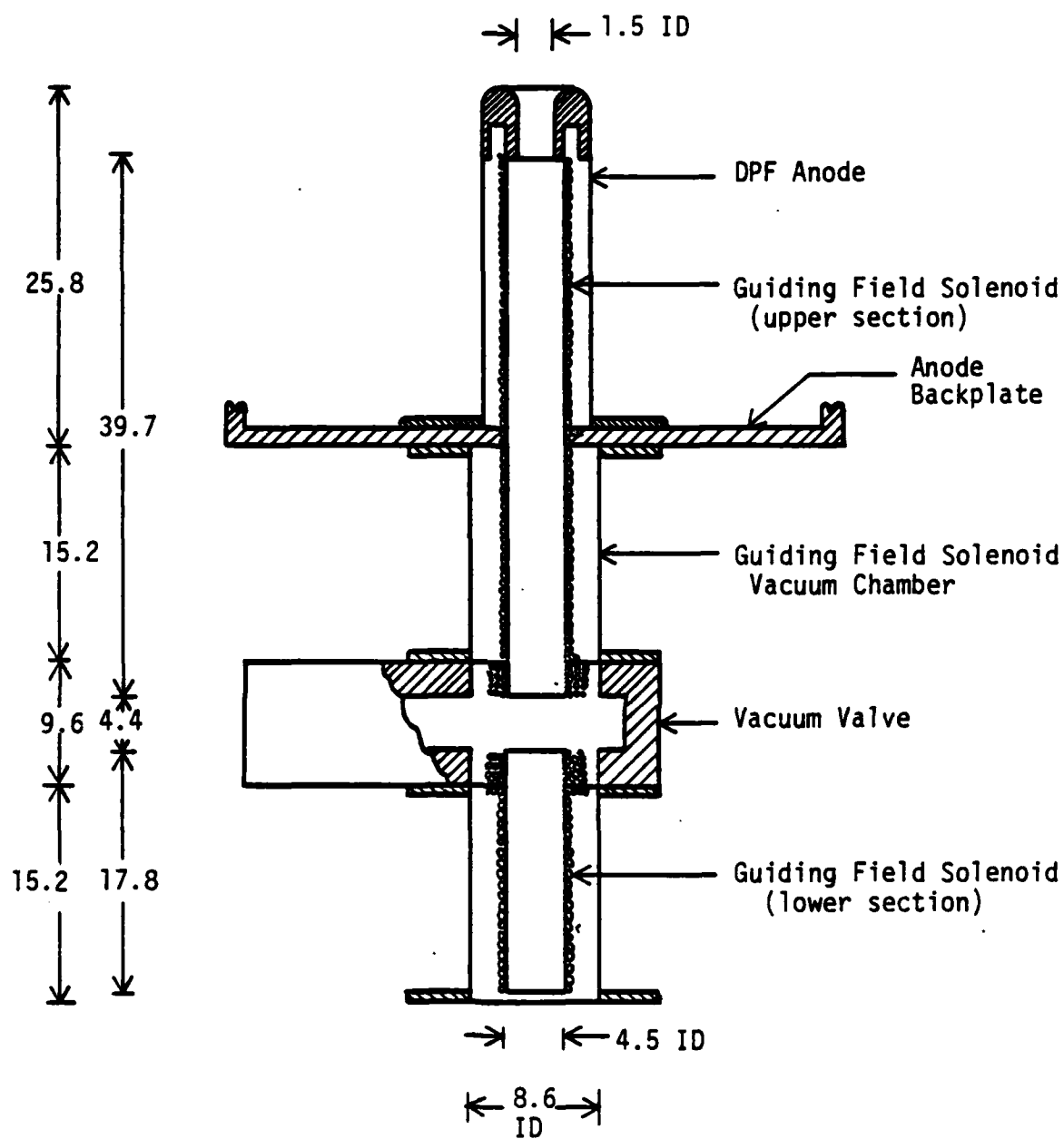


Fig. III-5. The DPF anode and the guiding field solenoid apparatus. The solenoid's electrical connections and structural support are omitted for clarity. All dimensions are in centimeters.

sections is lined with 0.25-mm-thick copper foil which is electrically grounded at both ends of the solenoidal sections when assembled on the DPF. The edges of the coiled copper foil are separated by a 6.0-mm gap along the length of each solenoidal section so that diffusion of the magnetic guiding field into the drift region is not impeded by eddy currents induced in the copper liner.

The magnetic field strength in the vicinity of the vacuum valve is tailored so that the minimum value on the axis between the ends of the solenoidal sections is within a factor of two of the magnetic field strength on the axis inside the solenoid. This is accomplished by adding extra turns to the ends of the solenoidal sections closest to the vacuum valve as detailed in Appendix B.

The design criteria for the circuit which pulses the field coil are as follows.

- (1) The duration of the current pulse to the solenoid should be long in comparison to the  $2.2 \mu\text{s}$  duration of the plasma focus discharge so that the magnetic field inside the beam guiding solenoid is essentially constant.
- (2) The current pulse should be sufficiently short so as to prevent diffusion of the magnetic guiding field through the wall of the DPF anode. Given that the anode is made of copper and imposing the restriction that the magnetic flux be confined to within a depth of 1 mm of the anode's inside surface, the current pulse must have an initial sinusoidal time-to-peak of less than 1.5 ms [39].
- (3) The magnetic field inside the solenoid should be of sufficient strength so that the Larmor radii of the electrons ejected from

the pinch are smaller than the inner radius of the drift tube. Assuming that the beam source is on the DPF axis and flush with the anode end, the angle at which propagation of the beam can deviate from the axis is limited to a maximum of  $10^\circ$  by the aperture in the end of the anode where the beam originates. If the Larmor radius of a typical electron ( $E \approx 150$  keV) in such a beam is to have a maximum value of 1 cm, then the magnetic flux density must be at least 0.023 T (see Chapter V).

The pulser circuit for the solenoid is shown schematically in Fig. III-6. The circuit is a critically damped RLC network with a time-to-peak of approximately 165  $\mu$ s (Fig. III-7); consequently, the current pulse is within 1% of its maximum value for about 46  $\mu$ s. The guiding field solenoid is energized by discharging the 14- $\mu$ F capacitor, which is initially charged to some preselected voltage, through the solenoid using an ignitron. The total series inductance of the circuit was made much larger than the inductance of the guiding field solenoid so as to allow considerable freedom in the choice of the solenoid geometry and to limit the maximum transient voltage drop across the solenoid. At the time of maximum current, only 3.3% of the initially stored energy is stored in the guiding field solenoid, 10.2% of the energy is stored in the external inductor, and a considerable amount of the energy (32.4%) has been dissipated in the series resistance. The apparently poor efficiency of the energy transfer to the guiding field solenoid was not a major consideration since the circuit design was the simplest for the components available.

Vacuum feedthroughs, which are used as electrical connectors for the guiding field solenoid, limit the maximum transient voltage drop across the solenoid to about 1.2 kV. Consequently, the maximum initial capacitor

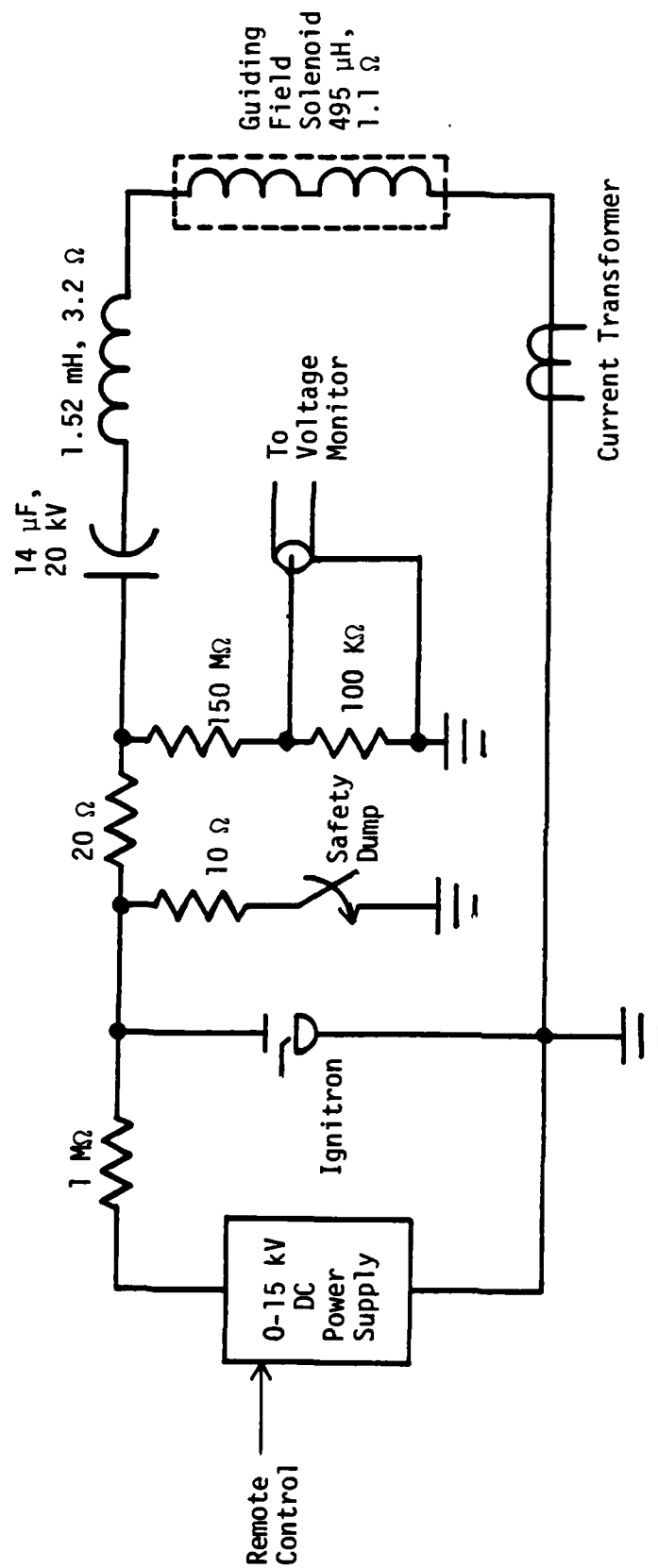


Fig. III-6. Schematic of the guiding field solenoid pulser circuit.

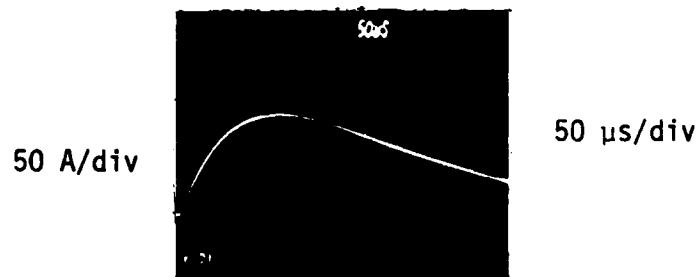


Fig. III-7. The guiding field solenoid current for a capacitor voltage of 5.0 kV.

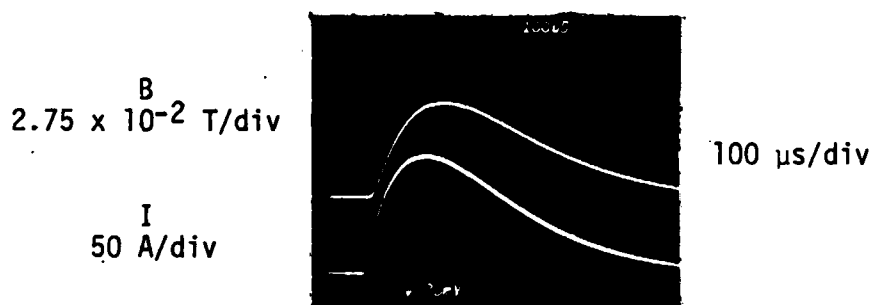


Fig. III-8. The guiding field magnetic flux density (upper trace) and corresponding solenoid current (lower trace) for a capacitor voltage of 5.0 kV.

voltage can be no more than 5.0 kV for the coil inductance selected, thus limiting the maximum peak current through the solenoid to approximately 150 A. The magnetic flux density on the axis, within the interior of the solenoid was found to be 0.072 T at the rated current (Fig. III-8) which is within a factor of 1.3 of the design value of 0.094 T. Furthermore, eddy currents induced in the anode material in the region of the anode aperture prevent the guiding field from diffusing into the DPF pinch region. The flux density was measured with the  $\dot{B}$  probe and integrator described in Appendix A.

#### The Auxiliary Electrode

The auxiliary electrode is located on the axis of the DPF as shown in Fig. III-9. The electrode consists of a 1.3-cm-diameter brass rod to which a brass knob with a molybdenum tip is attached. The brass rod is supported inside a nylon housing by a brass vacuum fitting attached at one end. The electrode was constructed so that the separation between the electrode tip and the DPF anode could be varied over a range of 5.1 cm to 25.4 cm. A 7.6-cm vacuum chamber extension, as shown in Fig. III-9, was used to achieve electrode separations greater than 17.8 cm.

As mentioned in Chapter I, part of this investigation originated from a study of the use of the DPF as an opening switch in an inductive energy storage scheme. The circuit used in that investigation is shown in Fig. III-10 and includes, in addition to the DPF, a series RLC network having a total capacitance of 400  $\mu\text{F}$  with a maximum voltage rating of 9 kV, a total inductance of about 50  $\mu\text{H}$  (including stray inductance), and a stray resistance of about 60  $\text{m}\Omega$ . The capacitor bank was constructed in a modular form so that the capacitance could be varied in 66.7- $\mu\text{F}$  increments up to 400  $\mu\text{F}$ .

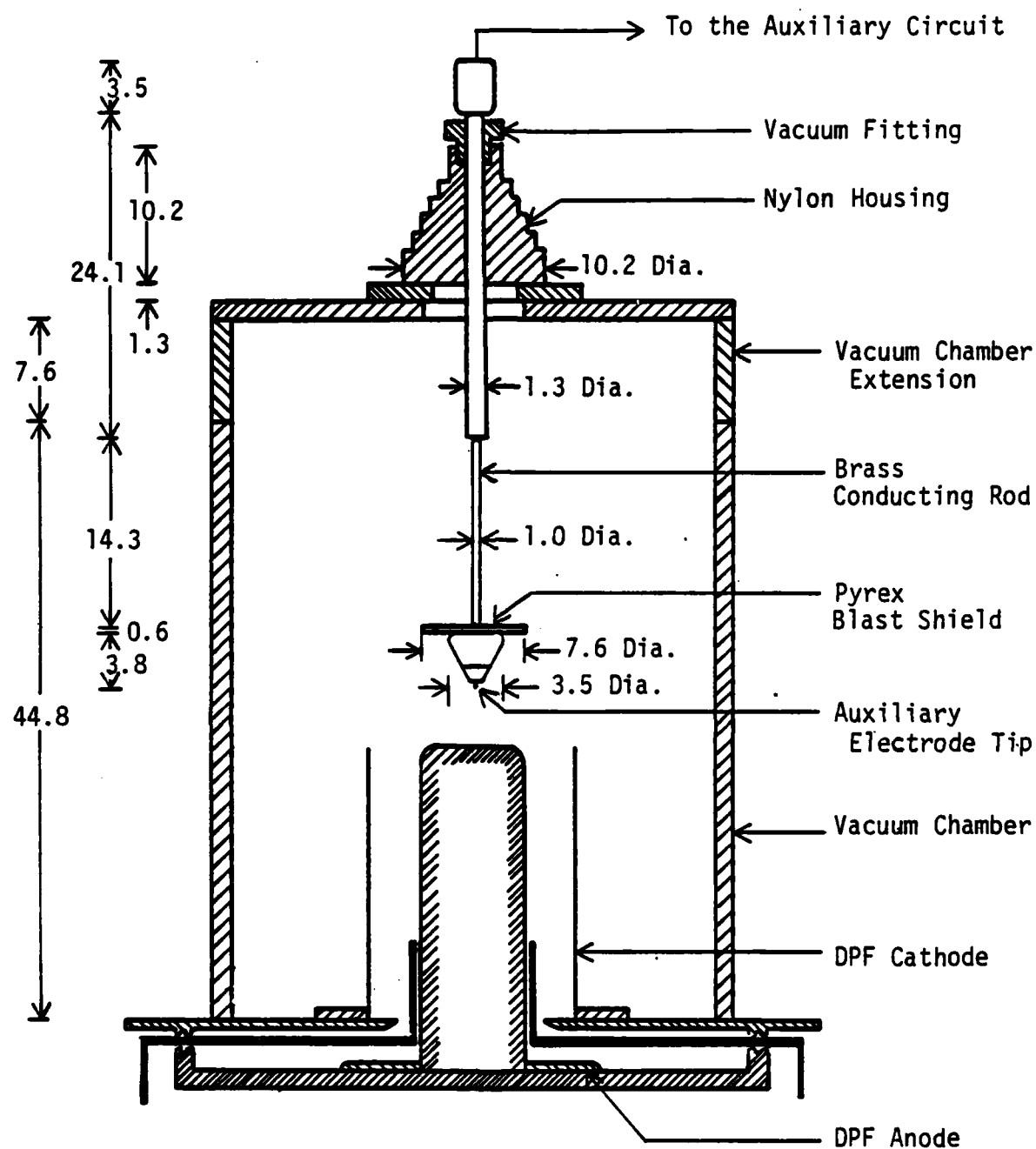


Fig. III-9. The arrangement of the DPF electrodes and the auxiliary electrode used in the investigation. All dimensions are in centimeters.

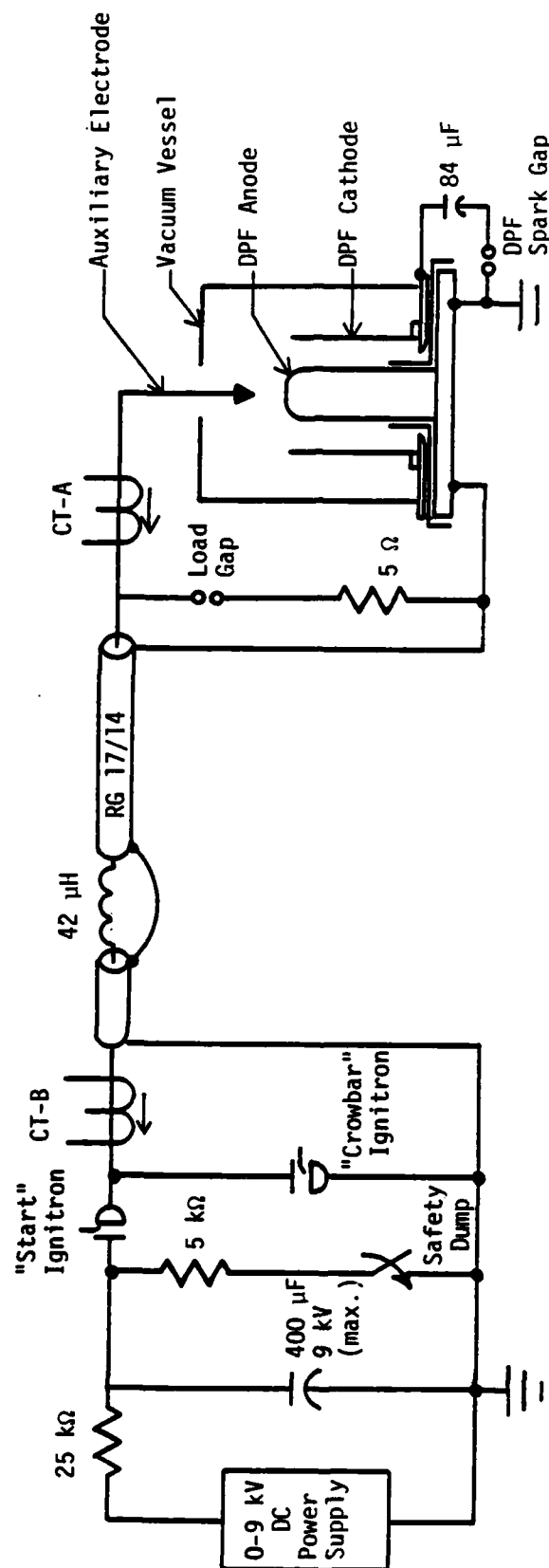


Fig. III-10. The DPF shown connected to the inductive energy storage circuit. Current transformers (CT-A and CT-B) were used to monitor the current in the circuit. The reference arrows shown below the transformers indicate the direction of conventional current flow which produces a positive signal.



The "start" ignitron connects the capacitor bank to the auxiliary electrode causing an arc to form between the electrode and the DPF anode. Once the current through the series inductor reaches a maximum, the "crowbar" ignitron closes and the energy in the inductor begins to decay slowly. This results in an almost constant current over the lifetime of the plasma focus discharge. If this current is then interrupted by the plasma focus, the  $L\dot{I}$  voltage generated across the inductor closes the load gap and transfers some of the inductively stored energy to the 5- $\Omega$  load resistor [40]. Six copper sulfate solution resistors, with a nominal resistance of 30  $\Omega$  each, are connected in parallel to produce the 5- $\Omega$  load. To minimize inductance, the six resistors are symmetrically arranged around the DPF and each resistor is fed by a separate high-voltage cable from the load gap. The load gap is a modified 100-kV spark gap (manufactured by Maxwell Laboratories, Inc.) set to statically break down at approximately 13 kV when filled with  $N_2$  at 760 torr.

#### The Faraday Cup

A Faraday cup was used to make direct measurements of the electron beam current ejected from the pinch by intercepting the beam with a suitable charge collector and subsequently measuring the voltage across a low-resistance shunt to ground. The charge collector and the shunt are arranged in a coaxial geometry to minimize the risetime. The peak voltage developed across the shunt is proportional to the peak electron beam current while the "tail" of the signal is proportional to the  $L/R$  decay of the charge deposited in the collector.

The device, shown schematically in Fig. III-11 and photographed in Fig. III-12, consists of a cylindrical graphite charge collector with a 6.4-cm OD and a 6.4-cm length which is surrounded by a single layer,

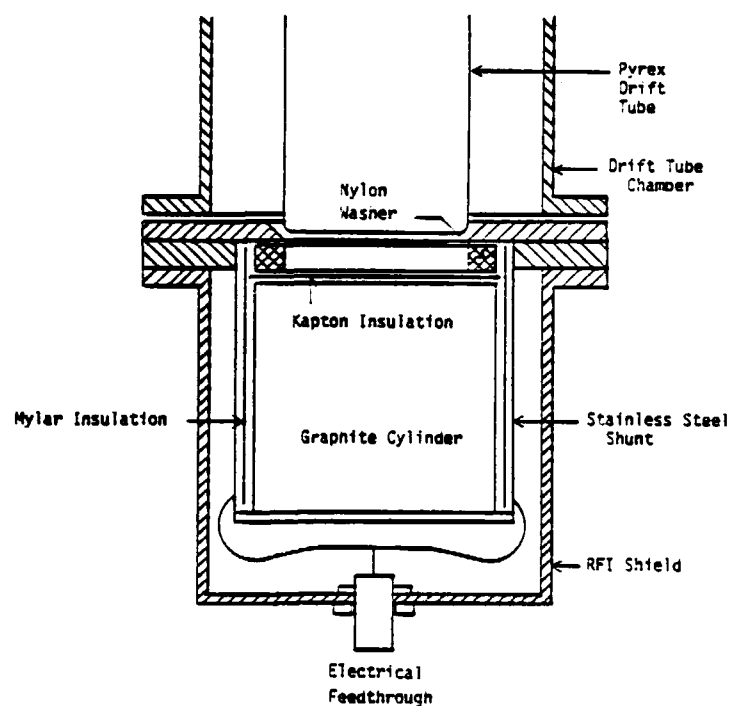


Fig. III-11. Schematic of the Faraday Cup shown attached to the guiding field drift tube.

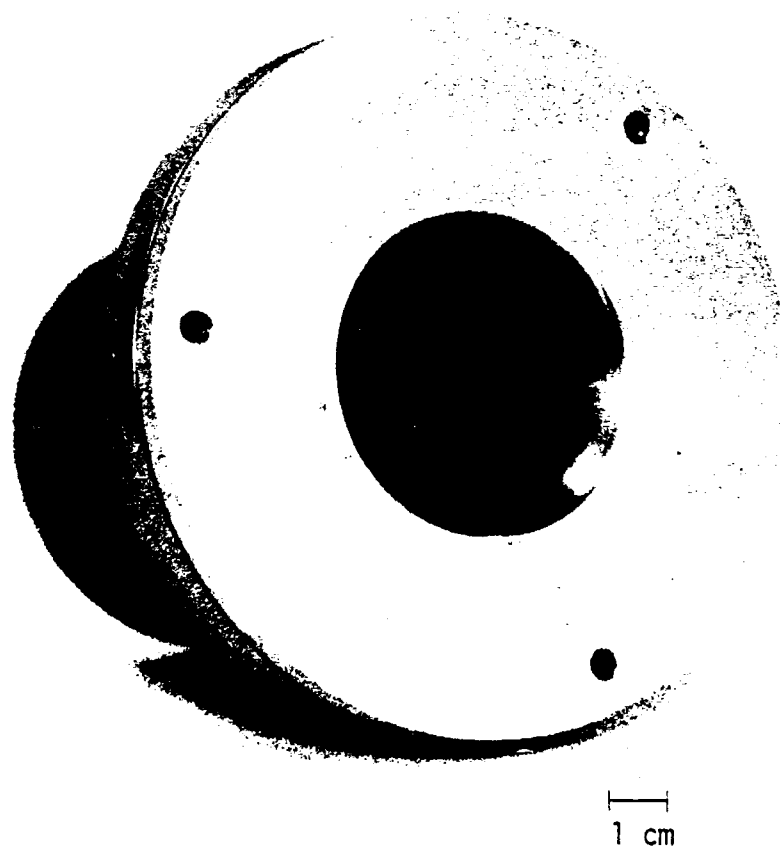


Fig. III-12. Photograph of the Faraday Cup.

0.025-mm-thick stainless steel current shunt. Graphite was chosen as the charge collector because of its high electrical conductivity, high ablation resistance, and low secondary electron emissivity. The stainless steel foil cylinder, chosen for its relatively high resistance and structural strength, is soldered to a brass disk at one end and a brass vacuum flange at the other. The resistance of the foil resistor between the disk and the flange is calculated to be  $8.8 \text{ m}\Omega$ . The graphite charge collector is insulated from the foil resistor and the brass vacuum flange by several layers of 0.2-mm Mylar film and is attached to the brass disk with Ag-filled epoxy ( $\rho = 2 \times 10^{-4} \text{ }\Omega\text{-cm}$ ). Four symmetrically arranged copper straps soldered to the outside of the current shunt at the brass disk feed a 50- $\Omega$  coaxial line. The entire Faraday cup assembly is inserted into a thick, copper RFI shield which also serves as a vacuum vessel. A vacuum flange and a nylon washer hold a thin sheet of Kapton insulation on the exposed face of the graphite charge collector so that the Faraday cup is not shorted to ground by the background plasma which accompanies the electron beam. The Kapton sheet required periodic replacement because of damage caused by both the electron beam and the background plasma. A 0.13-mm-thick sheet was found to have a reasonable lifetime; however, it has the adverse effect of eliminating electrons with energies less than 150 keV which might otherwise contribute significantly to the beam current.

The Faraday cup can be modeled as a short-circuited, lossy, coaxial transmission line with a one-way transit time of

$$\tau = \sqrt{\epsilon_r} \frac{L}{c} \approx 0.34 \text{ ns} \quad (\text{III-1})$$

where  $\epsilon_r \approx 2.5$  for Mylar,  $l$  is the length of the charge collector, and  $c$  is the speed of light. Furthermore, the total inductance of the cup for a uniform current distribution is calculated as

$$L = \frac{\mu_0}{2\pi} l \ln\left(\frac{b}{a}\right) \approx 0.30 \text{ nH} \quad (\text{III-2})$$

where  $\mu_0$  is the permeability of free space,  $a$  is the outer diameter of the charge collector, and  $b$  is the inner diameter of the stainless steel shunt. The actual inductance may be somewhat higher since the current distribution depends on the electron beam diameter which may be substantially less than the diameter of the charge collector.

A current injected into the charge collector induces an image current on the inner surface of the stainless steel cylinder; however, a signal does not appear at the output terminal until the current diffuses through the stainless steel foil. The ratio of the current on the outer surface ( $I_o$ ) to the current on the inner surface ( $I_i$ ) of the foil for a steady-state signal with a radian frequency of  $\omega$  is given by

$$\frac{I_o}{I_i} = \exp\left[-d\left(\frac{\omega\sigma\mu}{2}\right)^{\frac{1}{2}}\right] \quad (\text{III-3})$$

where  $d$  is the thickness of the foil,  $\sigma$  is the conductivity of the conductor, and  $\mu$  is the permeability of the conductor [37]. Hence, Eq. (III-3) shows that the Faraday cup acts as a low pass filter. As a worst-case estimate of the Faraday cup risetime, it is assumed that the relationship between the 10% to 90% risetime and the bandwidth of the cup can be approximated by that of a multi-pole filter,

$$\tau_r B_w \approx 0.5 \quad (\text{III-4})$$

where  $\tau_r$  is the risetime in seconds and  $B_w$  is the bandwidth in hertz. Furthermore, if it is assumed that the bandwidth is given by the frequency where the expression in Eq. (III-3) is  $e^{-1}$  and given that  $\epsilon = 0.11 \times 10^{-7}$  v/m, Eqs. (III-3) and (III-4) predict a risetime of approximately 1.4 ns.

The Faraday cup was calibrated using the circuit shown in Fig. III-13. The output of the pulse generator is a square pulse with a 2-ns risetime, 225-V peak, and 10-ns duration. Given the non-zero risetime of the input pulse, Fig. III-14 shows that the Faraday cup has a risetime of less than 3 ns corresponding to a bandwidth of greater than 160 MHz by Eq. (III-4). The foil shunt resistance can be calculated from the signal in Fig. III-14 to be 8.0 m $\Omega$  which is in good agreement with the theoretical value of 8.8 m $\Omega$ .

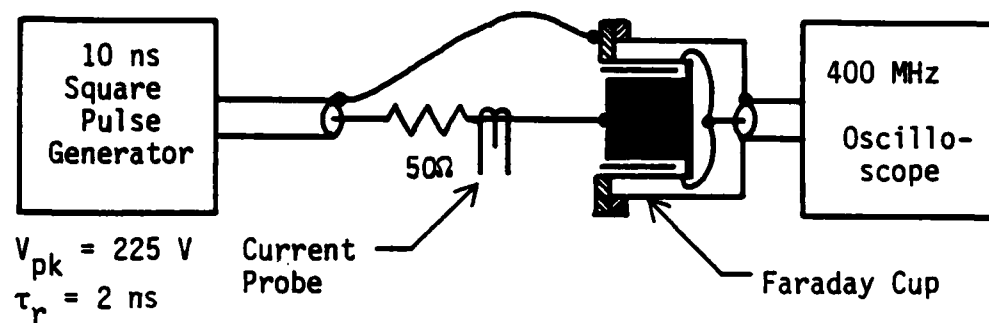
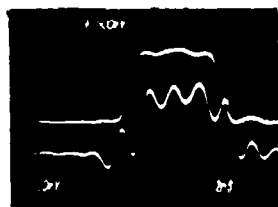


Fig. III-13. The Faraday cup calibration circuit.

Input Current  
1 A/div

Cup Response  
10 mV/div



2 ns/div

Fig. III-14. Faraday cup calibration illustrating the injected current (upper trace) and the cup response (lower trace).

## Chapter IV

### EXPERIMENTAL RESULTS

The primary goals of this investigation were to develop an electron beam guiding system to aid the propagation of the electron beam ejected from the DPF pinch and to investigate the effect of an auxiliary electrode on the DPF pinch phenomena, particularly on the electron beam. Typical DPF performance data, experimental results, and details of diagnostic arrangements as they apply to specific experiments are described in this chapter. The typical performance data, which are in good agreement with expectations, are used as a basis for evaluating the performance of the beam guiding system and to assess the effect of the auxiliary electrode on the DPF characteristics.

#### Typical DPF Performance Data

The performance of the DPF can be evaluated using any number of criteria, such as peak discharge current, time derivative of the discharge current, x-ray emission, neutron production, etc. For this investigation, the performance of the DPF was characterized by the following:

- (1) the DPF discharge current as measured by a calibrated Rogowski probe;
- (2) the motion of the axially collapsing current sheath recorded with an image converter camera in both the streak mode and the framing mode;

- (3) the spatially resolved emission of soft x rays from the pinch region recorded on x-ray pinhole photographs;
- (4) the temporally resolved emission of x rays from thick-target bremsstrahlung produced in an aluminum target placed in the path of the electron beam as detected by PIN diodes with different levels of filtration; and
- (5) the electron beam current as measured by a Faraday cup.

A description of each of these diagnostic elements and techniques is presented in Appendix A with the exception of the Faraday cup which is described in Chapter III. The data presented in this section are typical of the initial anode and drift tube configuration as well as the beam guiding apparatus when the guiding field solenoid is not energized. As such, these data provide a basis for the evaluation of the DPF performance in the beam guiding experiments and the auxiliary electrode experiments.

A representative Rogowski probe signal of the DPF discharge current is shown in Fig. IV-1. For an initial capacitor bank voltage ( $V_0$ ) of 16 kV ( $E_0 = 11$  kJ) and fill-gas pressure ( $P_0$ ) of 1.25 torr, Fig. IV-1 shows that the maximum current of 550 kA is reached about 2.2  $\mu$ s after initial breakdown and is followed 150 ns to 200 ns later by the characteristic rapid decrease in current, indicative of the pinch. An optical data link was used with the Rogowski probe for high-voltage isolation; however, x-ray fluorescence of the data link's optical fiber resulted in a sharp, positive spike just prior to the beginning of the decrease in current as evident in the figure. The inherent time-delay in the transmitter of the data link causes the spike to appear as if it occurs before the pinch. In fact, the transmitter introduces a delay of approximately 100 ns which implies that the spike occurs at about the time of the decrease in current.



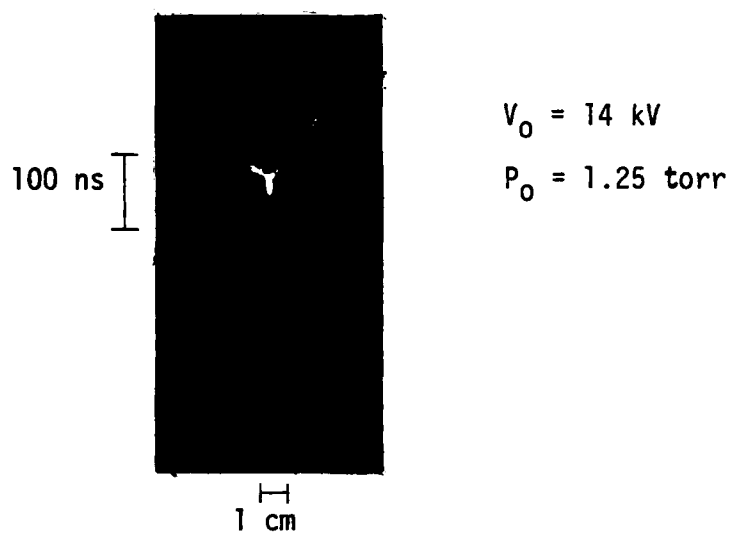


Fig. IV-1. The DPF discharge current for operation with  $V_0 = 16$  kV and  $P_0 = 1.25$  torr.

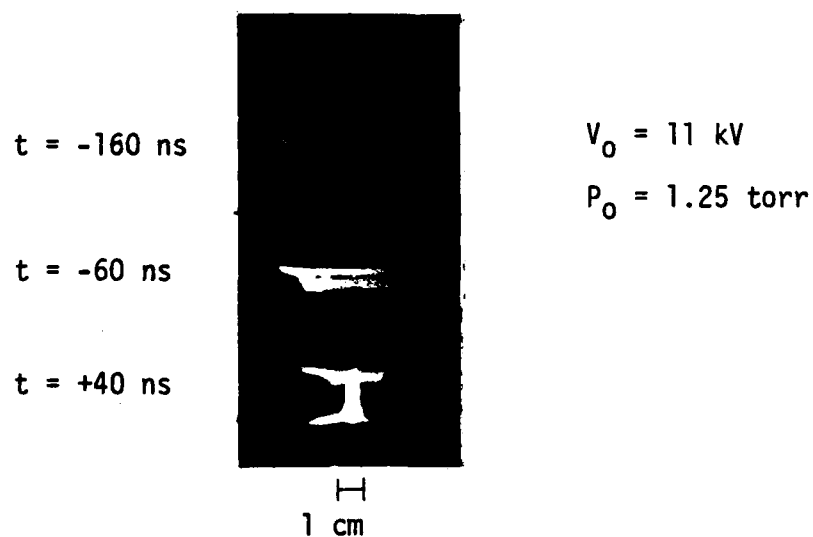
The time-to-peak of the DPF discharge current is essentially unaffected by the initial capacitor bank voltage and fill-gas pressure; however, the occurrence of the pinch relative to the peak current is a function of both parameters. These parameters were selected so that the pinch occurred within 300 ns of the peak current. An initial capacitor bank voltage of 16 kV and a fill-gas pressure of 1.25 torr were experimentally found to yield the most reproducible electron beam data.

Referring to Fig. IV-1, there appears a very sharp drop in the current at the pinch, after which the current returns to about 75% of its maximum value. A significant electron beam was usually measured when this behavior was observed. The presence of this current "spike" was predicted by a lumped-parameter computer simulation of the DPF done by Knapp [3]. In that study, the temporal characteristics of the spike were found to depend on the time evolution of the anomalous resistivity in the pinched column. This resistive phase has been shown by others to result in strong axial accelerating fields (see Chapter II).

Typical image converter photographs of the collapsing current sheath and resulting pinch are presented in Fig. IV-2. The streak photograph (Fig. IV-2(a)) was taken through a 0.13-mm-wide slit oriented parallel to the anode surface with the camera focused on the DPF axis, 6.4 mm from the end of the anode. The collapse velocity of the current sheath for an initial capacitor bank voltage of 14 kV and fill-gas pressure of 2.0 torr is calculated from the streak photograph to be  $2.0 \times 10^7$  cm/s which is in good agreement with values reported elsewhere (see Chapter II). Increasing the capacitor bank voltage or decreasing the pressure increases the sheath velocity somewhat; however, the velocity remains on the order of  $10^7$  cm/s. The framing photograph (Fig. IV-2(b)), for an initial capacitor



(a)



(b)

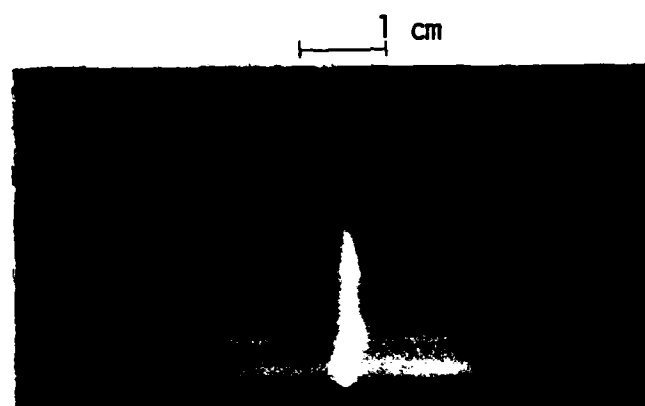
Fig. IV-2. Typical image converter camera photographs showing (a) a 500 ns streak photograph, and (b) a framing photograph with a 20 ns shutter speed and 100 ns frame separation where  $t = 0$  corresponds to the initial DPF x-ray pulse.

bank voltage of 11 kV and fill-gas pressure of 2.1 torr, illustrates the structure of the sheath as it collapses toward the axis. A short, 4.8-mm-diameter molybdenum rod was placed on the anode to mark the axis of the DPF.

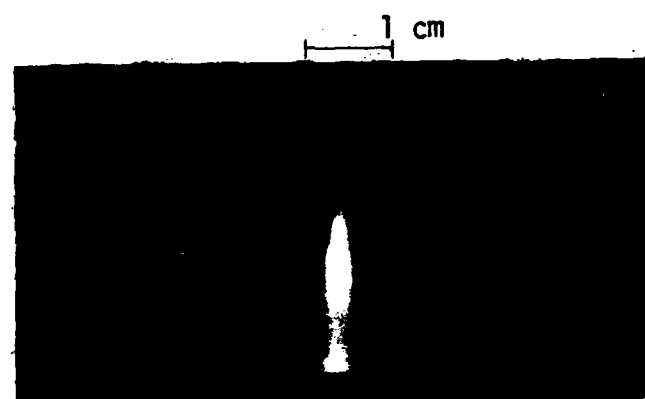
Soft x-ray pinhole photography, as shown in Fig. IV-3, records the spatial distribution of soft x-ray sources in the pinch region. The x-ray flux is time-integrated by the photographic film; consequently, the pinhole photograph does not contain information about the temporal development of the x-ray sources. The inherent nonreproducibility of the DPF discharge yields a unique pinhole photograph for each discharge; however, each of the photographs has several features in common.

- (1) The most intense emission occurs in a cylindrical volume on the axis of the DPF.
- (2) The cylindrical column often exhibits local constrictions indicative of MHD-type  $m = 0$  instabilities (Fig. IV-3(b)).
- (3) The outline of the DPF anode is usually visible as a result of bremsstrahlung from electrons accelerated in the sheath as it collapses toward the axis.

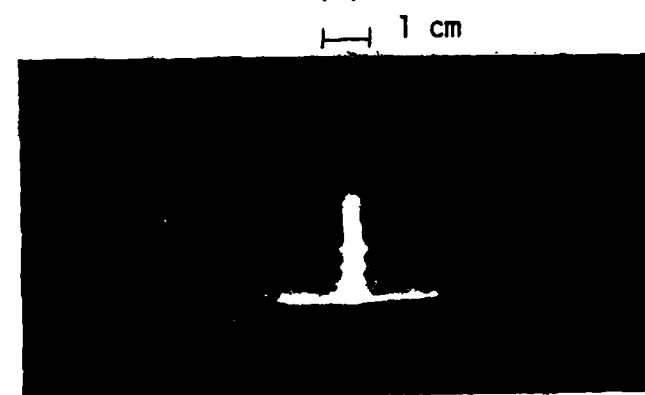
The initial capacitor bank voltage and fill-gas pressure have little effect on the pinhole photographs; however, the introduction of a small amount of high-Z gas, such as  $N_2$ , enhances soft x-ray emission (Fig. IV-3(c)) due to bremsstrahlung from electrons colliding with nitrogen molecules and K-line emission from the nitrogen. The capacitor bank voltage, the fill-gas pressure, and the magnification are indicated in Fig. IV-3 for each of the three photographs.



(a)

 $V_0 = 15 \text{ kV}$  $P_0 = 2.0 \text{ torr}$ 

(b)

 $V_0 = 14 \text{ kV}$  $P_0 = 2.0 \text{ torr}$ 

(c)

 $V_0 = 16 \text{ kV}$  $P_0 = 1.0 \text{ torr}$   
 $+ 0.15 \text{ torr N}_2$ 

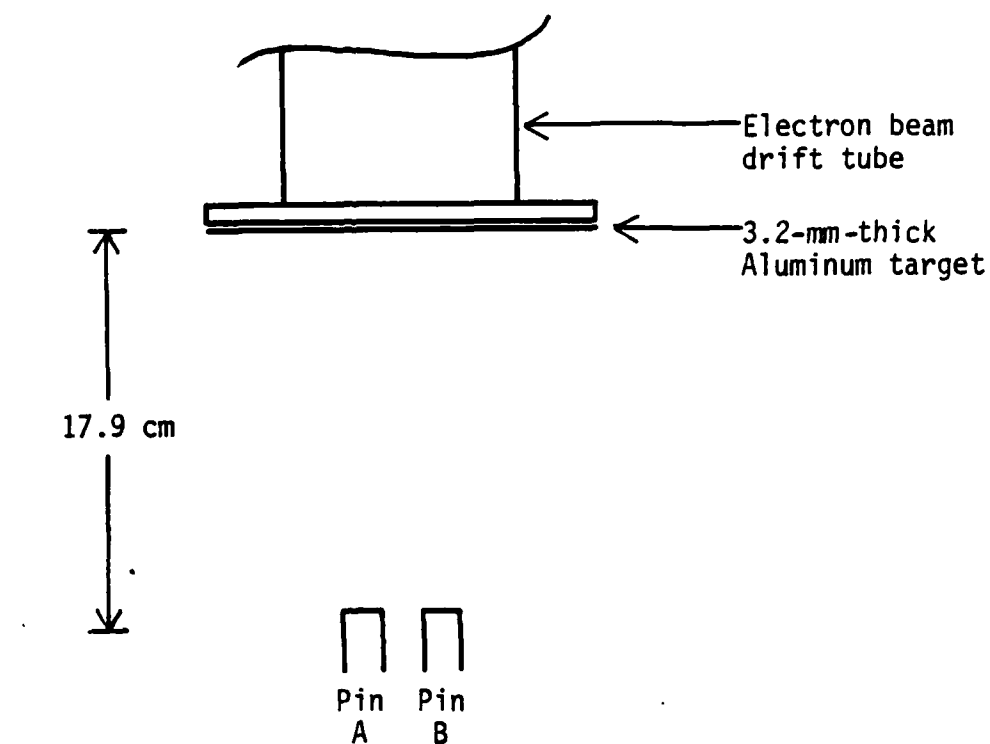
Fig. IV-3. Typical soft x-ray pinhole photographs.

Time-resolved measurements of thick-target bremsstrahlung caused by the DPF electron beam were made using the experimental arrangement shown in Fig. IV-4(a) in which the beam was intercepted by a 3.2-mm-thick aluminum target located at the end of the drift tube. Typical PIN diode signals for this arrangement are shown in Fig. IV-4(b). The signals were shifted by approximately 10 ns relative to each other for signal clarity. The upper and lower traces are the outputs of PIN diodes with intrinsic regions of 20  $\mu\text{m}$  and 125  $\mu\text{m}$ , respectively. The 20- $\mu\text{m}$  diode is filtered only by the 3.2-mm aluminum target while the 125- $\mu\text{m}$  diode has an additional 1.0 mm of Pb filtration, thus giving  $e^{-1}$  transmissions of 40 keV and 300 keV, respectively. In these experiments, only the relative response of the detectors are compared, and no attempt is made to calculate the x-ray flux since knowledge of the electron beam energy spectrum is required.

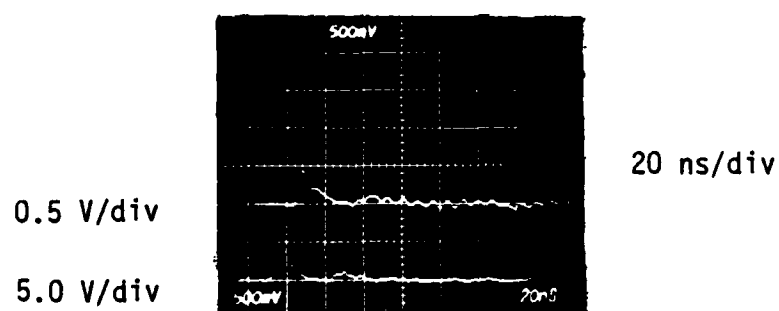
Fig. IV-5 shows a typical electron beam current signal having a peak current of about 18.8 kA and a risetime of 4 ns to 5 ns as measured by the Faraday cup. The risetime of the signal may be instrument limited by the approximate 160 MHz bandwidth of the Faraday cup. Although Fig. IV-5 represents a typical beam, electron beams with peak currents greater than 10 kA, some having peak currents as large as 35 kA, occurred only for about one out of ten discharges because of the nonreproducibility of the plasma focus discharge.

#### Electron Beam Guiding Field Results

Development of an electron beam guiding system was motivated by physical evidence which suggests that the beam does not always propagate parallel to the axis of the DPF. To demonstrate this, a 6.0-mm-thick aluminum witness plate was positioned at the base of a hollow DPF anode as shown in Fig. IV-6(a). The anode used in this experiment was developed for



(a)



(b)

Fig. IV-4. The bremsstrahlung x-ray dose rate produced by the electron beam was measured using the arrangement shown in (a) where PIN A and PIN B are PIN diodes which have intrinsic layer thicknesses of 20  $\mu\text{m}$  and 125  $\mu\text{m}$ , and  $e^{-1}$  transmissions of 40 keV and 300 keV, respectively. Typical results are shown in (b) for DPF operation with  $V_0 = 16$  kV and  $P_0 = 1.25$  torr.

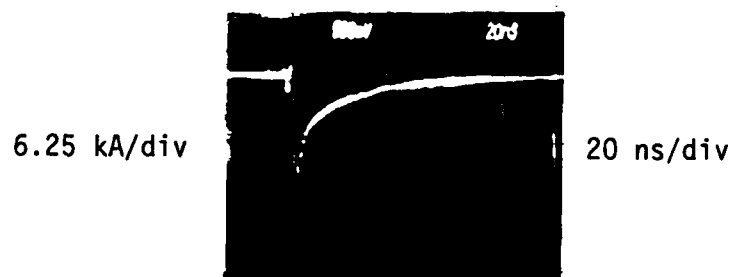
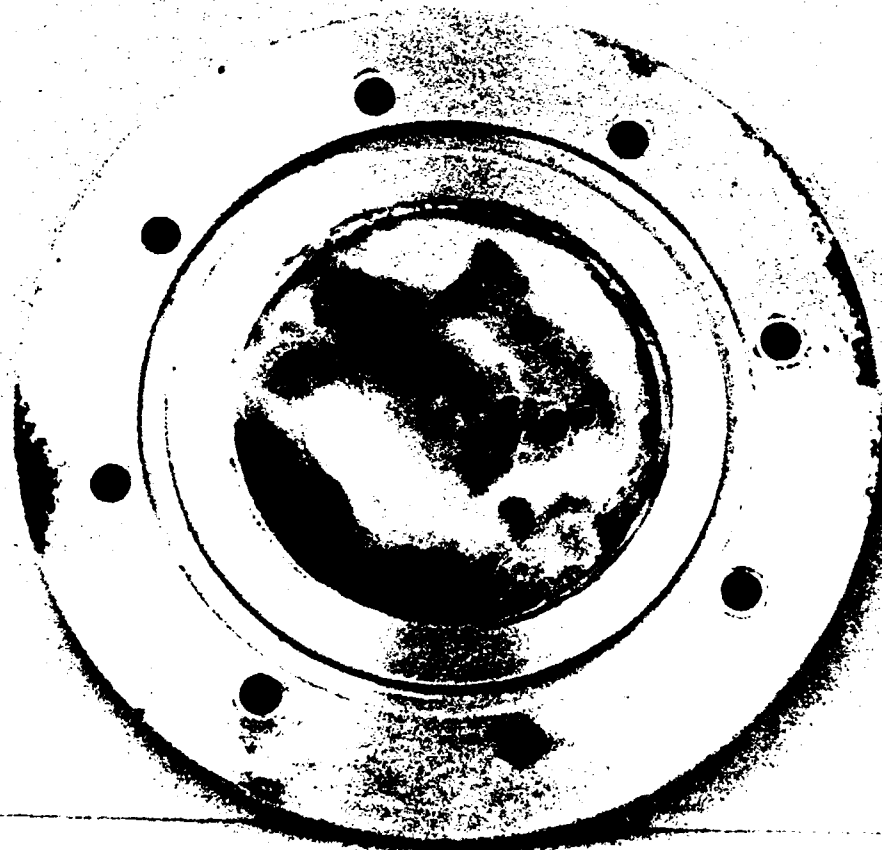
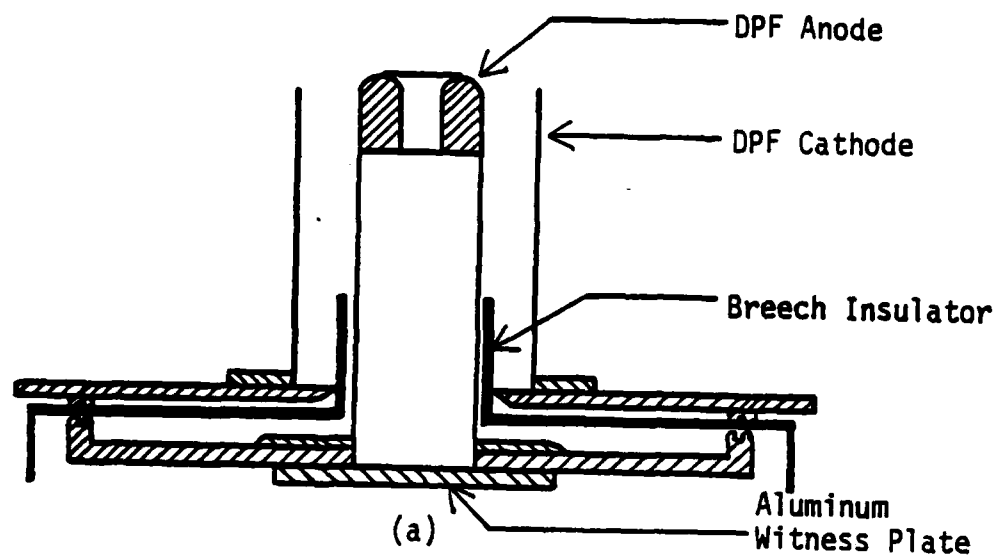


Fig. IV-5. Typical DPF electron beam current as measured by the Faraday Cup for DPF operation with  $V_0 = 16$  kV and  $P_0 = 1.25$  torr.





(b)

1 cm

Fig. IV-6. The experimental arrangement shown in (a) was used to illustrate the divergence of the DPF electron beam from the DPF axis. The resulting damage is shown in (b).

use with the beam guiding apparatus; however, the upper section of the guiding field solenoid was not included so that the angle at which a beam ejected through the anode aperture could propagate relative to the anode axis was limited by the diameter and length of the anode body rather than the smaller diameter and increased length of the guiding field solenoid (see Fig. III-5). Hence, assuming that the electron beam is produced on the DPF axis and flush with the anode surface, the maximum angle at which a beam can propagate relative to the axis without striking the inside surface of the anode body is about  $8.7^\circ$ .

With this experimental arrangement, the DPF was discharged 90 times at initial capacitor bank voltages and fill-gas pressures in the ranges of 11 kV to 15.5 kV and 2.0 torr to 3.0 torr, respectively. The resulting damage to the aluminum witness plate is shown in Fig. IV-6(b) in which the surface of the witness plate was lightly sanded in order to highlight localized damage sites. The position of most of the localized damage sites relative to the center of the witness plate strongly suggests electron beam propagation at significant angles relative to the DPF axis.

Initial tests on the guiding field solenoid showed that a negligible magnetic field was produced at rated coil current in the region of the DPF pinch. The measurement was performed without a plasma focus discharge using the  $\dot{B}$  probe and integrator described in Appendix A which has a maximum resolution of about  $10^{-3}$  T. When the plasma focus was discharged, other diagnostic results, which include Rogowski probe signals, image converter camera streak and framing photographs, and soft x-ray pinhole photographs, were apparently unaffected by energizing the guiding field solenoid. The performance of the beam guiding apparatus was subsequently evaluated using two independent experiments. The first experiment used

the Faraday cup to measure the electron beam current while the second experiment used two PIN diode x-ray detectors in the arrangement shown in Fig. IV-4(a).

The risetime and the basic shape of the Faraday cup signal were unaffected by the guiding field; however, the magnitude of the peak current was usually larger when the guiding field solenoid was energized. Thus, the performance of the beam guiding apparatus was evaluated by recording the peak current of the electron beam for many DPF discharges with, and without, the use of the guiding field and comparing the peak current distributions. The DPF was operated at a capacitor bank voltage of 16 kV and fill-gas pressure of 1.25 torr while the peak magnetic flux density produced by the guiding field solenoid was  $4.8 \times 10^{-2}$  T, corresponding to a coil current of 100 A. The DPF discharge was delayed 165  $\mu$ s relative to the guiding field discharge so that the magnetic field inside the guiding field solenoid would be near maximum at the pinch. The fill gas was renewed every 10 to 12 shots, and the guiding field was energized on alternate fills of gas.

The results of this experiment are presented in Fig. IV-7. The height of each histogram bar is proportional to the number of DPF discharges producing a peak electron beam current within the indicated interval and is expressed as a percentage of the total number of shots on the ordinate. The figure shows that the use of the guiding field reduces the probability that the DPF discharge will produce an electron beam with a peak current less than 15 kA while increasing the probability that the peak electron beam current will be greater than this value. In fact, a peak electron beam current greater than 10 kA occurs for two out of ten DPF discharges

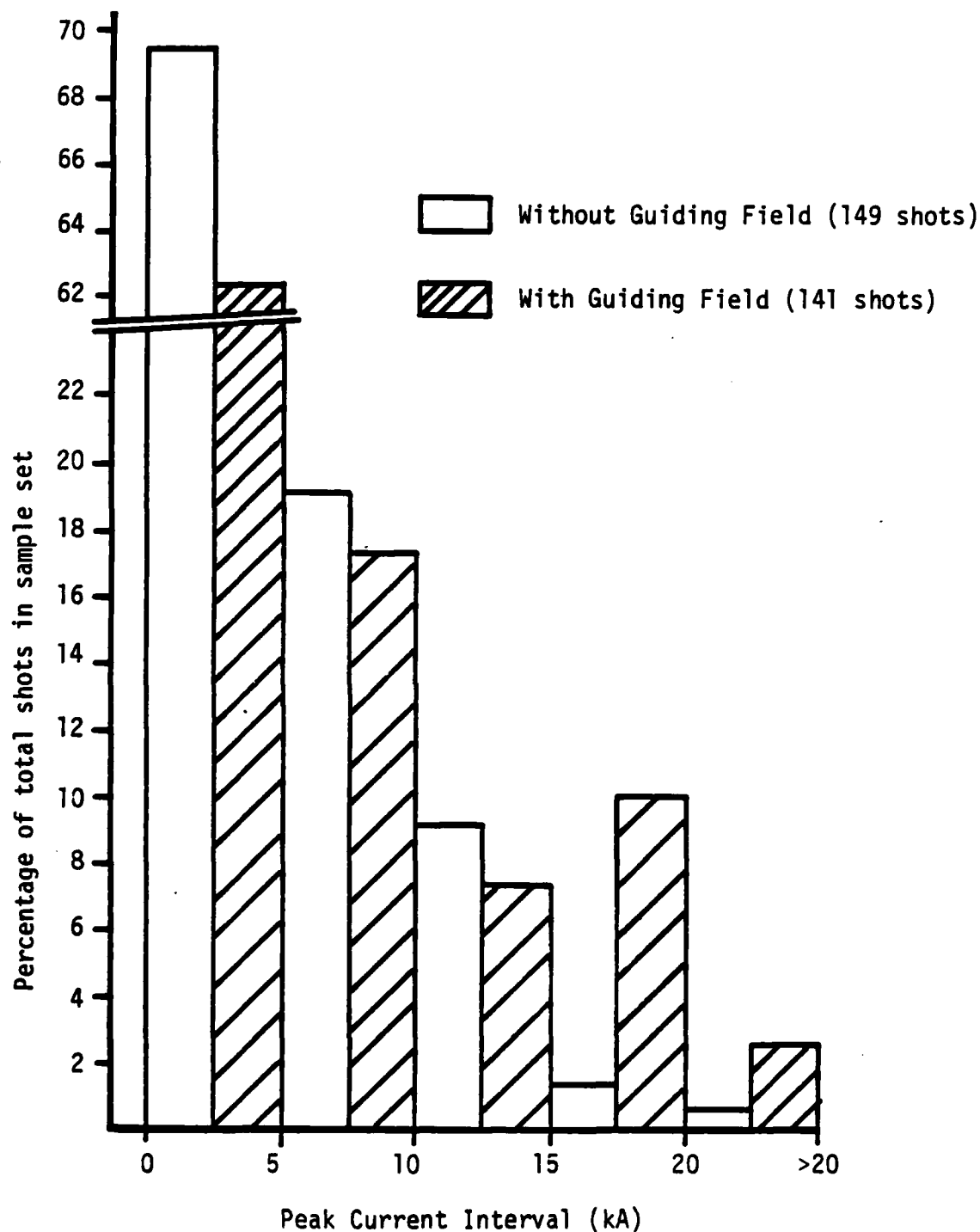


Fig. IV-7. Peak beam current results illustrating the performance of the beam guiding apparatus. The peak current intervals are such that the histogram analysis includes the lower limit but excludes the upper limit.

when the guiding field is used as opposed to one out of ten discharges when the guiding field is not used.

In the second experiment, the Faraday cup was replaced with the 3.2-mm-thick aluminum target and PIN diode arrangement shown in Fig. IV-4(a). The DPF was operated under the same conditions as in the Faraday cup experiment. As in the previous experiment, the guiding field had no apparent effect on the shape of the x-ray pulse, but the peak value of the signal was more likely to be larger when the guiding field was energized. The detector signals were recorded for a number of discharges, and the results of the experiment, shown in Fig. IV-8, seem to support the results obtained with the Faraday cup. The effect of the guiding field is not quite as evident in these data as in the Faraday cup data; nevertheless, there does seem to be an increase in the x-ray dose rate for both detectors when the guiding field solenoid is energized. These results imply that more electrons are impinging on the aluminum target and are consistent with an increase in peak beam current.

#### The Effect of the Auxiliary Electrode

As mentioned in Chapter I, one of the initial goals of this study was to investigate the apparent enhancement of the DPF electron beam by an auxiliary discharge as inferred from a relative increase in high-energy x rays (greater than 300 keV). In that study, the DPF discharge was observed to induce a current in the inductive energy storage circuit regardless of the magnitude of the auxiliary current. However, without the auxiliary discharge the introduction of the electrode seemed to have no apparent effect on the characteristics of the DPF since diagnostic results were comparable for operation of the DPF with or without the auxiliary electrode in the DPF chamber. These results, which were verified during

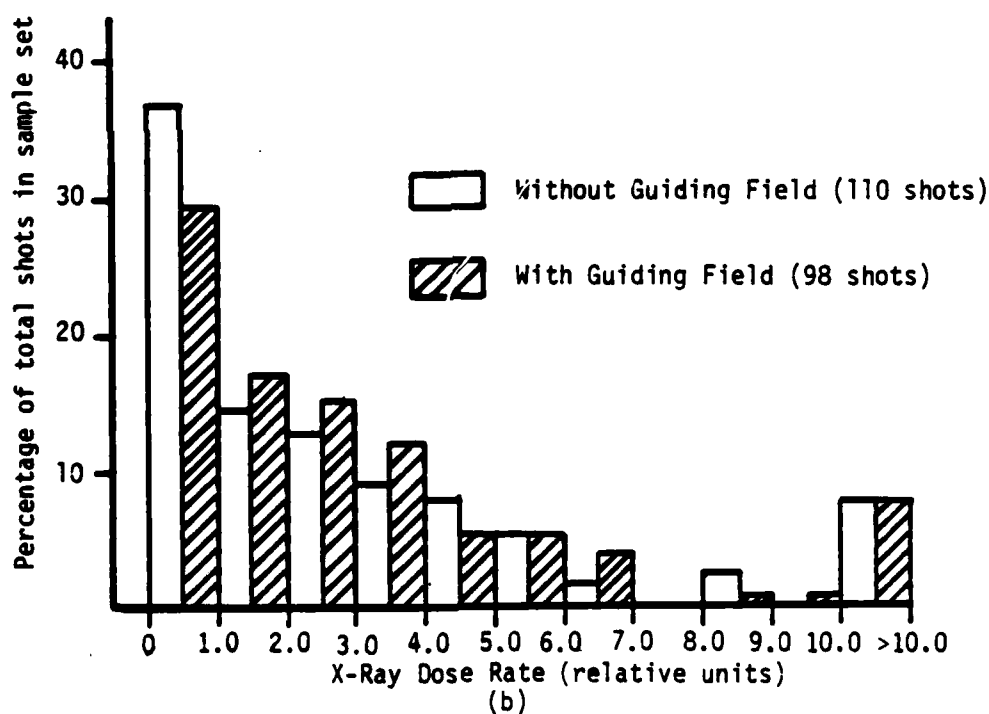
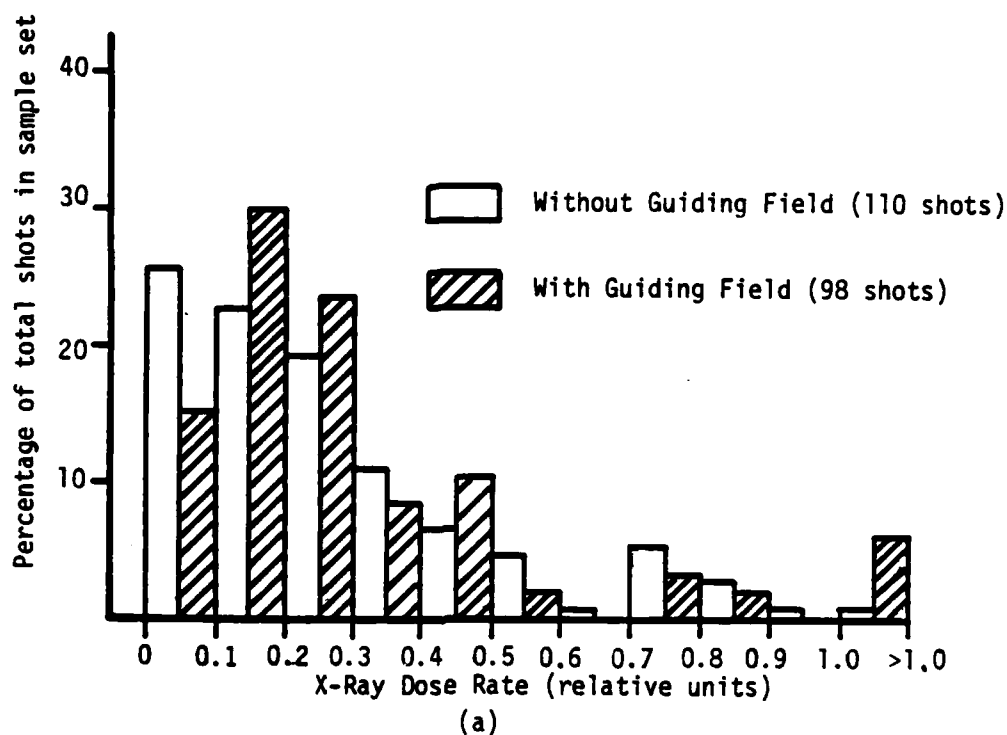


Fig. IV-8. X-ray dose-rate measurements illustrating the performance of the beam guiding apparatus. The results collected using (a) PIN A and (b) PIN B are expressed in relative units, and the dose-rate intervals are such that the histogram analysis includes the lower limit but excludes the upper limit.

the course of this investigation, included measurement of the DPF discharge current using a Rogowski probe, image converter streak and framing photographs of the collapsing current sheath, and soft x-ray pinhole photographs of the pinch.

Initial attempts to measure the electron beam current using the Faraday cup suggested that the presence of the auxiliary electrode, without an auxiliary current, has an adverse effect on the DPF electron beam production. On the average, this effect seemed to be inversely related to the separation between the DPF anode and the auxiliary electrode. Consequently, the emphasis of this investigation shifted to a study of this effect.

Using the experimental arrangement of Fig. III-10 with the load and load gap removed, the electron beam current was measured with eight different electrode separations over the range of 5.0 cm to 25.4 cm as well as with the electrode removed from the discharge chamber. Initial experiments were conducted with the auxiliary electrode connected to the inductive energy storage circuit. The DPF was operated at 16 kV and 1.25 torr with the fill gas renewed every 10 to 12 shots, and data was collected until at least 24 discharges were recorded for each auxiliary electrode position. Furthermore, the electron beam guiding apparatus with a maximum magnetic flux density of  $4.8 \times 10^{-2}$  T was used on each shot. In addition to the Faraday cup, a PIN diode mounted to the side of the DPF and isolated from the discharge chamber by a 1.6-mm-thick aluminum plate and 3.2 mm of lead shielding was used to measure the relative x-ray dose rate from the pinch region for energies greater than 300 keV.

Due to the nonreproducibility of the DPF discharge, the effect of the auxiliary electrode was evaluated by calculating an unweighted average of

the peak beam current for each of the eight auxiliary electrode positions, the results of which are presented in Fig. IV-9. Each point on the graph is normalized with respect to the 4.7 kA average value of the peak beam current calculated for the data collected when the auxiliary electrode was removed from the DPF chamber. The confidence intervals indicated for each point were calculated using the formula

$$P(\bar{X} - c\sigma/\sqrt{N} \leq \bar{X} \leq \bar{X} + c\sigma/\sqrt{N}) = 0.90 \quad (\text{IV-1})$$

where  $\bar{X}$  is the mean of a random variable described by a normal distribution,  $\sigma$  is the standard deviation,  $N$  is the number of samples in the set,  $c$  is a constant equal to 1.645, and 0.90 is the probability that the mean of an ensemble of sample points will fall in the indicated range [41]. The probability distribution which describes the data collected in these experiments is apparently exponential rather than normal, as is evident in the results presented in Fig. IV-7. However, the Central Limit Theorem [41] allows Eq. (IV-1) to be applied to any distribution provided that the size of the sample set is sufficiently large (e.g., greater than 20 samples).

The results of the x-ray dose-rate data were treated in the same way as the peak beam current data and show that, within experimental error, the x-ray dose rate remains relatively constant over the entire range of electrode separations.

From an experimental standpoint, three possible interactions were considered in attempting to explain this effect.

- (1) The auxiliary electrode may physically obstruct the motion of the converging current sheath prior to the formation of the pinch.



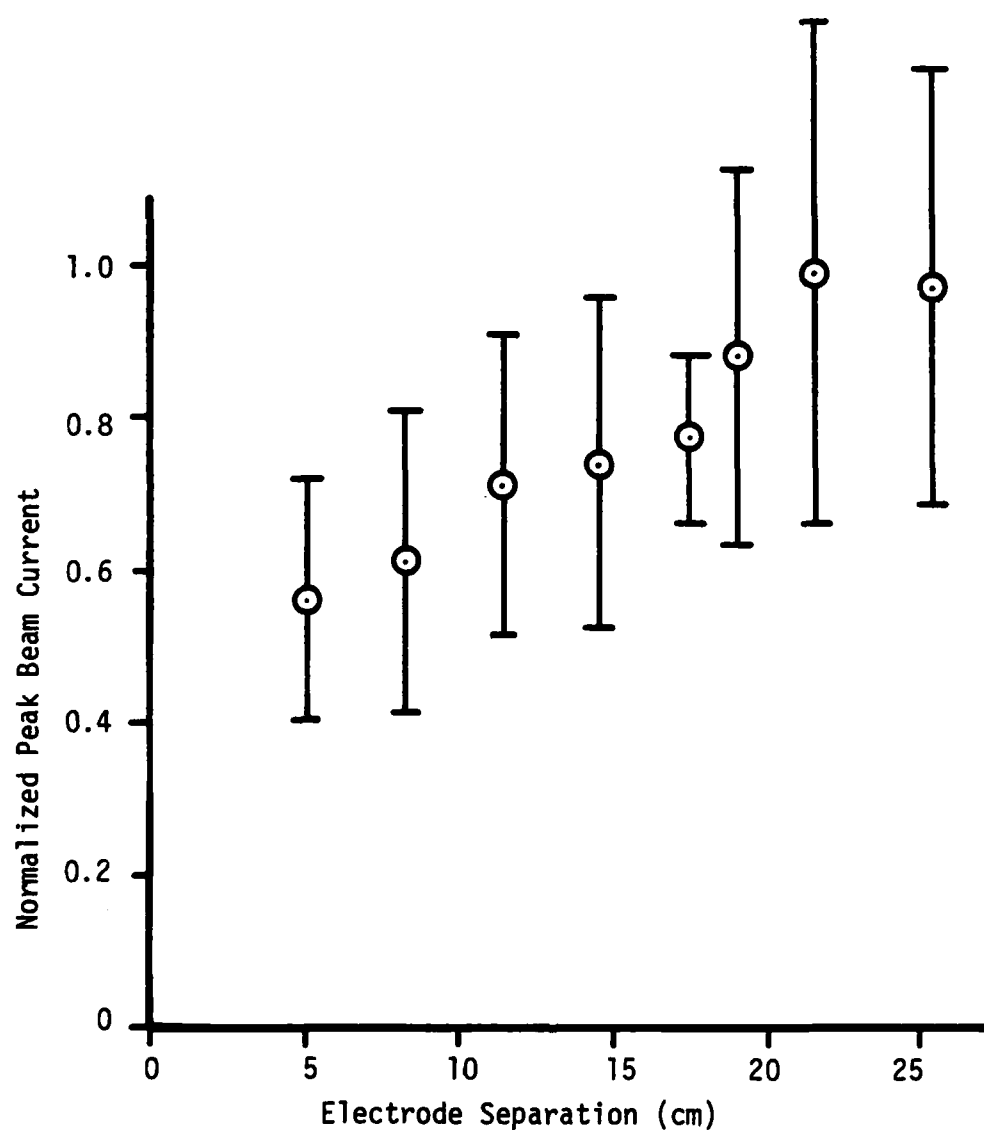


Fig. IV-9. The Faraday Cup results illustrating the effect of the auxiliary electrode when connected to the inductive energy storage circuit. The normalized confidence interval on the average peak beam current measured when the auxiliary electrode was not in the DPF chamber is  $\pm 0.24$ .

- (2) A portion of the DPF discharge current, and thus some of the stored energy, may be diverted from the DPF circuit by the inductive energy storage circuit.
- (3) The electric potential of the auxiliary electrode may interfere with the production or trajectory of the DPF electron beam.

The first of these interactions can be eliminated in view of the rather large interaction distances involved and a consideration of image converter camera framing photographs (Fig. IV-2(b)) which show that the top of the current sheath is no more than about 2.5 cm above the top of the DPF anode at the time of the pinch. The second and third possible interactions required additional experimental investigation which is described subsequently.

Two current transformers (CT-A and CT-B in Fig. III-10) were used to measure the DPF discharge current diverted into the inductive energy storage circuit. For DPF operation at 16 kV and 1.25 torr, current was observed at several auxiliary electrode positions using CT-A while comparatively less current was measured using CT-B. This suggests that the 42- $\mu$ H energy storage inductor electrically isolates the DPF from the remainder of the inductive energy storage circuit and that the current measured by CT-A is shunted to ground by the capacitance of the high-voltage, coaxial feeder cable. A typical current measured by CT-A is shown in Fig. IV-10. The bottom trace of Fig. IV-10 is a time expansion of the interval indicated on the top trace. The electrode separation for this shot was 14.6 cm; however, the current was found to be independent of the distance between the electrodes. The strongest interaction, which has a peak current of about 600 A with a subsequent oscillatory current having a period of about 400 ns, correlates well with the x-ray pulse emitted by the

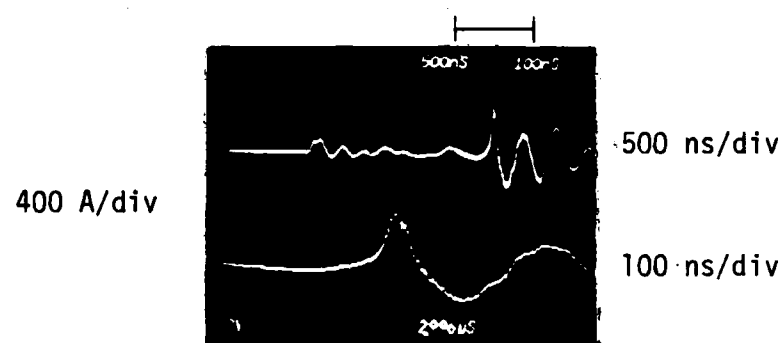


Fig. IV-10. The DPF current diverted to the inductive energy storage circuit as measured by CT-A. The upper trace shows the interaction over the entire DPF discharge interval and the lower trace is a time expansion of the upper trace over the interval shown. The signal polarity is such that positive current flow is opposite to the reference arrow shown in Fig. III-10.

pinch. The peak current measured by CT-A varied from shot-to-shot over the range of 480 A to 680 A.

If the high-voltage feeder cable is modeled as a capacitor which is initially uncharged, the auxiliary electrode is initially at the same potential as the DPF anode. Thus, in an attempt to determine the effect of the auxiliary electrode's electric potential on the DPF electron beam, the auxiliary electrode was disconnected from the high-voltage feeder cable and reconnected to the DPF discharge chamber which is at the same potential as the DPF cathode. This experiment was conducted in the same manner as the experiment which produced the results presented in Fig. IV-9. The results of this experiment are presented in Fig. IV-11 and show that the normalized average of the peak beam current approaches unity for a much smaller electrode separation. Furthermore, the x-ray dose-rate data were similar to the results recorded when the auxiliary electrode was at the anode potential. Also, the current transformer CT-A, which was located so as to measure currents coupled through the auxiliary electrode to the DPF vacuum chamber, also showed no apparent interaction above background noise.

Considering the results of these experiments, it has been shown that, on the average, the peak beam current is a function of the distance between the auxiliary electrode and the DPF anode. It also seems plausible that current is diverted from the DPF circuit into the inductive energy storage circuit with the auxiliary electrode installed. These results have also been shown to be a function of whether the electrode is effectively connected to the DPF anode or cathode. A physical interpretation of these processes are considered in Chapter V (Theoretical Considerations) and an appropriate model is proposed.

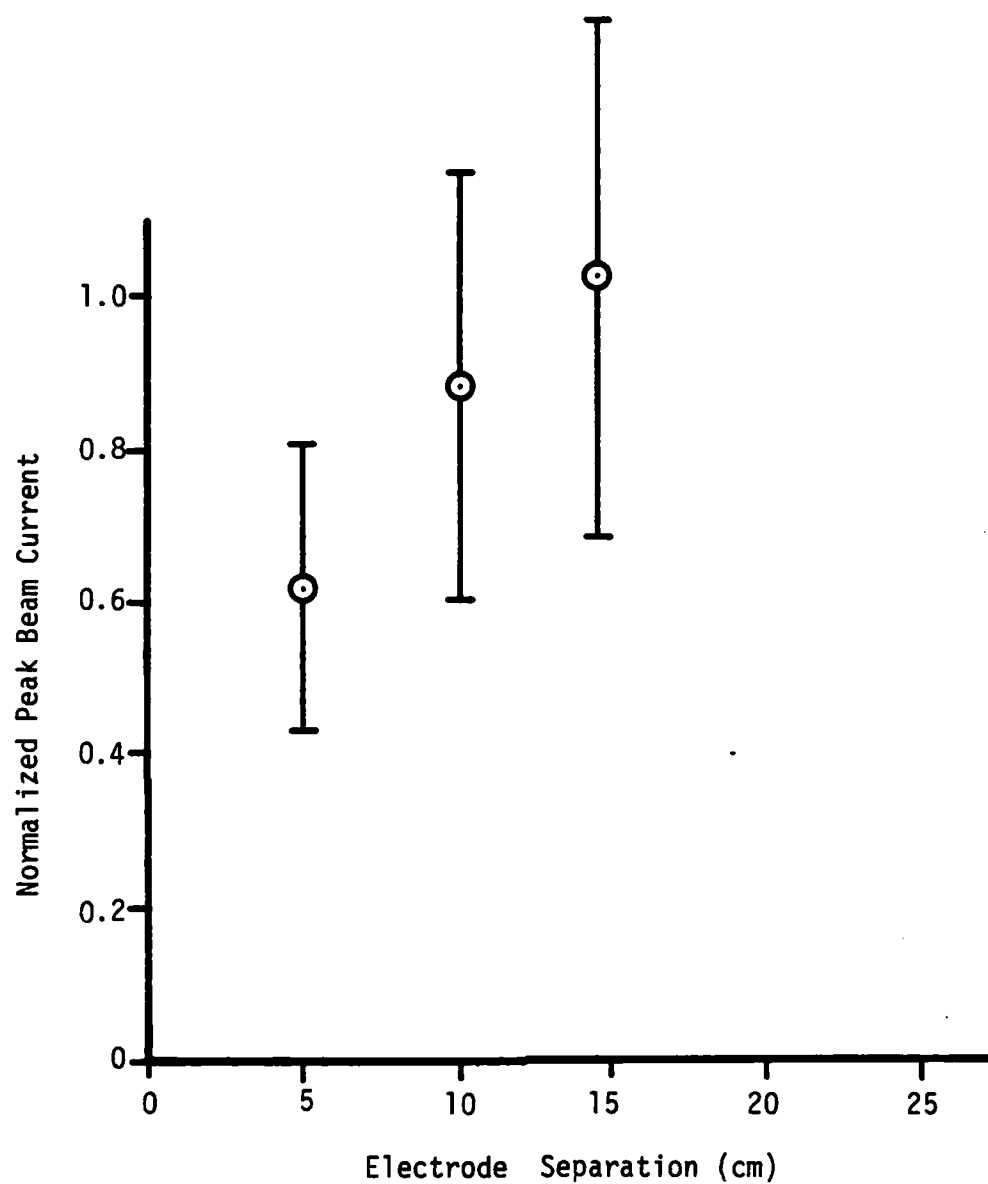


Fig. IV-11. Faraday Cup results illustrating the effect of the auxiliary electrode when at the potential of the DPF cathode. The normalized confidence interval on the average peak beam current measured when the auxiliary electrode was not in the DPF chamber is  $\pm 0.24$ .

## Chapter V

### THEORETICAL CONSIDERATIONS

Theoretical considerations pertaining to concepts which motivated certain aspects of the investigation and an analysis of the experimental results are presented in this chapter. Topics considered include a brief outline of electron beam propagation theory, a theoretical basis for the use of a magnetic beam guiding field, and a detailed analysis of the experimental results collected with the auxiliary electrode in the DPF vacuum chamber. The MKS system of units are used throughout the chapter.

#### Electron Beam Propagation

An electron beam can be loosely regarded as a collection of energetic electrons with similarly directed velocity vectors. As such, the electron beam constitutes an electric current and must satisfy Maxwell's equations. In particular, Ampere's Law requires that

$$\nabla \times \vec{H} = \vec{J} + \frac{\partial \vec{D}}{\partial t} \quad (V-1)$$

where  $\vec{H}$  is the magnetic field intensity,  $\vec{J}$  is the current density, and  $\vec{D}$  is the electric flux density. If a generalized current density is defined as

$$\vec{J}_T = \vec{J} + \frac{\partial \vec{D}}{\partial t}, \quad (V-2)$$

the divergence of Eq. (V-1) yields

$$\nabla \cdot \vec{J}_T = 0 \quad (V-3)$$

where the vector identity,

$$\nabla \cdot (\nabla \times \vec{V}) = 0 \quad (V-4)$$

has been used for an arbitrary vector  $\vec{V}$ . Equation (V-3) requires that the current in any electromagnetic system must be solenoidal (i.e., the current paths in the system must close on themselves). Therefore, the current carried in a propagating electron beam must be accompanied by a return current which may be manifested as charge transport in a plasma through which the beam may propagate, a current induced in a nearby conducting structure, or a displacement current.

In addition to the necessity for a return current, an electron beam experiences radially outward forces caused by the Coulomb repulsion between electrons in the beam and radially inward forces caused by the azimuthal magnetic field generated by the beam current. Although these forces tend to cancel each other somewhat, one of the forces usually dominates the other in many practical situations if sufficient charge or current neutralization is not present .

To illustrate charge neutralization, the propagation of a cylindrical electron beam with density  $n_e$  is considered as it moves through a background of stationary ions with density  $n_i$ . The radial component of the Lorentz force on a single electron in the beam is

$$F_r = -e(E_r - vB_\theta) \quad (V-5)$$

where  $E_r$  is the radial electric field,  $B_\theta$  is the azimuthal magnetic flux density,  $e$  is the electronic charge,  $v$  is the velocity of the electron perpendicular to the azimuthal magnetic field, and the radially outward direction is positive by convention. The electric field and magnetic flux density can be derived from Gauss' Law and Ampere's Law, respectively; the results of which are

$$E_r = \frac{-e}{\epsilon_0} r \int n_e (1 - f_e) r dr \quad (V-6)$$

$$B_\theta = \frac{-\mu_0 ev}{r} \int n_e r dr \quad (V-7)$$

where  $\epsilon_0$  is the permittivity of free space,  $\mu_0$  is the permeability of free space, and  $f_e = n_e/n_i$  is the fractional electron space charge neutralization. Substituting Eqs. (V-6) and (V-7) into Eq. (V-5) gives the radial force as

$$F_r = \frac{e^2}{\epsilon_0} r \int n_e (1 - \beta^2 - f_e) r dr \quad (V-8)$$

where  $\beta$  is the ratio of the electron velocity to the speed of light. Equation (V-8) shows that if

$$f_e < 1 - \beta^2 \quad (V-9)$$

(i.e., minimal charge neutralization is present), the beam will radially expand. Furthermore, it can be shown that if the electrostatic potential due to the beam space charge, which is a function of  $f_e$ , is greater than the kinetic energy of the beam, a deep potential well, or virtual cathode, can form which partially reflects the injected beam current so that total transmission of the beam is not possible [42].



Current neutralization can be illustrated by considering the beam of the previous example propagating through a region in which the beam is completely charge neutralized ( $f_e = 1$ ). In early work, Alfvén [43] considered a charged particle beam similar to the beam previously described and derived an upper limit for the current which can be carried by the beam. This limit may be expressed as

$$I_A = 17,000 \beta \gamma \quad (V-10)$$

where  $I_A$  is in amperes and  $\gamma = (1 - \beta^2)^{-1/2}$ . Exceeding this limit produces an azimuthal magnetic field of sufficient magnitude so as to reverse the direction of the electron's net motion at the outer edge of the beam. If the beam current is partially neutralized by counterstreaming electrons in the beam channel, such as may occur in a highly conductive plasma, the azimuthal magnetic field will also be neutralized and the limiting current can be qualitatively expressed as

$$I_A' = \frac{I_A}{1 - f_m} \quad (V-11)$$

where  $f_m$  is the fractional current neutralization [44]. According to Eq. (V-11), arbitrarily large beam currents are possible with sufficient current neutralization; however, beam propagation is then limited by instabilities which develop from the interaction of the beam electrons and the counterstreaming electrons [42].

In many practical situations, a propagating electron beam is only partially neutralized with respect to charge and current. However, it can be shown that stable propagation can occur if the radial forces are exactly balanced [42]. This equilibrium condition is given by

$$f_e = \gamma^{-2} + \beta^2 f_m \quad (V-12)$$

where it is assumed that the electron beam has no angular momentum. If  $f_e$  exceeds the equilibrium value, the radially inward magnetic forces will exceed the Coulomb repulsion forces and the beam will constrict, or pinch. For the opposite case, Coulomb repulsion will dominate and the beam will radially expand.

The conditions described above illustrate the concepts of charge and current neutralization in an electron beam; however, the situations described are somewhat idealized and are not applicable in many cases. More complete treatments of these propagation phenomena, which are beyond the scope of this report, are available in the literature [42,44-46].

The propagation of an electron beam injected into a neutral gas, which is assumed to be the primary mode of propagation in the DPF drift tube, is very difficult to describe quantitatively because of a dependence on the ionization properties of the gas. For efficient transport of the beam, there must be sufficient ionization of the background gas so as to provide significant charge and current neutralization, particularly if the beam current exceeds the Alfvén limit. The ionization rate of the neutral gas and the neutralization properties of the subsequently ionized gas are sensitive functions of the gas pressure [42,45,46]. At low pressure (typically less than 0.5 torr), the gas density is so low that not enough ions can be produced to provide charge neutralization; alternatively, at high pressure (typically greater than 10.0 torr), the gas density is so high that, even though charge neutralization is achieved, the collision rate between the plasma particles is high enough to keep the plasma temperature

relatively low so that the plasma conductivity is generally too low to provide adequate current neutralization. However, an intermediate pressure range (typically between 1.0 torr and 10.0 torr) exists in which sufficient charge and current neutralization can occur for efficient beam propagation. The optimum pressure for beam transmission varies somewhat with the gas species but usually falls within this range.

The DPF drift tube was typically operated in the intermediate pressure range (usually about 1.25 torr); however, it is not known if the drift tube was operated at the optimum pressure since the formation of the plasma focus pinch (and hence, the production of the electron beam) is also a sensitive function of pressure. Nevertheless, it is assumed that the drift tube was operated close to the optimum pressure since the maximum peak beam currents observed were often well in excess of the Alfvén limit. For example, given that the mean energy of the beam electrons is about 150 keV, the Alfvén limiting current can be calculated from Eq. (V-10) to be approximately 14 kA. The maximum peak current observed was about 2.5 times greater than the Alfvén limit, thus suggesting that significant charge and current neutralization was taking place. In addition to ionization by the electron beam, it also seems reasonable to assume that some preionization of the drift tube gas may have been produced by the intense ultraviolet and x-ray emission from the DPF pinch prior to injection of the electron beam into the drift space.

#### The Guiding Field Concept

The use of an axial magnetic field to guide the DPF electron beam was motivated by the experimental results shown in Fig. IV-6(b). To illustrate how a magnetic field can be useful in this respect, the motion of a single

electron propagating in a static magnetic field is considered. The Lorentz force law in this case is

$$\frac{d}{dt}(m\vec{v}) = -e(\vec{v} \times \vec{B}) \quad (V-13)$$

where  $\vec{v}$  is the velocity of the electron,  $\vec{B}$  is the magnetic flux density of the static magnetic field,  $m = \gamma m_0$  is the effective mass of the electron, and  $m_0$  is the electron's rest mass. If it is assumed that the magnetic field is in the  $z$  direction and the magnitude of the velocity components perpendicular to the magnetic field are much less than the parallel velocity component, the perpendicular components of Eq. (V-13) can be written as

$$\begin{aligned} \ddot{v}_x + \left(\frac{\omega_c}{\gamma}\right)^2 v_x &= 0 \\ \ddot{v}_y + \left(\frac{\omega_c}{\gamma}\right)^2 v_y &= 0 \end{aligned} \quad (V-14)$$

where the cyclotron frequency,  $\omega_c$ , is defined as

$$\omega_c = \frac{e|\vec{B}|}{m_0}, \quad (V-15)$$

and the dot indicates differentiation with respect to time. Analysis of the electron orbit described by Eq. (V-13) for the particular case being considered shows that the electron follows a helical path with a characteristic radius, called the Larmor radius, which is defined by

$$r_L = \frac{\gamma v_{\perp}}{\omega_c} = \frac{m v_{\perp}}{e|\vec{B}|} \quad (V-16)$$

where  $v_{\perp}$  is the magnitude of the velocity perpendicular to the axis. Equation (V-16) shows that an electron can be forced to travel essentially parallel to the magnetic field lines provided that the magnetic flux density is sufficiently large.

In addition to guiding the beam electrons along the magnetic field lines, the magnetic guiding field exerts a radial restoring force which counteracts radial expansion due to Coulomb repulsion and radial constriction due to the azimuthal magnetic field. To illustrate this effect, the motion of a single electron at the edge of a cylindrically symmetric electron beam is considered where the beam is oriented along the  $z$  axis and has radius  $r$ . If it is assumed that the velocity components perpendicular to the external magnetic field, which is oriented parallel to the  $z$  axis, are much smaller than the parallel component, it can be shown that the radial component of the electron's motion is described by

$$\ddot{r} + \left(\frac{\omega_c}{2\gamma}\right)^2 r = \frac{-e}{\gamma m_0} (E_r - v_z B_{\theta}) + \left(\frac{P_{\theta}}{\gamma m_0}\right)^2 \frac{1}{r^3} \quad (V-17)$$

where the position of the electron is  $r$ ,  $P_{\theta}$  is the canonical angular momentum, and  $v_z$  is the electron velocity parallel to the  $z$  axis [42]. Furthermore, if the density of the beam is assumed constant over the radius, then the radial electric field and azimuthal magnetic flux density can be derived from Eqs. (V-6) and (V-7) to be

$$E_r = \frac{-en_e (1 - f_e)}{2\epsilon_0} r \quad (V-18)$$

$$B_{\theta} = \frac{-\mu_0 n_e e v_z (1 - f_m)}{2} r \quad (V-19)$$

where terms have been included to account for partial neutralization.

An expression for the equilibrium radius ( $\ddot{r} = 0$ ),  $r_0$ , can be found by substituting Eqs. (V-18) and (V-19) into Eq. (V-17) to give

$$r_0^2 = \frac{2P_\theta}{m_0} \left[ \omega_c^2 - 2\gamma\omega_p^2 [(1 - f_e) - \beta^2(1 - f_m)] \right]^{-1/2} \quad (V-20)$$

where  $\omega_p^2 = n_e e^2 / (m_0 \epsilon_0)$  is the plasma frequency of the beam electrons.

Thus, equilibrium can only occur if

$$\omega_c^2 \geq 2\gamma\omega_p^2 [(1 - f_e) - \beta^2(1 - f_m)]. \quad (V-21)$$

Equation (V-21) relates the external magnetic field to the degree of charge and current neutralization of the beam. The fractional neutralization factors,  $f_e$  and  $f_m$ , are restricted to values which keep the right-hand side of the inequality positive; but, even for the simple conditions described, the inequality shows that an axial magnetic field can be used to stabilize the radial forces in a propagating electron beam. Furthermore, the inequality shows that the magnitude of magnetic flux density required for equilibrium decreases as the amount of fractional neutralization increases, as is expected.

#### Analysis of the Auxiliary Electrode Results

The DPF pinch is a complex, and not very well understood, physical phenomenon which is acutely sensitive to operating conditions. As shown by the experimental results, the mere presence of a third electrode in the DPF chamber is enough, on the average, to alter the beam producing characteristics of the device. Unfortunately, much more sophisticated diagnostic equipment and techniques than were available for this investigation are needed to conclusively determine the role of the auxiliary electrode in the

observed effect on the pinch; however, several observations can be made on the diagnostic results reported in Chapter IV.

It was found that both hard x-ray (greater than 300 keV) emission from the pinch and the DPF current waveform were unaffected by the auxiliary electrode regardless of the electrode's initial potential or position. This seems to suggest that the particle accelerating mechanisms of the pinch are not affected by the presence of the third electrode; however, since the transmitted beam is reduced, the electron beam is apparently being deflected away from the DPF axis to such a degree that the beam guiding apparatus is no longer effective. If the beam was redirected to the extent that it impinged on the top surface of the DPF anode, the average x-ray dose rate would be expected to be larger than the average dose rate measured when the auxiliary electrode was removed from the DPF chamber. However, if the beam was redirected only to the extent that it impinged on the inside of the anode aperture, out of the field of view of the x-ray detector, the observed results seem reasonable.

At first glance, the initial potential of the auxiliary electrode appears to have some bearing on the average electron beam production of the DPF as can be inferred from a comparison of Figs. IV-9 and IV-11. In fact, early attempts to map the electric fields for an arbitrary potential between the DPF electrodes in vacuum showed a surprising correlation between the perturbation of the field profiles caused by the potential of the auxiliary electrode and the results presented in Figs. IV-9 and IV-11. That is to say, the electric field profiles in vacuum appeared much more perturbed when the auxiliary electrode was initially at the anode potential (i.e., connected to the coaxial feeder cable). However, just prior to

the formation of the electron beam, the potential between the DPF electrodes is near minimum (approximately zero) since the discharge current is near maximum. Since the electric fields depend on the potential gradient, the development of fields sufficient in magnitude and spatial extent to deflect the electron beam is also at a minimum. Furthermore, the dense plasma would have a tendency to shield itself from any external electric fields. Therefore, it seems unlikely that the electric field perturbations produced by the potential of the auxiliary electrode with respect to the DPF electrodes is sufficient to significantly influence the trajectory of the electron beam.

The final group of experimental results to be considered is the data pertaining to the DPF current diverted by the auxiliary electrode. The waveform presented in Fig. IV-10 shows that the magnitude of the current diverted through the auxiliary electrode when connected to the coaxial feeder cable is several orders of magnitude smaller than the DPF current in the pinch. Consequently, the current measured with the current transformer in the external circuit is most likely not responsible for the observed effect on the electron beam; however, the observed current may be symptomatic of the actual cause.

A model based on these experimental results is proposed as an explanation for the observed effect on the electron beam. A magnetic field component transverse to the DPF anode and in the vicinity of the anode aperture would cause the aforementioned deflection of the electron beam. This magnetic field component could be produced by an azimuthally asymmetric, closed current path which includes the DPF electrodes, vacuum chamber, and auxiliary electrode as shown in Fig. V-1 by the dotted line. The secondary current is initially supplied by the DPF capacitor bank but



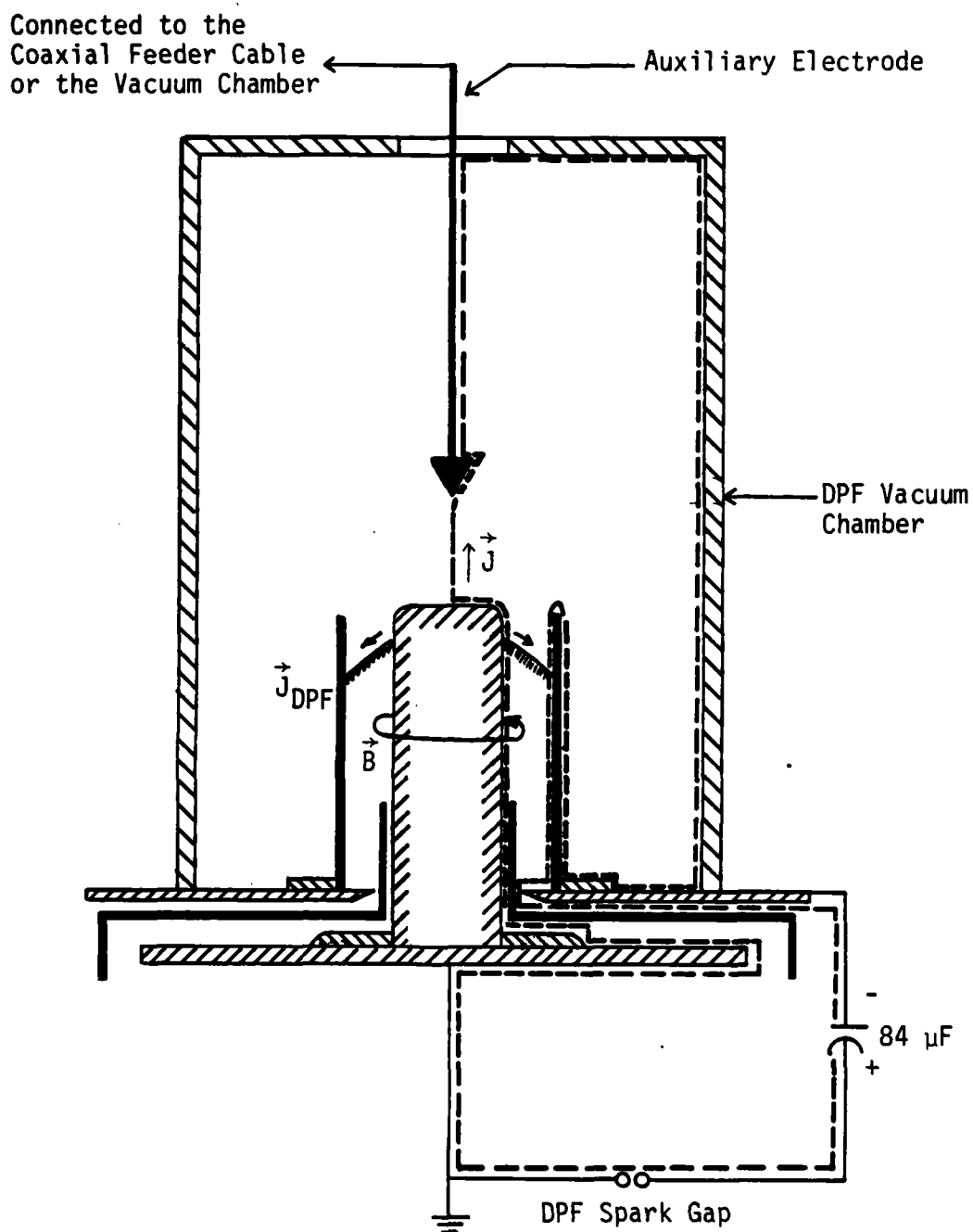


Fig. V-1. A transverse magnetic field in the region of the anode aperture at the time of beam formation can be produced by a secondary current density,  $\vec{J}$ . A possible closed path for the secondary current is shown by the dotted line.

may also have a magnetically induced component as the DPF current reaches a maximum. The inductive component is present because the secondary current loop contains all of the magnetic flux produced by the main DPF current. Also, the inductive component is in such a direction so as to satisfy Lenz's law [47] and as such, opposes the current which is supplied by the DPF capacitor bank. The net result is a current which is sufficiently strong to magnetically deflect the electron beam but not adversely affect the development of the pinch. This secondary current, which is much less in magnitude than the DPF current, apparently does not produce enough luminosity to be detectable on image converter photographs.

The DPF current diverted through the auxiliary electrode (Fig. IV-10), which also resembles the impulse response of an underdamped, series RLC network, can easily be explained in terms of the proposed model. To do so, the circuit in Fig. V-1 is modeled as the lumped-parameter circuit shown in Fig. V-2(a). The DPF discharge circuit is modeled as an ideal current source and a small inductance,  $L_{DPF}$ . The portion of the secondary current path external to the DPF discharge circuit is modeled as the sum of two inductances,  $L_1$  and  $L_2$ ; and, for the sake of simplicity, the inductive coupling between the secondary current and the DPF current is temporarily ignored. The coaxial feeder cable's connection to the auxiliary electrode and the DPF anode is modeled as an equivalent inductance,  $L$ , which is assumed to be much larger than any other inductance in the circuit. Lastly, the feeder cable is modeled by an equivalent capacitance,  $C$ .

To a first approximation, the DPF current and its derivative around the time of the pinch can be modeled by the piecewise-continuous, linear waveforms shown in Fig. V-2(b) and (c), respectively. Assuming that  $L_{DPF}$

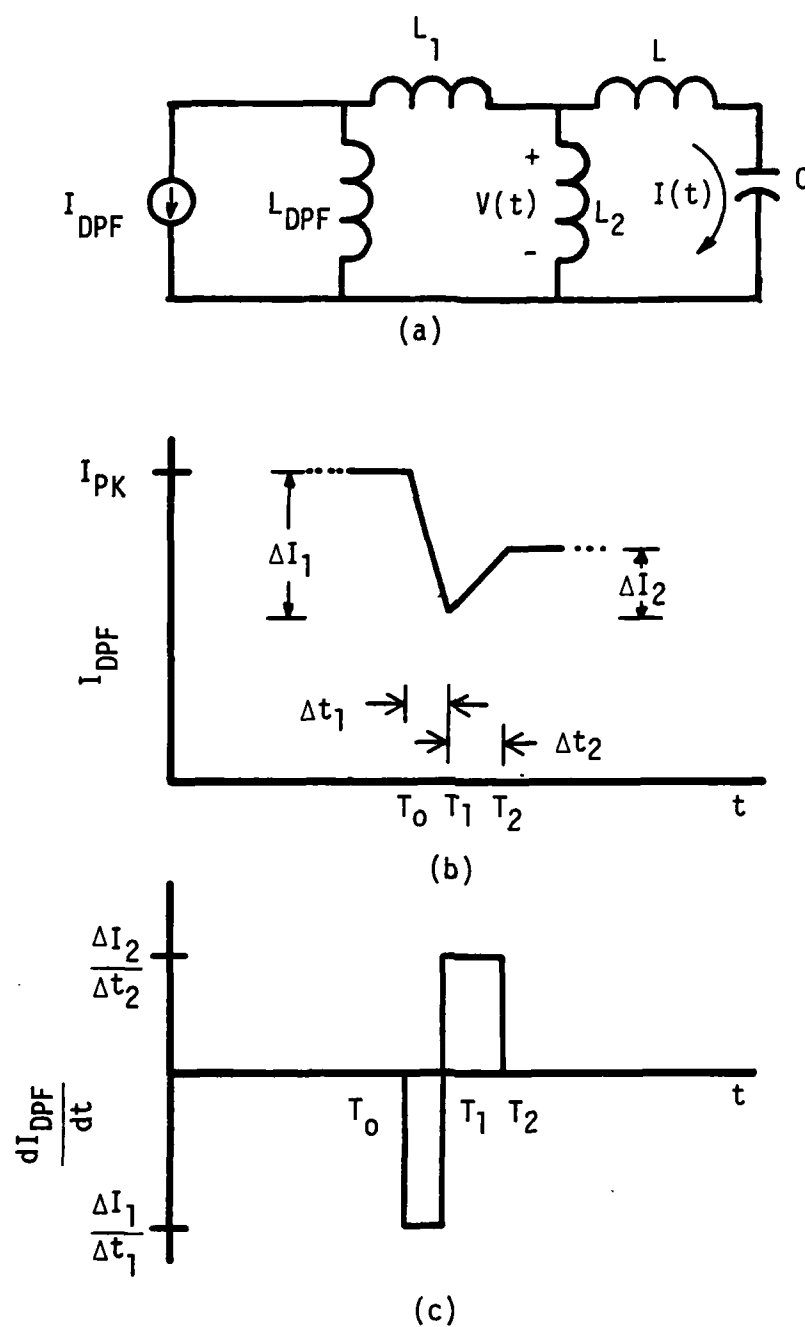


Fig. V-2. The interaction which produces the current measured by CT-A is modeled by the circuit shown in (a). The DPF current at the time of the pinch is modeled by (b) a piecewise-linear impulse-type function which has (c) a piecewise-continuous derivative.

is much smaller than the sum of  $L_1$  and  $L_2$ , the voltage  $V(t)$  across the inductor  $L_2$  can be written as

$$V(t) = k [-V_1 u(t - T_0) + (V_1 + V_2) u(t - T_1) - V_2 u(t - T_2)] \quad (V-22)$$

where

$$V_1 \approx L_{DPF} |\Delta I_1 / \Delta t_1|, \quad (V-23)$$

$$V_2 \approx L_{DPF} |\Delta I_2 / \Delta t_2|,$$

$u(t)$  is the unit step function,  $k$  is a constant which accounts for the relative magnitude of  $L_1$  and  $L_2$  as well as the previously ignored inductive coupling, and all other quantities are defined in Fig. V-2. The secondary current,  $I(t)$ , is easily computed using Laplace transform methods to be

$$I(t) = -k \sqrt{\frac{C}{L}} \left[ V_1 \sin\left(\frac{t - T_0}{\sqrt{LC}}\right) u(t - T_0) - (V_1 + V_2) \sin\left(\frac{t - T_1}{\sqrt{LC}}\right) u(t - T_1) + V_2 \sin\left(\frac{t - T_2}{\sqrt{LC}}\right) u(t - T_2) \right]. \quad (V-24)$$

Given that the capacitance per unit length of the coaxial feeder cable is 247.7 pF/m and that the cable length is 5.46 m, the equivalent capacitance,  $C$ , is calculated to be 1.35 nF. The inductance of the feeder cable connection can be estimated by assuming that the connection geometry is roughly rectangular and that the radius of the conductor forming the rectangular loop is essentially constant; thus, the inductance can be calculated using

$$L = 2 \times 10^{-7} \ell \left[ \ln\left(\frac{2\ell}{\rho}\right) - \alpha \right] \quad (V-25)$$

where  $L$  is in henries,  $\ell$  is the perimeter of the loop,  $\rho$  is the radius of the conductor, and  $\alpha$  is a constant which depends on the ratio of the lengths of the rectangle's sides [48]. The configuration is approximately a 61.0 cm by 122.0 cm rectangular loop with a mean conductor radius of 0.48 cm;  $\alpha$  is found from Ref. [48] to be 2.962. Thus the equivalent inductance,  $L$ , is calculated to be 3.2  $\mu\text{H}$ .

The current calculated with Eq. (V-24) is plotted in Fig. V-3 using the estimated values of the external circuit parameters and assuming that  $L_{\text{DPF}}$  is the 33 nH inductance mentioned in Chapter III. Furthermore, the parameters used to describe the DPF current waveform, which are listed in the figure, were selected as typical. For an appropriate choice of the constant  $k$ , the results presented in Fig. V-3 compare very favorably with the experimental results presented in Fig. IV-10, particularly with respect to polarity and frequency of oscillation. It is noteworthy to mention that the ratio of the first two peaks depends on the presence of the current "dip" shown in Fig. V-2(b). For example, the ratio of the first to the second peak in Fig. V-3 is about 1.61, which corresponds well with the experimentally observed ratio of 1.55 (Fig. IV-10); however, if  $\Delta I_2$  is zero, the ratio of the peaks of the resulting waveform is approximately unity. Also, the experimentally observed shot-to-shot variation in the first peak of the waveform qualitatively corresponds to variations in the parameters specified in Fig. V-2(b) as well as the value of  $k$ .

When the auxiliary electrode is connected to the DPF cathode, the potential difference between the auxiliary electrode and the DPF anode is the capacitor bank voltage. Since the chamber pressure is such that the DPF is probably operated near the Paschen breakdown minimum [49], breakdown can occur easily between the auxiliary electrode and the DPF anode

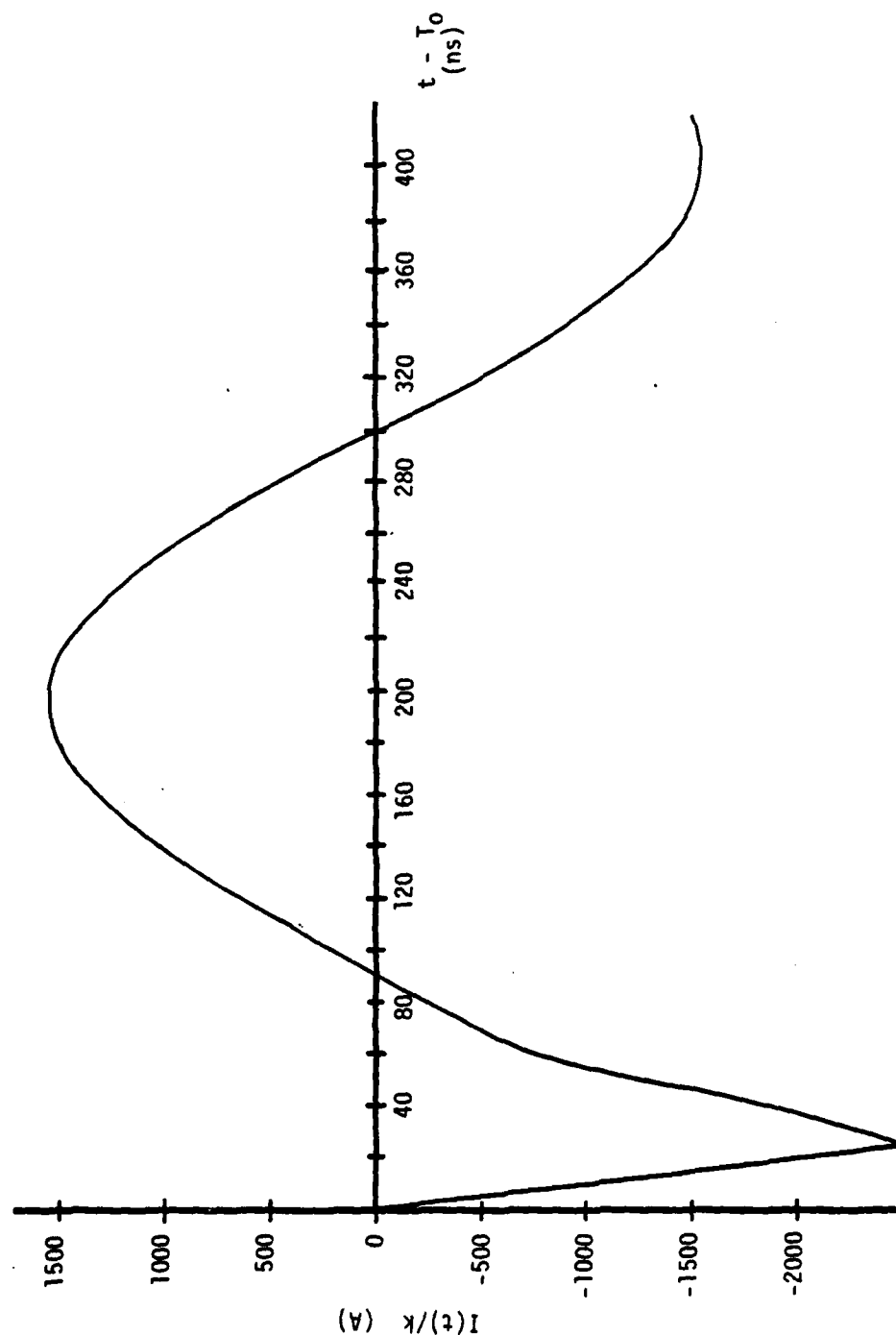


Fig. V-3. Response of the circuit shown in Fig. V-2(a) to the excitation presented in Fig. V-2(b) for  $L = 3.2 \mu\text{H}$ ,  $C = 1.35 \text{ nF}$ ,  $\Delta I_1 = 250 \text{ kA}$ ,  $\Delta I_2 = 110 \text{ kA}$ ,  $\Delta t_1 = 25 \text{ ns}$ , and  $\Delta t_2 = 35 \text{ ns}$ .

sometime prior to the formation of the pinch thus completing the secondary current path. Breakdown also apparently occurs between the auxiliary electrode and the DPF chamber since a measurable current was not observed to flow through the auxiliary electrode external to the DPF chamber. As the distance between the electrodes increases, the electrodes are apparently shielded from each other and breakdown is less likely to occur. Therefore, the average of the peak beam current over a number of shots increases since the magnetic deflection caused by the secondary current is less likely to occur.

On the other hand, when the auxiliary electrode is effectively connected to the DPF anode through the uncharged capacitance of the coaxial feeder cable, breakdown initially occurs between the auxiliary electrode and the DPF vacuum chamber since the chamber is at the cathode potential and is closer to the auxiliary electrode than any other part of the cathode structure. A series CLC circuit consisting of the 84- $\mu$ F DPF capacitor bank, the 1.35-nF equivalent capacitance of the coaxial feeder cable, and the 3.2- $\mu$ H inductance of the feeder cable connection is formed once breakdown occurs. It can be shown that since the effective capacitance of the feeder cable is much less than that of the DPF capacitor bank, the voltage across the feeder cable capacitance reaches nearly twice the voltage on the DPF capacitor bank at breakdown in a time which is short in comparison to the DPF discharge and is given by

$$\tau \approx \frac{\pi}{2} \sqrt{LC} \approx 0.1 \mu s \quad (V-26)$$

where C is the effective capacitance of the feeder cable.

Thus, when the auxiliary electrode is connected to the coaxial feeder cable, the distributed inductance of the circuit causes the potential of

the electrode to be somewhat higher than the potential it assumes when connected to the DPF cathode. Consequently, shielding of the electrode is somewhat more difficult when the electrode is connected to the feeder cable and requires a larger interelectrode distance for comparable shielding, a conclusion supported by the experimental results.

As a final consideration, an estimate is made of the secondary current necessary to produce a transverse magnetic flux density of sufficient magnitude to significantly deflect the DPF electron beam. If it is assumed that a Larmor radius equal to the radius of the DPF anode aperture (0.75 cm) is sufficient to deflect the beam and that the beam passes through a region in which the transverse magnetic field is relatively constant over a characteristic length of at least one Larmor radius, the required magnetic flux density for a 150 keV electron initially propagating parallel to the DPF axis is calculated using Eq. (V-16) to be 0.19 T. Ampere's Law can be used to derive the relationship between the magnetic flux density and the secondary current. If it is assumed that the secondary current occupies a roughly cylindrical channel with a radius less than some radius  $b$ , the current and magnetic flux density are related by

$$I = \frac{2\pi b}{\mu_0} B = 9.3 \times 10^5 b \quad (V-27)$$

where  $b$  is chosen to be the distance from the center of the secondary current channel to the DPF axis and  $B = 0.19$  T. Since  $b$  is probably on the order of a centimeter, the secondary current is on the order of 10 kA which is significantly less than the 500 kA main discharge current and could conceivably be produced by the proposed model.



## Chapter VI

### CONCLUSION

This investigation has addressed the possible enhancement of the DPF electron beam. The first part of the investigation found that an axial magnetic field in the drift region improved the probability of observing an electron beam with a relatively larger peak current. The second part of the investigation showed that the presence of a third electrode in the DPF chamber has, on the average, an adverse effect on the DPF electron beam.

The magnetic guiding field increased the probability of observing a peak beam current greater than 10 kA from 10% of the discharges to 20%. The improvement is attributed to a reduction in beam loss achieved by confining the electrons in the beam to a Larmor radius less than the radius of the drift tube. An axial magnetic field can also be used to counteract Coulomb expansion and magnetic self-pinch of the beam; however, this is not considered to be a major factor in the reduction of beam loss since peak beam currents well in excess of the Alfvén limit were observed without the use of the guiding field. Further investigation into the improvement of the beam reproducibility should address the operating conditions of the DPF so that the particle accelerating mechanisms can be made more reproducible.

The adverse effect on the average peak beam current transported through the drift tube was shown to have an inverse relationship to the distance between the auxiliary electrode and the DPF anode. This effect is

more pronounced when the auxiliary electrode is connected to the coaxial feeder cable as opposed to the cathode. Also when the electrode is connected to the feeder cable, the current measured in the inductive energy storage circuit was shown to have the form of an impulse-like response of an underdamped RLC circuit. The impulse excitation is attributed to the time rate of change of the DPF current at the pinch and a lumped-parameter model is proposed which suggests that a coupling exists between the DPF discharge circuit and the inductive energy storage circuit. The response predicted by the model was shown to compare favorably with the experimentally observed results.

The diagnostic results of this investigation are not sufficient to conclusively determine the role of the auxiliary electrode and its effect on the electron beam. However, a model based on the available data is proposed as an explanation for the observed beam disturbance. The model proposes that an asymmetric current produces a magnetic field component in the region of the anode aperture that is transverse to the DPF axis and of sufficient strength so as to magnetically deflect the electron beam. The presence of the auxiliary electrode apparently acts as the catalyst for the formation of the secondary current path. Furthermore, the distance between the auxiliary electrode and the DPF anode for which the electrodes are shielded from each other depends on whether the auxiliary electrode is initially connected to the coaxial feeder cable or the DPF cathode. This dependence is attributed to a voltage doubling effect which occurs when the auxiliary electrode is connected to the coaxial feeder cable.

To determine the validity of this hypothesis, three experiments are suggested. First, the spatial anisotropy of neutron emission using deuterium as the fill gas could be measured for various electrode separations.

This experiment will establish whether the accelerating mechanisms are indeed unaffected and may also provide clues as to the degree to which the beam has been deflected (assuming that the ion beam produced by the DPF experiences the same type of disturbance as the electron beam). Second, magnetic field measurements in the region of the auxiliary electrode tip and the DPF anode aperture could be made for various electrode separations in order to establish whether magnetic interaction is a viable explanation for the beam disturbance. Third, a fast, high-voltage probe could be used to verify the voltage doubling effect on the equivalent capacitance of the coaxial feeder cable.

## LIST OF REFERENCES

- [1] G.M. Molen, "Electron Burst Measurements Produced by a Plasma Focus," Proc. International Conf. on Energy Storage, Compression, and Switching, Venezia, Italy, 1978.
- [2] G.M. Molen, M.J. Bernstein, K.W. Paschen, and R.H. Vandre, "Transient Radiation and Dose-Enhancement Effects in Transistors," The Space and Missile Systems Organization rept. no. SAMSO-TR-78-108, 1978.
- [3] G.F. Knapp, M.E. thesis, Old Dominion University, Norfolk, VA, 1983.
- [4] J.W. Mather, Methods of Experimental Physics, vol. 9, pt. B, ed. by R.H. Lovberg and H.R. Griem, New York: Academic Press, 1971, pp. 187-249.
- [5] T. Oppenlander, G. Pross, G. Decker, and M. Trunk, "The Plasma Focus Current in the Compression Phase," Plasma Phys., vol. 19, pp. 1075-1083, November 1977.
- [6] N.W. Jalufka and J.H. Lee, "Current Sheet Collapse in a Plasma Focus," Phys. Fluids, vol. 15, pp. 1954-1958, November 1972.
- [7] A. Bernard, A. Couderville, A. Jolas, J. Launspach, and J. de Mascureau, "Experimental Studies of the Plasma Focus and Evidence of Nonthermal Processes," Phys. Fluids, vol. 18, pp. 180-194, February 1975.
- [8] J.N. Downing and M. Eisner, "Dynamics of the Dense Plasma Focus as Determined from an Analysis of Laser Scattering Spectra," Phys. Fluids, vol. 18, pp. 991-1001, August 1975.
- [9] G. Decker, B. Nahrath, T. Oppenlander, G. Pross, B. Ruckle, H. Schmidt, M. Shakhatre, and M. Trunk, "Dynamics of 120 and 20 kV Plasma Focus Devices with respect to Density and Current Distribution, and Neutron and X-Ray Emission," Proc. International Conf. on Plasma Phys. and Controlled Nuclear Fusion Research, IAEA, vol. III, pp. 441-446, Vienna, 1977.
- [10] F. Hamada, K. Shimodo, and K. Hirano, "Streak Mode Interferometric Study of Plasma Focus," Phys. Fluids, vol. 22, pp. 1217-1218, June 1979.

- [11] L. Bertolot, R. Deutsch, H. Herold, U. Jager, H.J. Kaeppler, A. Mozer, T. Oppenlander, B. Ruckle, M. Sadowski, P. Schilling, and H. Schmidt, "Experiments on Plasma Focus Dynamics, Neutron Production, and Ion Emission," Proc. International Conf. on Plasma Phys. and Controlled Nuclear Fusion Research, IAEA, Brussels, 1980.
- [12] H. Sahlin, G. McFarland, R. Barlett, and R. Gullickson, "The Plasma Focus as a Pulsed Power Source," Proc. International Topical Conf. on Electron Beam Research and Technology, Albuquerque, 1975.
- [13] H.J. Kaeppler, "Basic Physical Phenomena, Neutron Production, and Scaling of the Dense Plasma Focus," University of Stuttgart internal rept. no. IPF-77-7, Stuttgart, W. Germany, 1977.
- [14] H.J. Kaeppler, "Neutron Production in the Dense Plasma Focus," Proc. International Conf. on Plasma Phys. and Controlled Nuclear Fusion Research, IAEA, vol. III, pp. 437-439, Vienna, 1977.
- [15] A. Hayd, H.J. Kaeppler, M. Maurer, and P. Meinke, "The Calculation of Turbulence Phenomena in Plasma Focus Dynamics using REDUCE," University of Stuttgart internal rept. no. IPF-82-7, Stuttgart, W. Germany, 1982.
- [16] N.J. Peacock, M.J. Forrest, M.G. Hobby, and P.D. Morgan, "Measurements of the Plasma Confinement and Ion Energy in the Dense Plasma Focus," Proc. Conf. on Plasma Phys. and Controlled Thermonuclear Fusion, pp. 537-551, Madison, 1971.
- [17] J.P. Rager, Yu. Alexeev, J. Appelt, J.S. Brzosko, J. Ehrhardt, C. Gurlan, K. Hubner, L. Ingrosso, M. Kazeev, P. Kirchesch, J. Klobukowska, H. Kroegler, S. Podda, B.V. Robouch, and K. Steinmetz, "Plasma Dynamics and Particle Confinement in the 1 MJ Plasma Focus at Frascati," Centro Ricerche Energia Frascati internal rept., Italy, 1982.
- [18] H. Krompholz, L. Michel, K.H. Schoenbach, and H. Fischer, "Neutron-Ion- and Electron-Energy Spectra in a 1 kJ Plasma Focus," Appl. Phys., vol. 13, pp. 29-35, 1977.
- [19] A. Bernard, A. Coudeville, J.P. Garconnet, A. Jolas, J. de Mascureau, C. Nazet, "Structure of Current Sheath and Fast-Particle Beams in the Focus Experiment," Proc. International Conf. on Plasma Phys. and Controlled Nuclear Fusion Research, IAEA, vol. III, pp. 471-482, Vienna, 1977.
- [20] V.V. Vikhrev, K.G. Gureev, S.K. Zhdanov, V.M. Korzhavin, B.A. Trubnikov, "Dynamics of a Non-Cylindrical Z-Pinch and the Particle Acceleration Mechanism," Proc. International Conf. on Plasma Phys. and Controlled Nuclear Fusion Research, IAEA, vol. III, pp. 455-469, Vienna, 1977.

- [21] L. Bertolot, R. Deutsch, H. Herold, U. Jager, A. Mozer, M. Sadowski, and H. Schmidt, "Ion Emission Characteristics of Plasma Focus Devices," University of Stuttgart internal rept. no. IF-81-9, Stuttgart, W. Germany, 1981.
- [22] M. Yokoyama, Y. Kitagawa, Y. Yamada, M. Okada, Y. Yamamoto, C. Yamanaka, K. Hirano, Y. Kondoh, K. Shimoda, T. Yamamoto, M. Hattori, and M. Sato, "Experimental Progress on Plasma Dynamics and Energetic Particle Generation in Dense Plasma Focus," Proc. International Conf. on Plasma Phys. and Controlled Nuclear Fusion Research, IAEA, Baltimore, 1982.
- [23] W. Stygar, G. Gerdin, F. Venneri, and J. Mandrekas, "Particle Beams Generated by a 6-12.5 kJ Dense Plasma Focus," To be published in Nuclear Fusion.
- [24] W.H. Bostick, V. Nardi, and W. Prior, "Space-Time Structure of Neutron and X-Ray Sources in a Plasma Focus," Proc. International Conf. on Plasma Phys. and Controlled Nuclear Fusion Research, vol. III, pp. 497-505, Vienna, 1977.
- [25] W. L. Harries, J.H. Lee, and D.R. McFarland, "Trajectories of High Energy Electrons in a Plasma Focus," Plasma Phys., vol. 20, pp. 95-106, 1978.
- [26] R.L. Gullickson, "Applications of the Plasma Diode Model to Particle Acceleration in the Plasma Focus Device," Proc. International Workshop on Plasma Focus Research, Moscow, 1981.
- [27] M.J. Rhee, "Peak Energies of Charged Particles Accelerated in a Plasma Focus," Bull. Amer. Phys. Soc., vol. 26, p. 893, September 1981.
- [28] N.V. Filippov, T.I. Filippova, and V.P. Vinogradov, "Dense, High-Temperature Plasma in a Non-Cylindrical Z-Pinch Compression," Nuclear Fusion Supplement, pt. 2, p. 577-587, 1962.
- [29] J.H. Lee, L.P. Shomo, M.D. Williams, and H. Hermansdorfer, "Neutron Production in a Plasma Focus," Phys. Fluids, vol. 14, pp. 2217-2223, October 1971.
- [30] M.J. Bernstein and G.G. Comisar, "Neutron Energy and Flux Distribution and a Crossed-Field Acceleration Model of Plasma Focus and Z-Pinch Discharges," Phys. Fluids, vol. 15, pp. 700-707, April 1972.
- [31] S.P. Gary and F. Hohl, "Ion Kinematics in a Plasma Focus," Phys. Fluids, vol. 16, pp. 997-1002, July 1973.
- [32] F. Hohl and S.P. Gary, "Electron Kinematics in a Plasma Focus," Phys. Fluids, vol. 20, pp. 683-687, April 1977.

- [33] H. Herold, L. Bertalot, R. Deutsch, W. Grauf, U. Jager, H.J. Kaeppler, F. Lepper, T. Oppenlander, H. Schmidt, R. Schmidt, J. Schwarz, K. Schworer, M. Shakhatre, "Investigation of the Neutron Production Phases of a Large Plasma Focus Device," Proc. International Conf. on Plasma Phys. and Controlled Nuclear Fusion Research, IAEA, Baltimore, 1982.
- [34] H.L.L. van Paassen and R.H. Vandre, "X-Ray Spectra from Dense Plasma Focus Devices," Phys. Fluids, vol. 13, pp. 2606-2612, October 1970.
- [35] W.L. Harries, J.H. Lee, and D.R. McFarland, "Space and Time Resolved Emission of Hard X Rays from a Plasma Focus," Plasma Phys., vol. 20, pp. 963-969, 1978.
- [36] R.L. Gullickson and R.H. Barlett, "X-Ray Analysis for Electron Beam Enhancement in the Plasma Focus Device," Advances in X-Ray Analysis, vol. 18, pp. 184-196, August 1974.
- [37] D. Pellinen, "A High Current, Subnanosecond Response Faraday Cup," Rev. Scientific Instruments, vol. 41, pp. 1347-1348, September 1970.
- [38] G.M. Molen, K.W. Paschen, R.H. Vandre, and K.T. Young, "Thermoluminescent Detector Spectral Analysis on the Retro-Focus Simulator," The Space and Missile Systems Organization rept. no. SAMS0-TR-76-215, 1976.
- [39] H. Knoepfel, Pulsed High Magnetic Fields. New York: American Elsevier, 1970, pp. 49-59.
- [40] H.C. Kirbie, M.S. Pronko, and E.C. Hoelzer, "The Design and Construction of the Auxiliary Capacitor Bank," Dept. of Elec. Engineering Pulsed Power Lab. internal rept. no. 82-02, Old Dominion University, Norfolk, VA, 1982.
- [41] E. Kreyszig, Advanced Engineering Mathematics. New York: John Wiley and Sons, 1972, pp. 751-756.
- [42] R.B. Miller, An Introduction to the Physics of Intense Charged Particle Beams. New York: Plenum Press, 1982, pp. 19-212.
- [43] H. Alfven, "On the Motion of Cosmic Rays in Interstellar Space," Phys. Rev., vol. 55, pp. 425-429, March 1939.
- [44] D.A. Hammer and N. Rostoker, "Propagation of High Current Relativistic Electron Beams," Phys. Fluids, vol. 13, pp. 1831-1850, July 1970.
- [45] P.A. Miller, J.B. Gerardo, and J.W. Poukey, "Relativistic Electron Beam Propagation in Low-Pressure Gases," J. Appl. Phys., vol. 43, pp. 3001-3007, July 1972.
- [46] P.A. Miller and J.B. Gerardo, "Relativistic Electron Beam Propagation in High-Pressure Gases," J. Appl. Phys., vol. 43, pp. 3008-3013, July 1972.

- [47] D.T. Paris and F.K. Hurd, Basic Electromagnetic Theory. New York: McGraw-Hill, 1969, pp. 544-545.
- [48] F.W. Grover, Inductance Calculations. New York: Dover, 1964, pp. 59-61.
- [49] E. Nasser, Fundamentals of Gaseous Ionization and Plasma Electronics. New York: Wiley-Interscience, 1971, pp. 245-248.
- [50] R.H. Huddlestone and S.L. Leonard, Plasma Diagnostic Techniques. New York: Academic Press, 1965, pp. 8-13.
- [51] W.R. Smythe, Static and Dynamic Electricity. New York: McGraw-Hill, 1950, pp. 270-273.
- [52] F.F. Chen, Introduction to Plasma Physics. New York: Plenum Press, 1974, pp. 25-31.



## APPENDIX

- A. Diagnostic Equipment
- B. Guiding Field Winding Configuration
- C. DPF Remote Control System
- D. DPF Trigger System

## Appendix A

### DIAGNOSTIC EQUIPMENT

All of the diagnostic equipment, with the exception of the Faraday cup, are described in this appendix. These diagnostics include the Rogowski probe, PIN diodes, soft x-ray pinhole photography, image converter camera, and integrated  $\dot{B}$  probe.

#### Self-Integrated Rogowski Probe

The self-integrated Rogowski probe, which has a sensitivity of 7.45 kA/V when terminated into 1 M $\Omega$ , measured the primary DPF discharge current by encircling the DPF anode as shown in Fig. A-1. The design of the probe followed the procedure given in Ref. [50].

The probe was constructed by winding 18-AWG magnet wire around the inner core of a 1-m length of RG-8 coaxial cable. The windings are electrostatically shielded by an electrically grounded, 0.13-mm-thick copper foil which completely encircles the windings except for a 3.0-mm slit along the length of the probe. Since the response of the probe is proportional to the time derivative of the DPF current, the signal must be integrated. It can be shown that the probe can be made self integrating by connecting a low-resistance shunt in parallel with the probe coil. The shunt must be such that  $R \ll \omega L$  where  $R$  is the combined resistance of the shunt and the coil wire,  $\omega$  is the characteristic radian frequency of the signal being measured, and  $L$  is the inductance of the probe coil. The above inequality requires that the characteristic duration for the

AD-A133 462

AN INVESTIGATION OF ACCELERATING MECHANISMS IN A PLASMA 2/2  
FOCUS RELEVANT TO (U) OLD DOMINION UNIV NORFOLK VA  
DEPT OF ELECTRICAL ENGINEERING M S PRONKO ET AL.

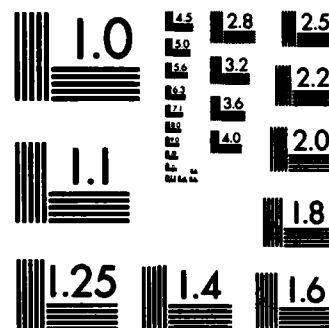
UNCLASSIFIED

JUL 83 AFOSR-TR-83-0794 AFOSR-81-0039

F/G 20/9

NL





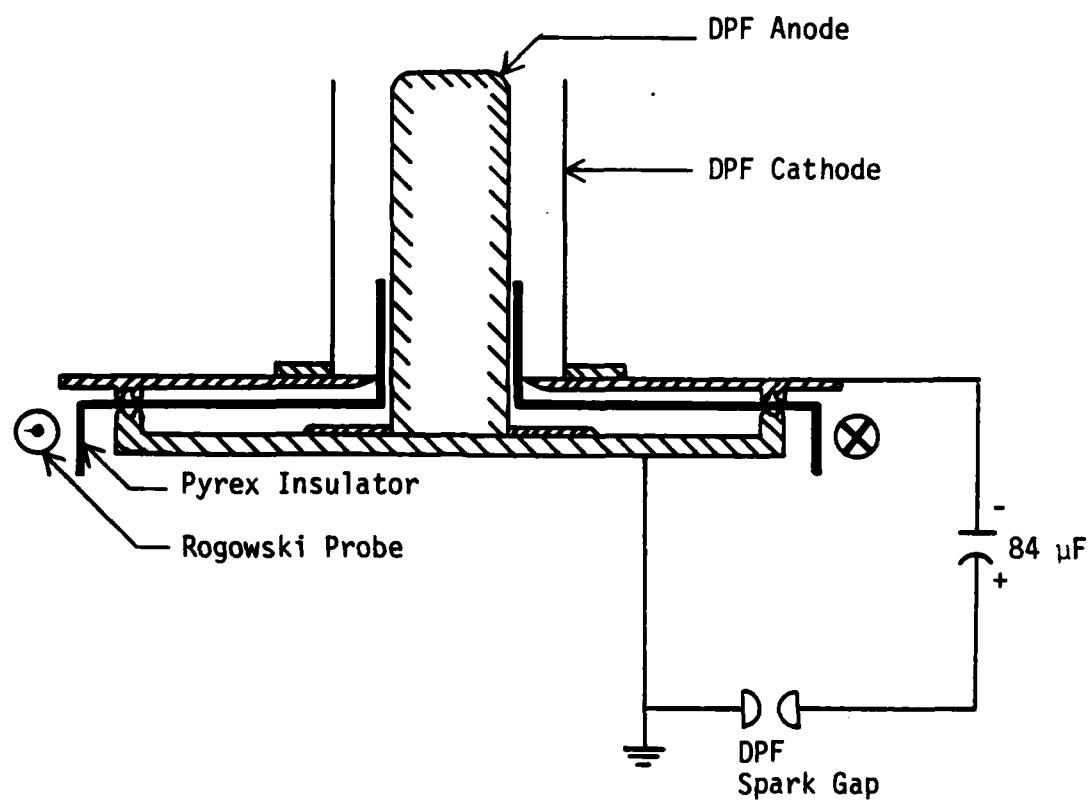


Fig. A-1. Location of the Rogowski probe in the DPF apparatus that was used to measure the DPF discharge current.

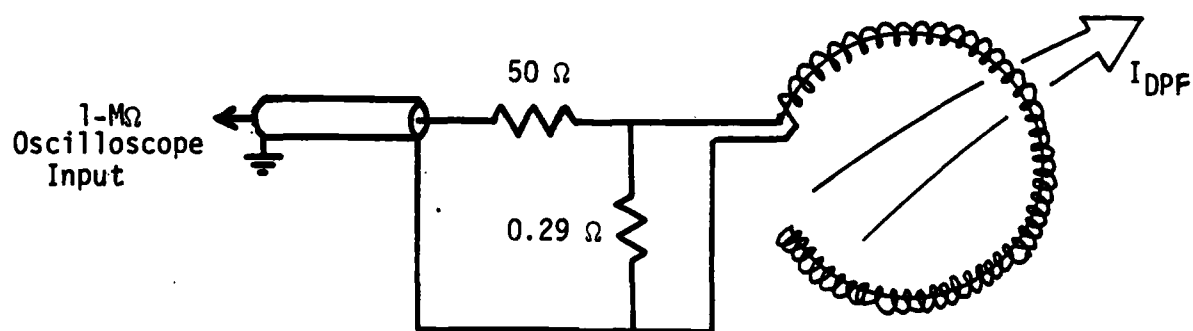


Fig. A-2. Electrical schematic of the Rogowski coil, 0.29- $\Omega$  shunt resistor, and 50- $\Omega$  impedance-matching resistor.

transient signal must be much less than the  $L/R$  time constant of the probe circuit. Thus, the probe acts as a current transformer where the output, which is measured as the voltage across the shunt resistor, is directly proportional to the DPF current.

The shunt resistor is a 2.54-cm length of 28-AWG stainless steel wire with a calculated resistance of  $0.29 \Omega$ . A  $50\text{-}\Omega$  resistor, as shown in Fig. A-2, is connected in series with the probe so as to match the impedance of the probe to the signal cable.

### PIN Diodes

PIN diodes, which were used to measure relative x-ray dose rate, differ from ordinary diodes in that the region which separates the p-doped and n-doped layers of the diode is much thicker than in a conventional junction diode. The output is proportional to the number of electron-hole pairs created by x-ray photon absorption in this thicker, intrinsic region. As such, the diode signal is dependent on the position of the diode relative to the x-ray source as well as the energy of the x-ray photons which determine the photon absorption length.

The response of the diodes is easily related to the x-ray dose rate in  $\text{Rad(Si)/s}$  by considering the active region of the diodes. However, a calculation of the x-ray fluence is considerably more difficult since this requires knowledge of the photon spectral distribution. For the DPF, the photons have a rather broad distribution which not only varies during the pulse but also from shot to shot. Thus, in this investigation, the PIN diodes are used to provide relative data about the intensity of the x rays in a given spectral region as determined by absorption filters which are mounted between the diodes and the x-ray source.

As shown in Fig. A-3, the PIN diodes were reverse biased using a 75-V dc power supply, and the signals were capacitively coupled to an oscilloscope. The two types of diodes which were used have intrinsic layer thicknesses of 125  $\mu\text{m}$  and 20  $\mu\text{m}$ , and active areas of 25  $\text{mm}^2$  and 1.12  $\text{mm}^2$ , respectively.

### Soft X-Ray Pinhole Photography

As shown in Fig. A-4, simple geometrical optics can be used to trace rays through the aperture of the soft x-ray pinhole camera. The "pinhole" in the camera consists of a 20- $\mu\text{m}$ -diameter hole in a 0.76-mm-thick sheet of tantalum. The hole is covered with an additional 0.02 mm of beryllium, which has an  $e^{-1}$  transmission of 2.3 keV, so as to provide a vacuum seal.

The pinhole camera consists of three aluminum flanges, a cylindrical aluminum chamber, and a Polaroid film pack which are assembled as shown in Fig. A-5. X rays emitted from the pinch region pass through the pinhole and are imaged at the back plane where they expose the photographic film. The cylindrical chamber was slightly overpressurized with helium so as to decrease the absorption of soft x rays.

The magnification of the pinhole imaging system is determined as

$$M = \frac{d_1}{d_2} \quad (\text{A-1})$$

where  $d_1$  is the distance from the object to the pinhole and  $d_2$  is the distance from the pinhole to the image. Since  $d_2$  is largely determined by the length of the cylindrical chamber, the magnification of the imaging system can be changed by altering the chamber length. Two chambers were available for use with this system having lengths of 17.1 cm and 5.1 cm giving magnifications of 1.1 and 0.675, respectively.

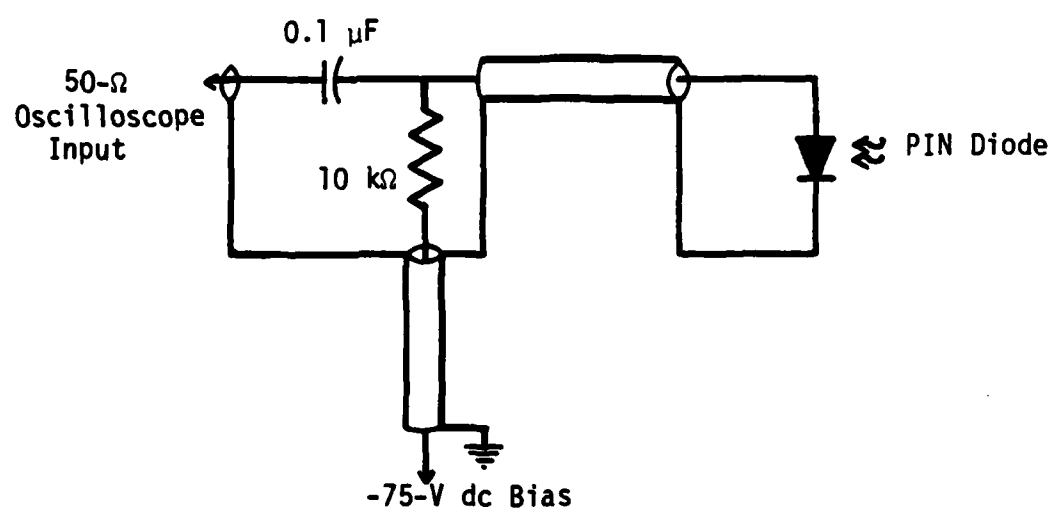


Fig. A-3. Electrical schematic of the PIN diode bias circuit.



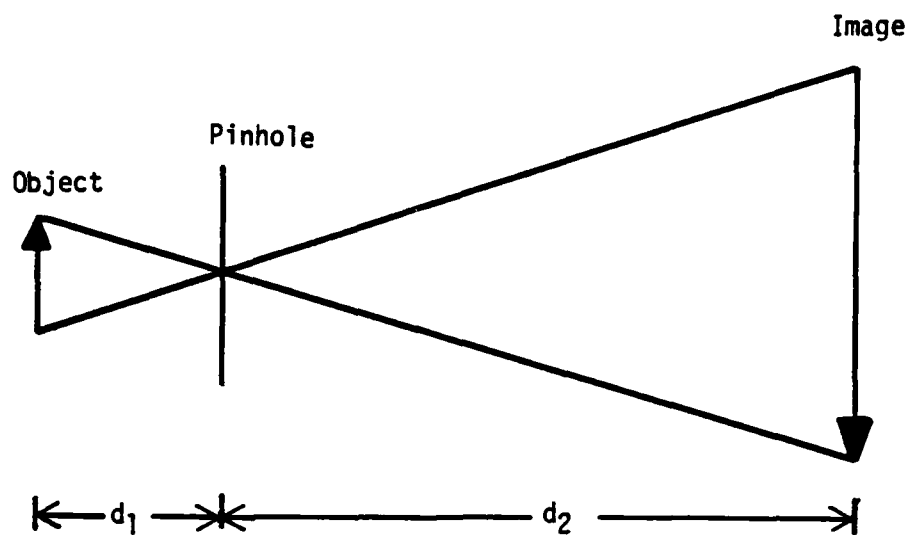


Fig. A-4. Ray tracing in a pinhole imaging system.

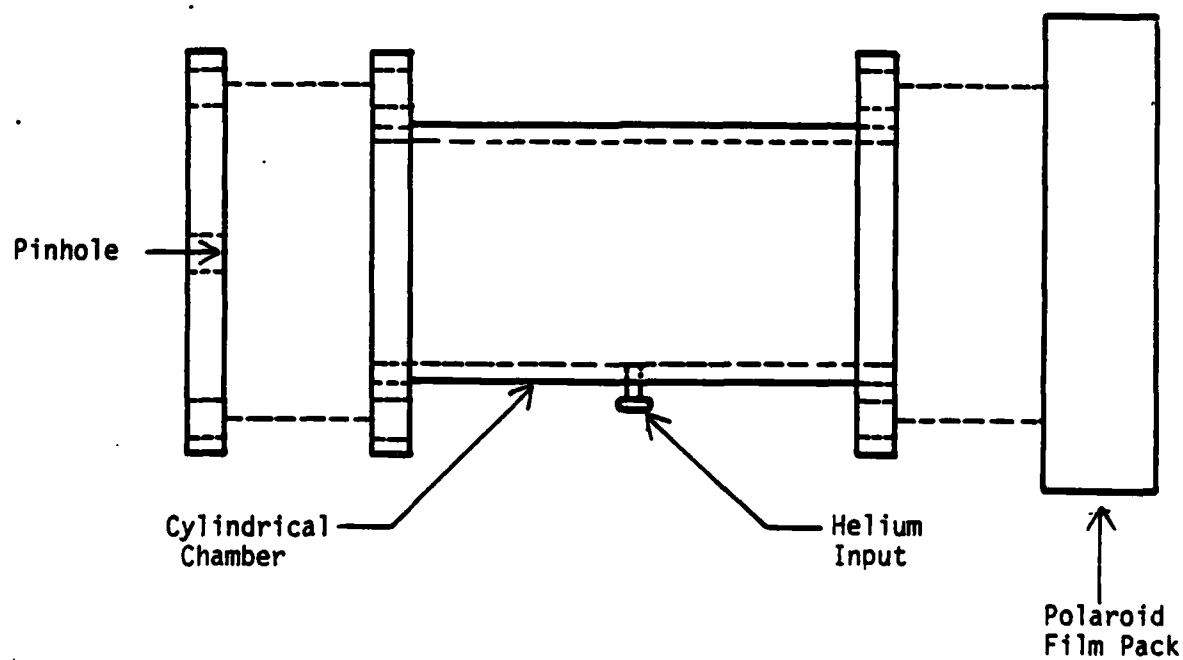


Fig. A-5. Exploded view of the soft x-ray pinhole camera.

### Image Converter Camera System

The image converter camera (ICC) system consists of a TRW STL model 1D ICC, a streak photography plug-in unit, a framing photography plug-in unit, and an auxiliary optical extension mounted in front of the ICC. The ICC system is mounted in an aluminum enclosure which functions as an electrostatic shield as well as a convenient roll-around cart.

Streak durations available from the streak unit range from 0.5  $\mu$ s to 10  $\mu$ s. The framing unit produces three consecutively timed frame photographs with electronic shutter speeds of 5 ns, 10 ns or 20 ns. The time delay between the first and second frames, and the second and third frames can be independently preset to be in the range of 50 ns to 500 ns.

The ICC imaging system, including the optical extension, consists of a 127-mm f/2.0 lens, a 203-mm f/7.1 lens, a mechanical shutter with an adjustable f-stop, and a removable 0.13-mm slit used for streak photography. The overall magnification of the system is 1:0.23.

### B Probe and Passive Integrator

The magnetic flux density produced by the guiding field solenoid was measured using a calibrated, passively integrated  $\dot{B}$  probe. The probe is a 10-turn, single-layer solenoid constructed with 28-AWG magnet wire wound on a 5.0-mm-diameter ceramic form. The probe is integrated by a passive RC integrator having a time constant of about 1.6 ms. The sensitivity of the probe and integrator was found to be 66.0 T/V where the calibration is valid only if the magnetic field lines linking the probe are parallel to the probe axis.

The necessarily small cross-sectional area and length of the solenoidal probe, as well as the magnitude of the magnetic flux density being considered, produced output voltages only on the order of a few millivolts.

Consequently, an active amplifier with a measured voltage gain of 48 and a bandwidth of approximately 10 kHz was used to increase the sensitivity of the probe.

## Appendix B

### GUIDING FIELD WINDING CONFIGURATION

A vacuum valve was included in the beam guiding apparatus so as to facilitate the frequent maintenance required by the Faraday cup. The geometrical configuration of the apparatus (see Fig. III-5) was chosen as the simplest design for the available components; however, the vacuum valve precluded the use of a simple, one-piece guiding field solenoid. Without magnetic field compensation, the 4.4-cm gap between the ends of the guiding field solenoidal sections inside the valve is a region of lower magnetic flux density than the region inside the solenoidal sections. Compensation was achieved by adding extra windings to the ends of both solenoidal sections closest to the valve so that the magnetic flux density on axis at the midpoint between the ends of the solenoidal sections was substantially increased relative to the flux density at the midpoint for no compensation.

To provide guidelines for the construction of the compensation winding configuration, the magnetic flux density at the midpoint between the ends of the solenoidal sections was approximated as the superposition of flux densities produced by many single loops of wire, all carrying a current  $I$ . A circular loop of wire, having a radius of  $a$ , produces a magnetic flux density on its axis which is given by

$$B = \frac{\mu_0 a^2 I}{2(a^2 + d^2)^{3/2}} \quad (B-1)$$

where  $\mu_0$  is the permeability of free space and  $d$  is the distance along the axis from the loop to the point of interest [51]. Eq. (B-1) was summed over a number of loops in appropriate geometrical arrangements for several different winding configurations. The resulting magnetic flux density was compared to the flux density produced inside the solenoidal sections which was approximated by

$$B = \frac{\mu_0 NI}{\ell} \quad (B-2)$$

where  $\ell$  is the total length of the guiding field solenoid and  $N$  is the number of turns. Imposing the condition that the winding configuration must produce a flux density at the midpoint approximately equal to the flux density inside the solenoidal sections, this procedure yielded a configuration consisting of an extra two layers of windings which are in addition to the main windings of the solenoid. These extra layers are located at the end of each solenoidal section closest to the valve and extend 3.8 cm along each section.

When the guiding field apparatus was assembled on the DPF, the magnetic flux density at the midpoint between the ends of the solenoidal sections was found to be about a factor of two lower than the magnetic flux density in the interior of the solenoid. Although the value of the minimum magnetic flux density is below the calculated value, the maximum Larmor radius of an electron at the midpoint is still well within the local radius of the drift tube. A plot of the magnetic flux density along the solenoid's axis in the region of the vacuum valve is presented in Fig. B-1. It should be noted that without compensation, the magnetic flux density at the midpoint would have been about a factor of 4.5 less than the flux density inside the solenoid as was measured in the early stages of the solenoid's

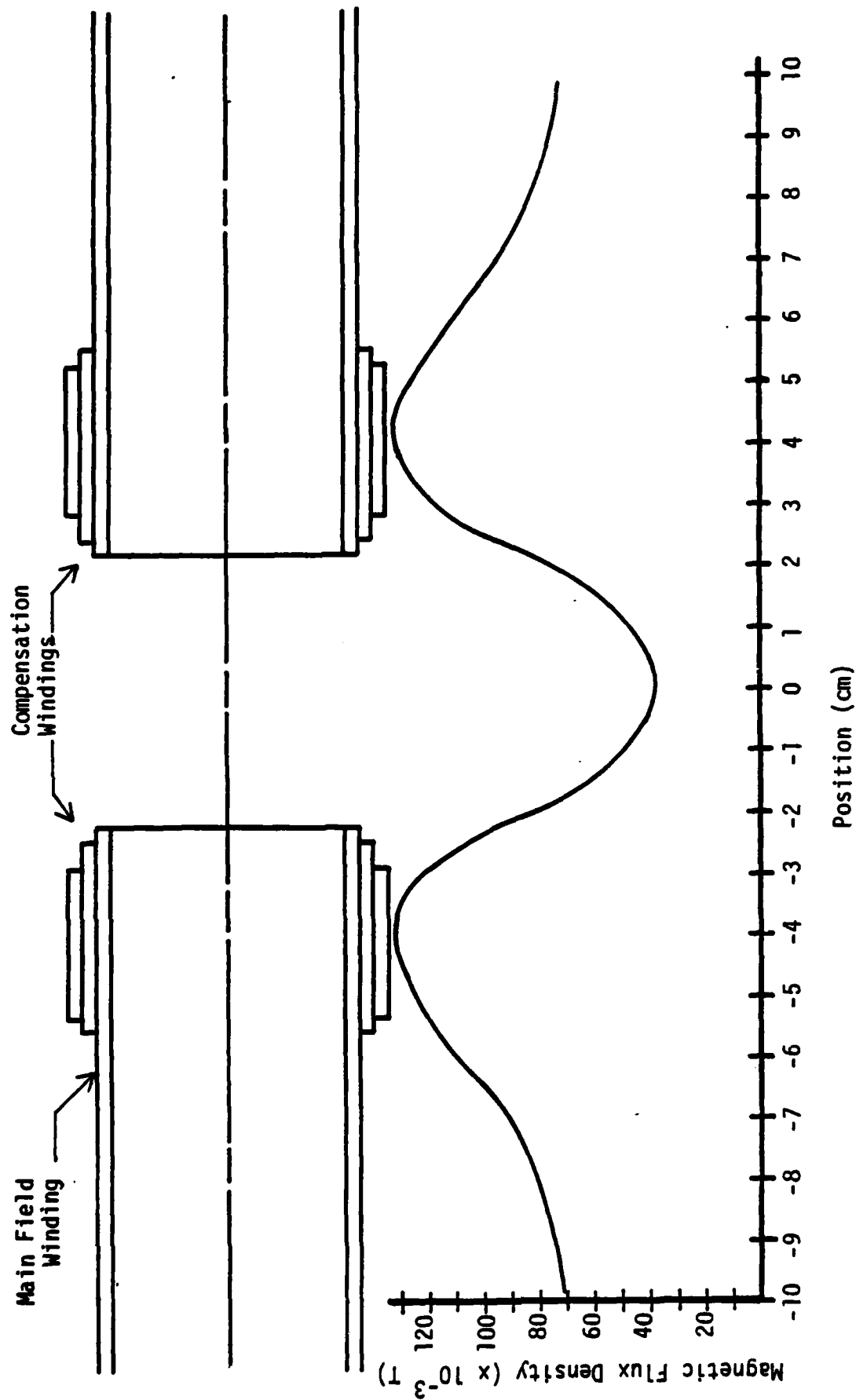


Fig. B-1. Plot of the magnetic flux density measured along the axis of the guiding field solenoid in the region of the vacuum valve for a coil current of 150 A. The field plot is scaled to the drawing.

construction. The maximum Larmor radius for this case would have been unacceptably large.

The use of the compensation windings introduces the possibility that the electrons will reflect from magnetic mirrors as they travel from a weak field region into a stronger field region. This effect would be most likely to occur as an electron travels from the weak field region inside the vacuum valve toward the much stronger field region produced by the compensation windings at the opening of the bottom section of the guiding field solenoid (see Fig. B-1). If  $\theta$  is the angle between the electron's velocity vector and its component parallel to the magnetic field lines in the weak field region, reflections can occur if

$$\sin^2\theta \geq \frac{B_{\min}}{B_{\max}} \quad (\text{B-3})$$

where  $B_{\min}$  is the magnetic flux density in the weak field region and  $B_{\max}$  is the flux density in the stronger field region [52]. For a coil current of 150 A,  $B_{\max}$  and  $B_{\min}$  were measured to be 0.130 T and 0.035 T, respectively. Thus, the minimum value of  $\theta$  required for reflection is  $31.3^\circ$ . Since the DPF anode aperture limits  $\theta$  to  $10^\circ$ , electrons propagating through the beam guiding solenoid are not subject to reflections.

## Appendix C

### DPF REMOTE CONTROL SYSTEM

The charging of the DPF capacitor bank and the capacitor in the beam guiding system was remotely controlled by a modular control system from inside the laboratory screenroom. The control system features independent control of up to four separate capacitor banks as well as a passive safety interlock system. Three basic commands are available from the system:

- (1) a "Dump" command which opens or closes a safety dump switch that is used to safely discharge energy stored in capacitor banks which cannot be discharged otherwise;
- (2) a "Charge" command which initiates the charging cycle of the capacitor banks; and
- (3) an "Interrupt" command which stops the charging of the capacitor banks but does not discharge them.

In addition, the charge command to each individual bank can be independently delayed to compensate for differences in charging rates between banks, the voltage on each bank can be monitored on an analog meter inside the screenroom, the charging cycle of each individual bank can be automatically interrupted when the voltage on the bank reaches a preset level, and a "Fire" command is available from the control system to initiate the experiment. The control system logic, a diagram of which is presented in Fig. C-1, is accomplished with electrically-rugged, electro-mechanical



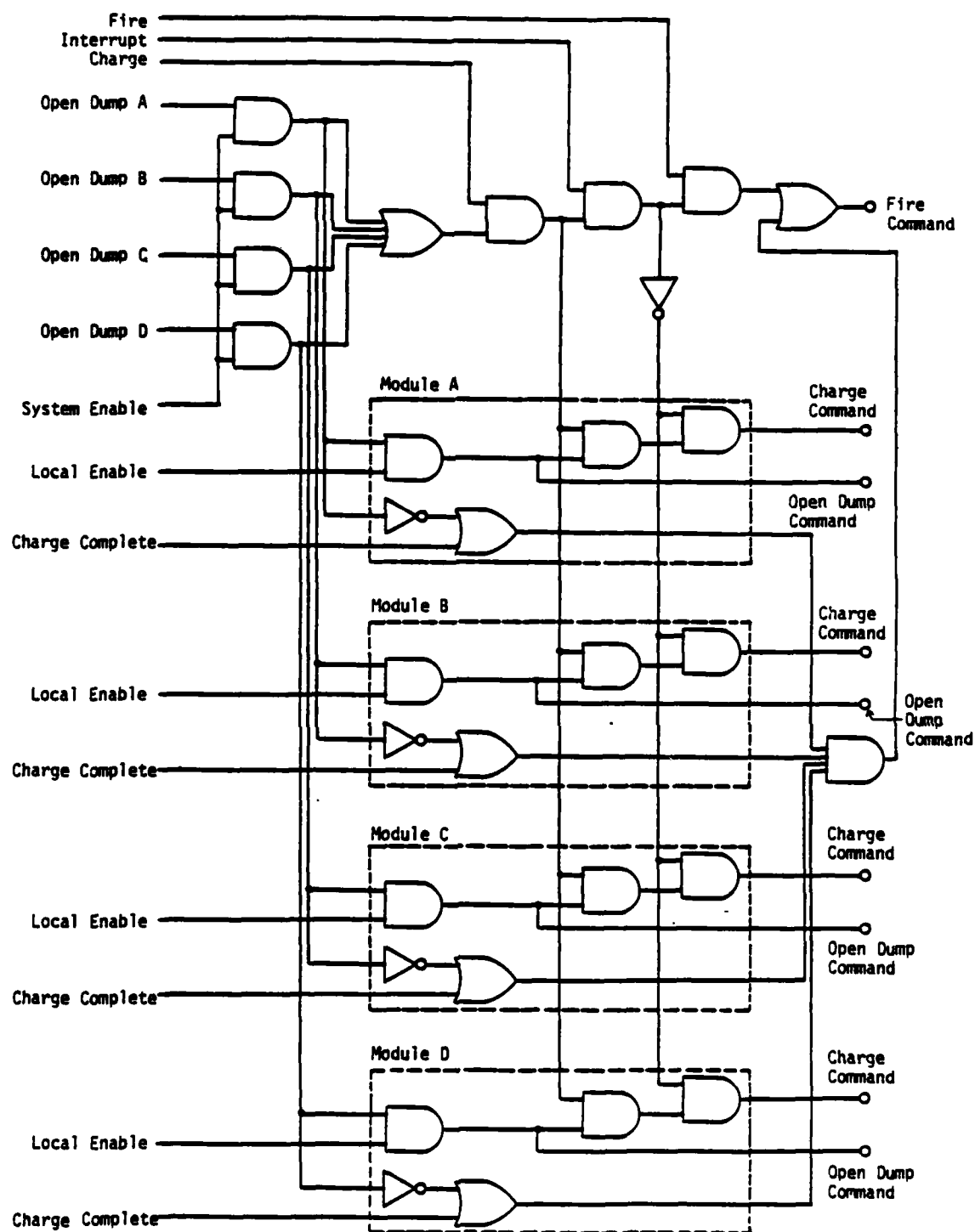


Fig. C-1. Remote control logic diagram. Modules A through D are located outside the screenroom and each interfaces the control system to a single capacitor bank.

relays because of the intense electromagnetic radiation produced by the DPF.

## Appendix D

### DPF TRIGGER SYSTEM

The DPF requires a trigger system which can initiate breakdown in the trigatron switches affixed to each capacitor bank with a relative jitter of less than 5 ns. The circuit designed to meet this requirement is shown in Fig. D-1. The trigatron trigger pulse is initiated by discharging the 0.5- $\mu$ F capacitor, which is transformer coupled to a spark gap, through a 3C45 thyatron. The spark gap simultaneously discharges four 500-pF door-knob capacitors which are transformer coupled to the trigatron trigger electrodes. Since two capacitor bank modules were used throughout this investigation, only two of the trigger channels shown in the figure were used. The trigger pulse applied to the trigatron has a risetime of 25 ns and a peak voltage of 25 kV.

Commercially available TTL pulse delay generators were used to sequence the triggering of the DPF trigger system, beam guiding field, image converter camera, and oscilloscopes. For the equipment requiring a medium high-voltage pulse, the Krytron pulse amplifier circuit shown in Fig. D-2 was used to step the TTL pulse up to a 600-V pulse having a risetime of less than 10 ns and a throughput delay of about 350 ns.

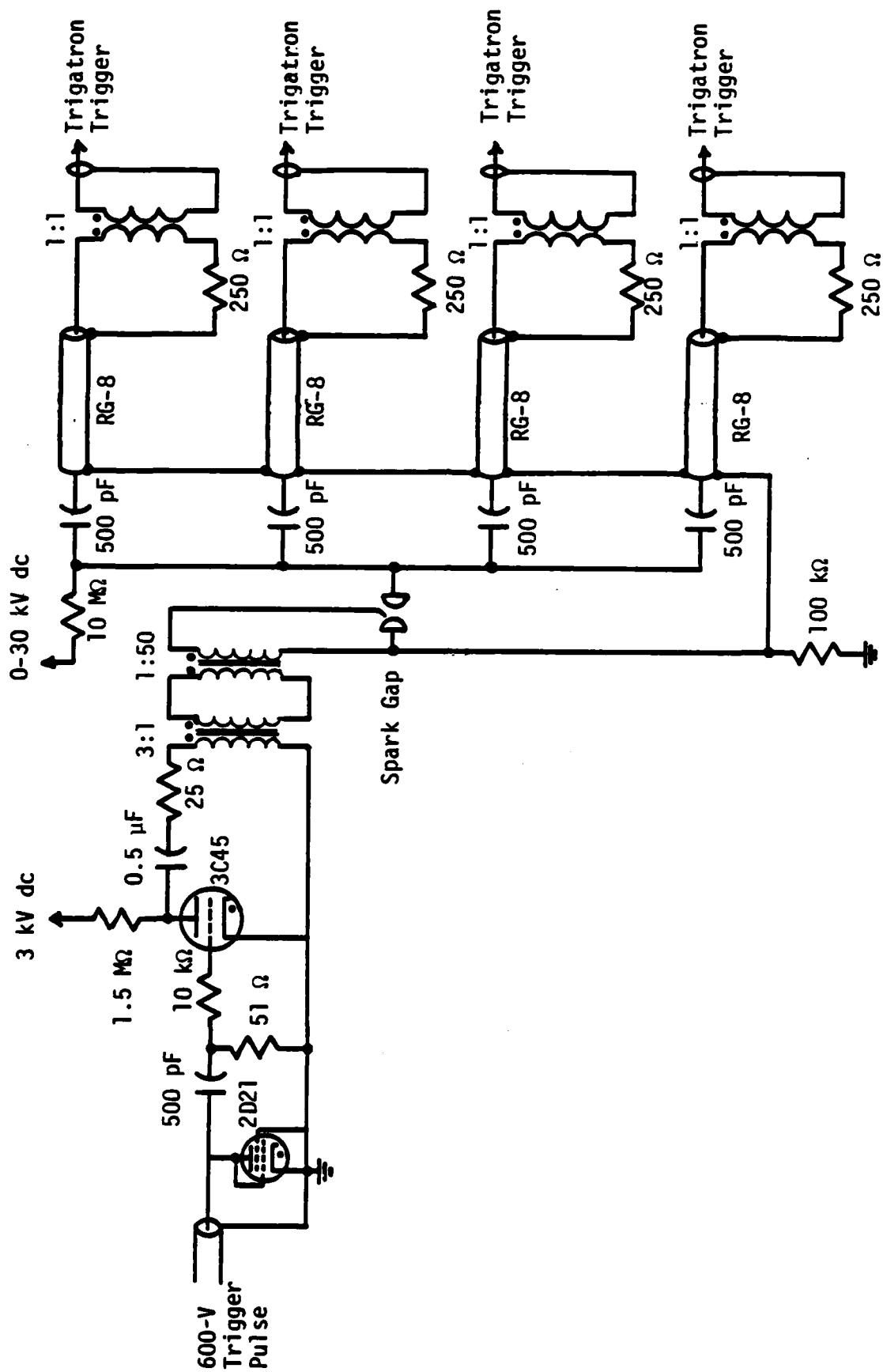


Fig. D-1. The DPF trigger system.

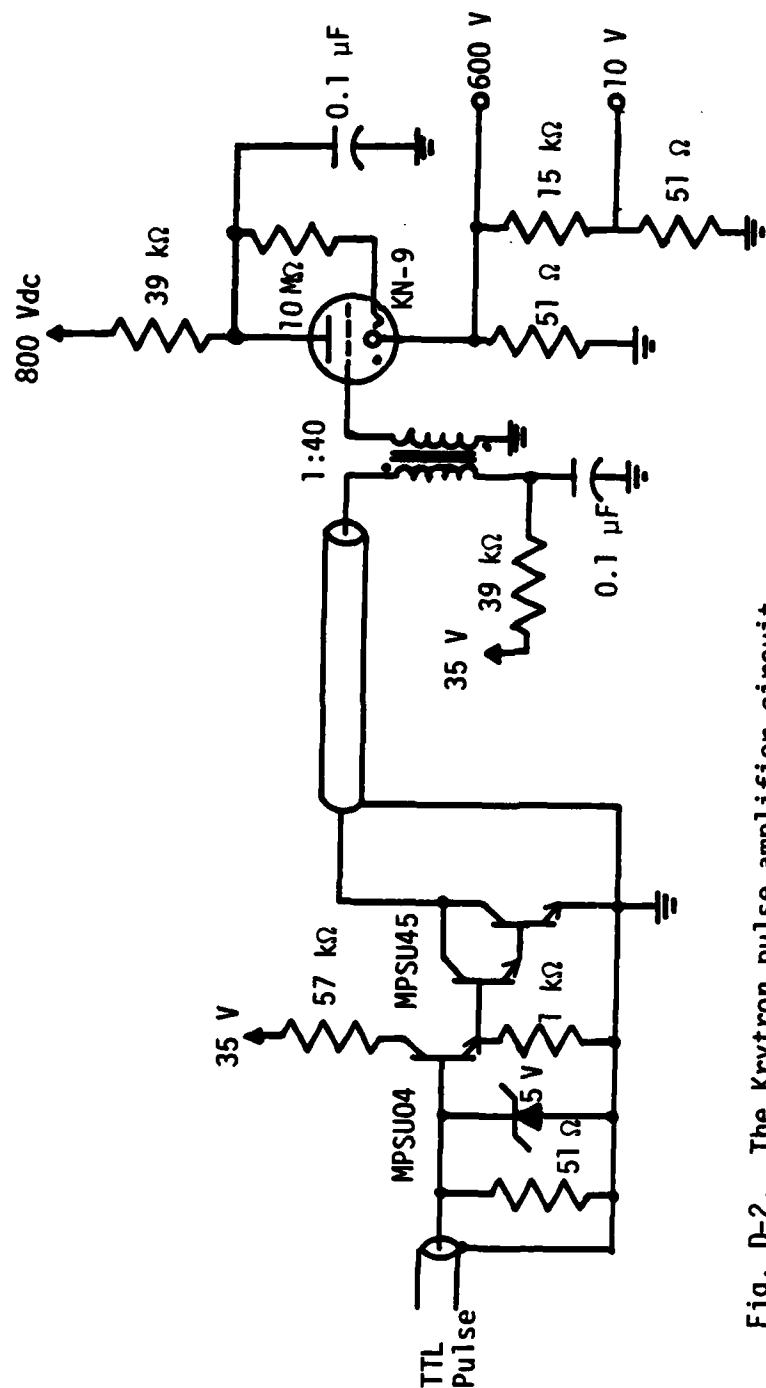


Fig. D-2. The Krypton pulse amplifier circuit.

END

FILMED

10-83

DTIC